DEPARTAMENT FÍSICA APLICADA I
ELECTROMAGNETISME

DINÁMICA DE LA RECOMBINACIÓN DE EXCITONES CONFINADOS EN NANOSTRUCTURAS CUÁNTICAS DE In(Ga)As

JORDI GOMIS BRESCÓ

UNIVERSITAT DE VALENCIA
Servei de Publicacions
2008

Aquesta Tesi Doctoral va ser presentada a València el dia 15 de juliol de 2008 davant un tribunal format per:

- D. Andrés Cantarero Saéz
- D. Salvador Sales Maicas
- D. Rudolf Bratschitch
- D. Andrew Schields
- D. Juan Capmany Francoy

Va ser dirigida per:
Dª. Juan P. Martinez Pastor
D. Ulrike Woggon

Depòsit legal:
I.S.B.N.:978-84-370-7291-3
Edita: Universitat de València
Servei de Publicacions
C/ Artes Gráficas, 13 bajo
46010 València
Spain
Telèfon: 963864115

UNIVERSITAT DE VALÈNCIA
Facultat de Física
Departament de Física aplicada i Electromagnetisme

Dinámica de la recombinación de excitones confinados en nanostructuras cuánticas de In(Ga)As.

por

Jordi Gomis i Brescó

Febrero 2008

Clàusula de bon ús

"Queda absolutament prohibida la utilització, recerca i desenvolupament, de manera directa o indirecta, de qualsevol de les aportacions científiques pròpies de l'autor que es presenten en aquesta memòria, per part de qualsevol exèrcit del món o per part de qualsevol grup armat, per a qualsevol ús militar i per a qualsevol altre ús que atempti contra els drets humans o contra el medi ambient, si no és amb el permís escrit de totes les persones del món."

Good Use Right

"It is strictly prohibited to use, to investigate or to develop, in a direct or indirect way, any of the scientific contributions of the author contained in this work by any army or armed group in the world, for military purposes and for any other use which is against human rights or the environment, unless a written consent of all the persons in the world is obtained"

"Un físico siempre se guía por el principio de mínima energía: piensa bien lo que va a hacer y porqué lo va a hacer. Luego diseña la manera de hacerlo con el mínimo esfuerzo."

"Qué es un electrón? Ni lo sé, ni me importa, ni quiero saberlo. Eso si, el electrón se comporta como..."

Hermano Adalberto, profesor de física en el colegio La Salle de Alcoi durante mi bachillerato, a quien me veo en la obligación de dedicarle este trabajo.

"A physicist is always guided by the minimum energy principle: He thinks about what he is going to do and why he is going to do it. Afterwards he designs the way to do it with the minimum effort."

"What is an electron? Nor I know it, nor I care about it, nor I want to know it. But, nevertheless, an electron behaves like..."

Brother Adalberto, teacher of physics in La Salle school of Alcoi during my bachelor, to whom I feel obliged to dedicate this work.

Contents

List of Figures

List of Abbreviations

AOM	Acusto Optic Modulator
APD	Avalanche PhotoDiode
CW	Continuous Wave (excitation)
FSS	Fine Structure Spplitting
FWHM	Full Width Half Maximum
FWM	Four-Wave Mixing
GS	Ground State
GTI	Gires-Tournois Interferometer
IPL	Integrated Intensity Photoluminiscence
QD	Quantum Dot
QW	Quantum Well
QWr	Quantum Wire
PL	PhotoLuminescence
PLE	Excitation PhotoLuminescence
LGR	Low Growth Rate
MBE	Molecular Beam Epitaxy
MEM	Master Equation Microstate
MOCV	Metal Organical Chemical Vapor Deposition
MFD	Mode Field Diameter
NIR	Near Infrared
OPO	Optical Parametric Oscillator
SOA	Semiconductor Optical Amplifier
RE	Rate Equations
TRPL	Time Resolved Photoluminescence
TCSPC	Time Correlated Single Photon Counting
WL	Wetting layer
A^-	Acceptor
D^+	Donnor
e^-	electron
h^+	hole
ICMUV	Institut Ciències dels Materials de la Universitat de València

Chapter 1

Introduction

As I went deep into my study on "Confined Exciton Recombination Dynamics on In(Ga)As Quantum Nanostructure", I felt fascinated by the great, long and fruitful relation between Semiconductor physics and Optical Spectroscopy. The development of these two different research fields surpasses the simple relation between the subject of the study and the technical tools employed for it; there is a potent feedback between the knowledge generated and the improvement of the technical resources available. Most of the properties of bulk semiconductors, namely band structure, phonons, plasmons, single-particle spectra or defects, have been extensively studied through linear optical spectroscopy (absorption, reflectivity, photoluminescence or Raman). Moreover, the appearance of picosecond and femtosecond pulsed lasers allowed the access to nonequilibrium, nonlinear and transport properties: the development of ultrafast optical spectroscopy techniques covered the different time scales that defined the relaxation of photoexcited semiconductors.[1]

Carrier recombination and part of the capture processes can be measured through direct photoluminescence detection; nowadays fast photodiodes are capable of detecting low signals while providing a time resolution in the range of some picoseconds. But, when we focus our interest in the fastest processes, more time resolution is needed: pump and probe or time-gating up-conversion provide resolutions up to the full width half maximum (FWHM) of the laser pulses used.

The leap to fast optoelectronic devices came with the development

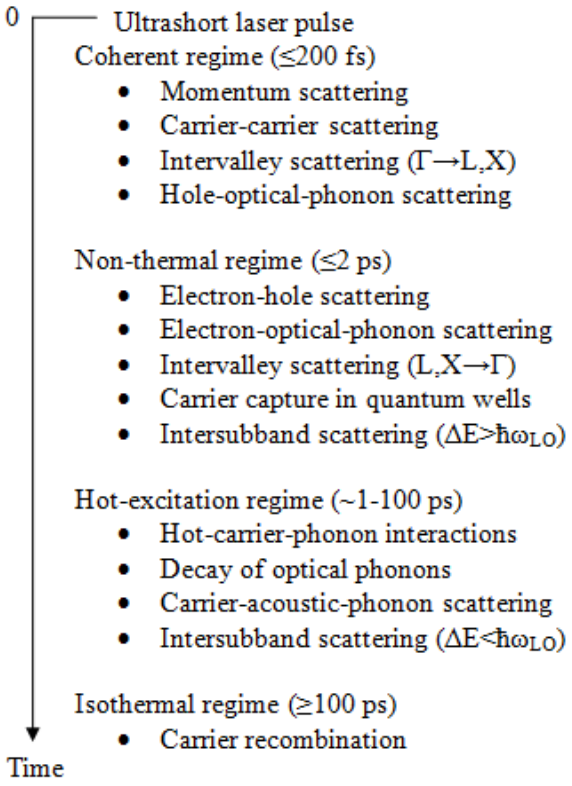

Figure 1.1: **Four temporally-overlapping relaxation regime in photoexcited semiconductors, with some typical scattering and relaxation processes for each regime. Taken from [1]**

of the semiconductor heterostructures (a semiconductor structure that is composed of layers of two different semiconductor materials with different band gaps), and it was worth the physics Nobel prize given to Zhores Ivanovich Alferov and Herbert Kroemer in 2000.

In extremely thin layers, when the thickness is comparable to the carrier vector wavelength, its kinetic energy becomes quantized. This quantum confinement leads to a complete change in the energy states distribution. Furthermore one can progressively extend this concept to more spatial directions, creating nanostructures with two (quantum wires) or even three

confined dimension (quantum dots).

In this work, ultrafast techniques have been applied to the study of In(Ga)As Quantum Dots (QDs), III-V semiconductor nanostructures that confine the carriers in all three dimensions. Convenient models have been developed to understand different relaxation and recombination processes involved in each case.

First we show and discuss experimental data on unprocessed samples and collective measurements; the excitonic dynamics in ensembles of different shape nanostructures is measured through time resolved photoluminescence (TRPL) experiments: we can relate effective lifetime behavior as a function of temperature and power to their different electronic structure.

Afterwards, confocal microscope measurements on low QD density samples are analyzed, while developing a theoretical background for the recognition of the different excitonic species based on a microstate approach. Time resolved micro photoluminescence is collected on a single quantum dot, and the competition among the different excitonic species is analyzed.

Crossing the bridges between basic research and technological applications, we've performed time resolved measurements in the active medium of a QD based Semiconductor Optical Amplifier (QD SOA). Electrical instead of optical pumping makes a big difference with previous experiments: the main part of the gain recovery dynamics takes place in a sub-picosecond or picosecond range.

The heterodyne pump and probe technique employed in our experiments provides a way to study the propagation of collinear laser pulses in the waveguide of the SOA with a time resolution in the range of 150 fs (the FWHM of the pulse employed). In order to test the physical limits of the time response of the device, two Michelson interferometers have been placed at the entrance of the setup, creating a small "pulse train" composed by up to four replicas of the original pulse. Modeling of these experiments lead to a reinterpretation of the capture in electrically pumped QDs, we find out that the ground state of the QDs can be directly refilled from the high energy reservoirs in the systems, providing an alternative path to the refilling just through the excited states level of the quantum dot.

Chapter 2

Introducción

A medida que profundizaba en mi estudio “Dinámica de la recombinación de excitones confinados en nanostructuras cuánticas de In(Ga)As.”, me sentí fascinado por la gran, larga y fructífera relación entre la física de semiconductores y la espectroscopía óptica. El desarrollo de estos dos campos de investigación sobrepasa la simple relación entre el tema de estudio y las herramientas técnicas empleadas para ello; hay una potente retroalimentación entre el conocimiento generado y la mejora de los recursos técnicos disponibles. La mayoría de las propiedades de los semiconductores masivos, por ejemplo, la estructura de bandas, fonones, plasmones, espectros de una partícula o defectos, han sido extensivamente estudiados através de métodos de óptica lineal (absorción, reflectividad, fotoluminiscencia o Raman). Además, la aparición de láseres pulsados en el rango de los picosegundos y los femtosegundos permitió el acceso a situaciones de no-equilibrio, propiedades no-lineares y de transporte: el desarrollo de las técnicas de espectroscopía óptica ultrarápida cubrió las diferentes escalas temporales que definen la relajación de semiconductores fotoexitados[1].

La recombinación de portadores y parte del proceso de captura pueden ser medidos através de la detección directa de fotoluminiscencia; actualmente los fotodiodos rápidos son capaces de detectar señales bajas mientras permiten una resolución temporal en el rango de algunos picosegundos. Pero, cuando nos centramos en procesos ms rápidos, necesitamos más resolución temporal: las técnicas “pump and probe” or “time-gating up-conversion” permiten resoluciones hasta la anchura a media altura de los pulsos láseres

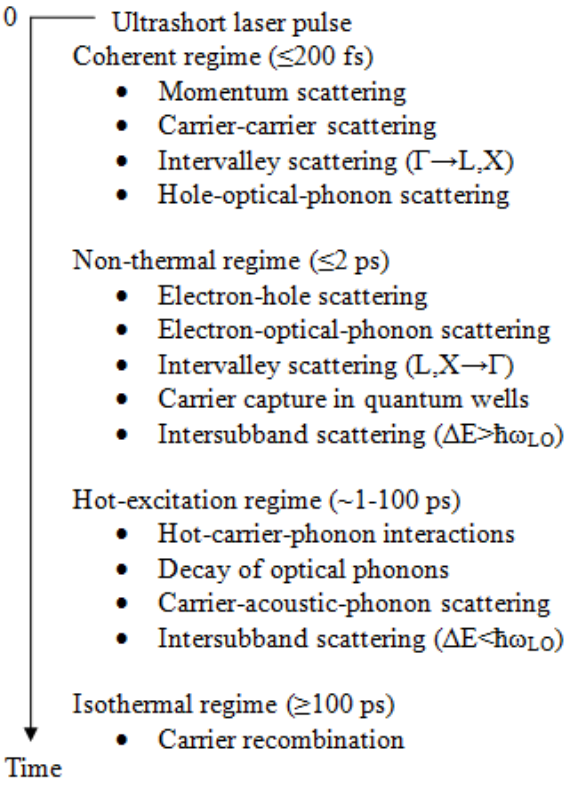

Figure 2.1: **Las cuatro regímenes temporalmente sobrepuestos en semiconductores fotoexcitados, con los processos de "scattering" y relajación típicos para cada uno. Tomado de** [1]

empleados.

El salto hacia los dispositivos optoelectrónicos llegó con el desarrollo de las heteroestructuras semiconductoras (un estructura semiconductora compuesta por capas de dos materiales semiconductores distintos con diferentes separaciones de banda), esto conllevó el premio Novel de física para Zhores Ivanovich Alferov y Herbert Kroemer en el 2000.

En capas extremadamente delgadas, cuando la anchura es comparable al vector de ondas de los portadores, su energía cinética se cuantiza. Este confinamiento cuántico conlleva un cambio completo de la distribución

energética de estados. Más aún, uno puede extender progresivamente este concepto a más direcciones del espacio, creando nanoestructuras con dos (hilos cuánticos) o incluso tres dimensiones confinadas (puntos cuánticos).

En este trabajo, hemos aplicado técnicas ultrarápidas de espectroscopía óptica al estudio de puntos cuánticos de In(Ga)As, nanoestructuras semiconductoras III-V que confinan los portadores en las tres dimensiones. Hemos desarrollado los modelos adecuados para comprender los diferentes procesos de relajación y recombinación en cada caso.

Primero, mostramos y discutimos datos experimentales en muestras no procesadas y medidas sobre colectivos; la dinámica excitónica en colectivos de nanoestructuras con distintas formas se ha medido a través de experimentos de fotoluminiscencia resuelta en tiempo (TRPL): Podemos relacionar el comportamiento del tiempo efectivo de vida en función de la temperatura y la potencia con su estructura electrónica distinta.

Después, se analizan medidas de microscopía confocal en muestras de baja densidad, mientras se desarrolla un sustrato teórico para el reconocimiento de las distintas especies excitónicas basado en microestados. Se colecta la micro-fotoluminiscencia resuelta en tiempo de un punto cuántico aislado y se analiza la competición entre las distintas especies excitónicas.

Atravesando los puentes entre la investigació fundamental y las aplicaciones técnicas, hemos realizado estudios resueltos en tiempo en el medio activo de un amplificador óptico semiconductor basado en puntos cuánticos (QD SOA). La inyección eléctrica en vez de óptica marca una gran diferencia con los experimentos anteriores: la mayor parte de la recuperación de la ganáncia óptica sucede en una escala en o por debajo del picosegundo.

La técnica de "pump and probe" heterodina empleada en nuestros experimentos permite el estudio de la propagación de pulsos colineares en la guía de ondas del SOA con una resolución en el rango de los 150 fs (la anchura a media altura de los pulsos empleados). Modelar estos experimentos conlleva una reinterpretación de la inyección electrica en puntos cuánticos, encontramos que el estado fundamental de los puntos cuánticos puede ser directamente realimentado desde reservorios de alta energía, proporcionando un camino alternativo a la realimentación solo através del estado excitado del punto cuántico.

Chapter 3

Basic fundamentals

In this chapter we will briefly introduce some of the basic concepts on semiconductor physics, afterwards, we will apply them to our particular system, In(Ga)As quantum dots, fixing a theoretical framework to motivate, discuss and analyze our experiments.

Two different approaches to the description of the QD dynamics will be discussed, their conceptual differences will be pointed out while determining their strengths and suitable applications. Both approaches will be used to interpret the phenomenology observed in the following experimental chapters, rate equation approach when dealing with ensembles of QDs and microstate theory applied to Single QD experiments.

3.1 Semiconductor and Semiconductor Nanostructures

A semiconductor is a solid whose electrical conductivity is in between that of a conductor and that of an insulator. Semiconductors have a crystalline structure: the unit cell (Figure 3.1 left) is repeated periodically, and, as a result, carriers experiment periodic electrical potentials. The electronic wave functions can be described by means of periodic functions (Bloch functions) and used to obtain the electronic band structure through very different theoretical or pseudo-experimental methods like tight-binding or $\overrightarrow{k}\overrightarrow{p}$ [2].

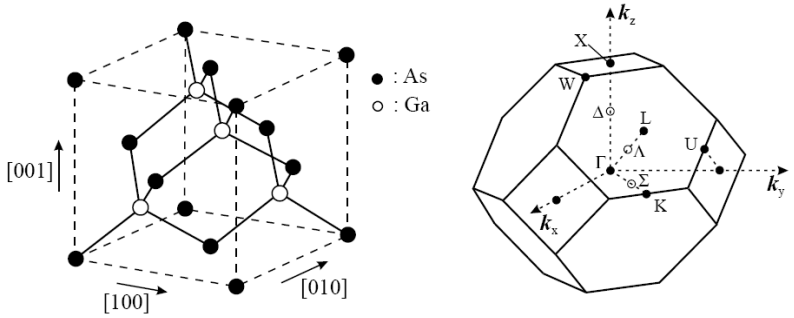

Figure 3.1: **Left: Unit cell of the Bravais lattice of a zinc-blende structure, e.g. of GaAs. Right: First Brillouin-zone of the reciprocal zinc-blende lattice.**

Most semiconductors present a moderate energy gap (0.5-3.5 eV) between the conduction and valence bands. At zero Kelvin, the valence band of a perfect semiconductor crystal is completely full while conduction band is completely empty: there are no available carriers in the conduction band and the semiconductor behaves like an insulator. In contrast, at room temperature, a thermal carrier distribution populates the conduction band and, consequently, a typical low conductivity is measured. This conductivity can be easily controlled by adding impurities. Acceptor impurities induce hole conduction and donor impurities electron conduction.

Even if the full electronic band structure is rather complex, with different energy band dispersions ($E(\overrightarrow{k})$) at different crystalline directions, most of the direct semiconductor properties can be described reducing the whole band structure to a simplified band structure around the center of the Brillouin zone, the Γ-valley; as shown in figure 3.2 for GaAs, the semiconductor matrix where all the nanostructures studied in this work are embedded.

The parabolic approximation is the simplest one, describing an electron in the conduction band with an effective mass (m_{e^*}). The lack of an electron in the valence band is described as a "hole", and due to the presence of two different bands in the Γ point, two different kinds of holes are defined, heavy and light holes, whose different effective masses come from the different bending of these two valence bands. While a photon

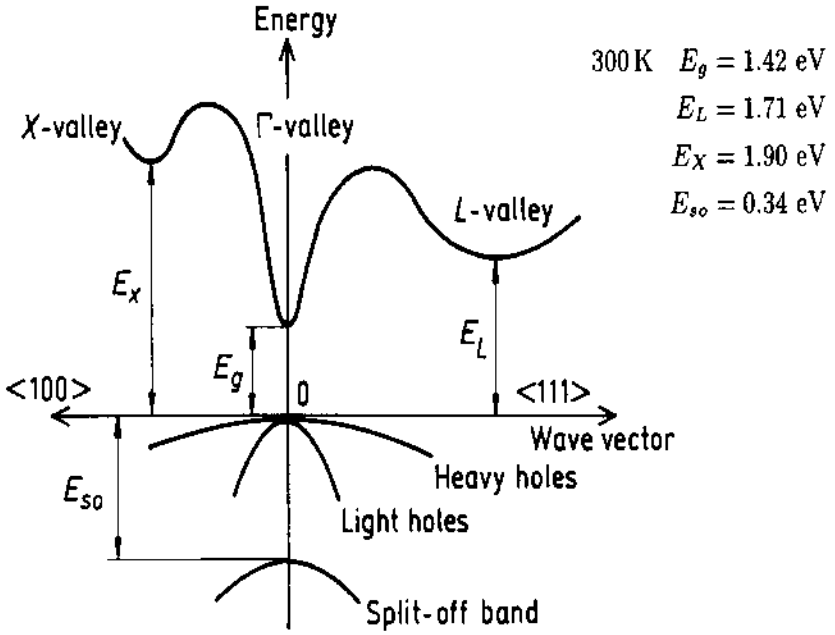

Figure 3.2: **Simplified Band structure of GaAs at 300K** [3]

with energy below the band gap (E_g in the diagram) cannot be absorbed, a photon with energy above the gap pulls out an electron from the valence band to the conduction band, leaving a "hole" in the process. If electron (e^-) and hole (h^+) remain correlated through coulomb interaction, the optical excitation can be described by only one quasi-particle, the exciton (X). Once the crystal is excited, it tends to relax that excess of energy until returning to the original crystal ground state. Depending on the nature of these relaxation channels, we find non-radiative processes (phonon emission, carrier scattering...) or radiative processes: electron and hole recombine emitting a photon with energy equal to their transition energy.

3.1.1 Quantum confinement

Semiconductor Nanostructures are low dimensional systems that result from reducing at least one of the dimensions of a semiconductor to the nanometric scale. Quantum confinement effects appear when the wave-

length associated to the energy transition is lower than the physical dimensions of the nanostructure (L in Figure 3.3), reducing the available energy level and modifying the density of states.

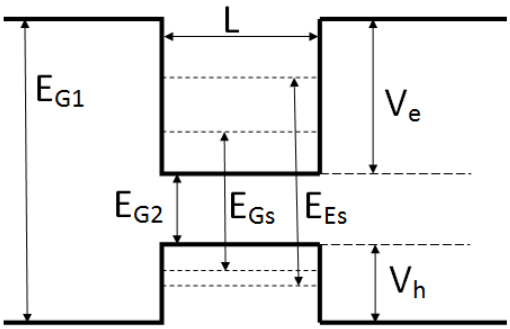

Figure 3.3: **1-D Quantum Well sketch. $\mathbf{E}_{g1}$ and $\mathbf{E}_{g2}$ are the Bandgaps of the two semiconductors; $\mathbf{V}_e$ and $\mathbf{V}_h$ stand for the different band offsets that confine electrons and holes, respectively, while L is the Well length.**

In a massive semiconductor or a three dimensional structure, the density of states is expressed like:

$$\frac{\mathrm{d}N}{\mathrm{d}E} \propto \frac{\mathrm{d}}{\mathrm{d}E}\left(E - E_g\right)^{\frac{3}{2}} = \left(E - E_g\right)^{\frac{1}{2}} \tag{3.1}$$

Where E_g stands for the gap energy difference. Epitaxial growth methods (like Molecular Beam Epitaxy (MBE) or Metal Organical Chemical Vapor Deposition (MOCVD)) allow the combination of different energy bandgap materials without losing the crystallity of the resulting solid; growing a thin layer of a lower band gap semiconductor in a higher band gap matrix is now a standard way to obtain quantum wells (QW), a one dimension confined nanostructure that presents a step-like density of states:

$$\frac{\mathrm{d}N}{\mathrm{d}E} \propto \frac{\mathrm{d}}{\mathrm{d}E}\sum_{\varepsilon_i<E}\left(E - \varepsilon_i\right) = \sum_{\varepsilon_i<E} 1 \tag{3.2}$$

Different growth (Stansky-Krastanov self assembling) or processing (lithographic...) techniques can reduce the dimensionality of the final nanostructures [4]. In the case the final structure has two dimension below the De-Broglie wavelength that the excitons mainly determined by the electrons,

we are dealing Quantum Wires (QWr), whose density of states obeys the following expression:

$$\frac{\mathrm{d}N}{\mathrm{d}E} \propto \frac{\mathrm{d}}{\mathrm{d}E} \sum_{\varepsilon_i<E} (E-\varepsilon_i)^{\frac{1}{2}} = \sum_{\varepsilon_i<E} (E-\varepsilon_i)^{-\frac{1}{2}} \tag{3.3}$$

Extending the confinement to all three dimensions, we have quantum dots that exhibit a delta like density of states:

$$\frac{\mathrm{d}N}{\mathrm{d}E} \propto \frac{\mathrm{d}}{\mathrm{d}E} \sum_{\varepsilon_i<E} \Theta\left(E-\varepsilon_i\right) = \sum_{\varepsilon_i<E} \delta\left(E-\varepsilon_i\right) \tag{3.4}$$

There is a striking difference in their densities of states, as plotted in Figure 3.4. The large density of states concentrated at a given wavelength can be used to increase the performance of laser and optoelectronic devices [5]. The development of quantum well based lasers is in a commercial stage; while recent research has actually achieved better performances in QD based devices[6] and opened the doors to new and exciting applications[7], like, for example, single photon emitter for quantum cryptography.

3.1.2 Quantum Dot electronic structure

The three dimensional confinement of a QD results in an atom-like structure. To calculate the electronic structure of a real QD, very different aspects have to be taken into account: shape, composition profile (intermixing between the QD and the matrix materials leads to a gradient along the structures), piezoelectric effects or stress fields bending the semiconductor band.

Self Assembled Quantum Dots are obtained by the growth of a semiconductor material exhibiting a mismatch in the lattice parameter with respect to the substrate. This situation enables the growth mode named Stranski-Krastanov. The stress accumulated when growing an epitaxial layer of the larger lattice parameter material over the seed matrix relaxes strain by forming isolate islands, standing on a planar and thin layer of the same material, the Wetting layer (WL). Energetically, this layer provides a QW-like level between the conduction band of the barrier material (usually the matrix) and the confined levels of the QDs. The role of the WL

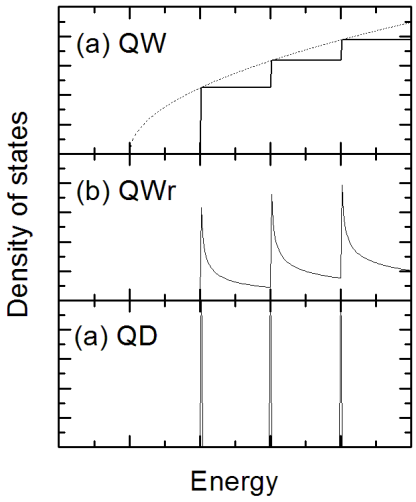

Figure 3.4: **Density of states for (a) semiconductor bulk (dashed line) and a Quantum Well (solid line), (b) Quantum wire (c) Quantum Dot**

in the overall energetic picture and the dynamics of the system is relevant and will be discussed further in the next chapters.

The shape and composition of the final nanostructures depend on the growth conditions: substrate temperature, thickness of the deposited layer, atmosphere... and these slightly vary from QD to QD in the ensemble.

Different complex models have been developed under the assumption of particular shapes (pyramids and lens are the most popular ones) and measured or calculated composition gradients and stress fields. The experience, effort and calculation power needed to get the electronic structure by any of the established methods ($\overrightarrow{k}-\overrightarrow{p}$ 8 bands, tight binding..) is very high for most of the nanostructures we work with, given the strange non standard shape and size (quantum dashes, quantum camels or quantum rings) or the lack of an accurate composition, shape and dimension characterization.

In order to combine experimental measurements on QD dynamics with their optical characterization, manly energetic positions and degeneracy of

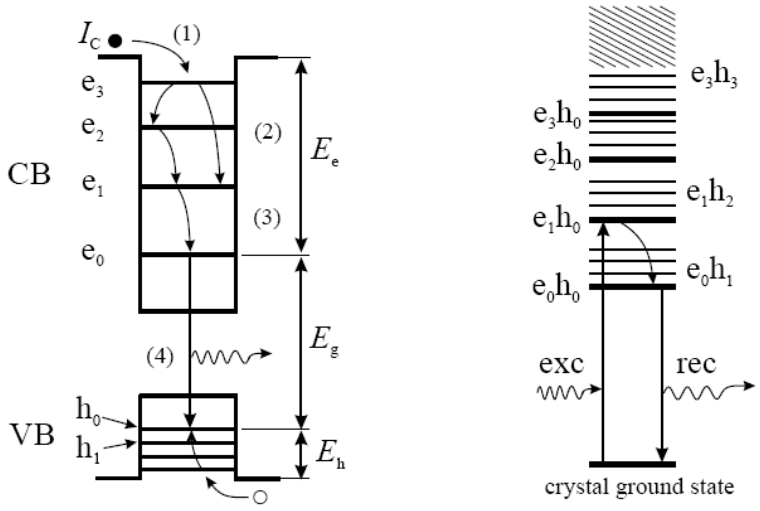

Figure 3.5: **Energy level scheme for electrons and holes (left) and for electron-hole pairs(right). Different steps of relaxation are indicated by arrows, e_i, h_i denote electron and hole levels, CB: conduction band, VB: valence band, exc: excitation, rec: recombination. The hatched area indicates a continuum joint density of states. Electrons are indicated by closed circles, holes by open circles[8].**

the different confined levels are needed.

For small QD structures, where the semiconductor free Wannier-Mott exciton length is well below the length of confinement, a really simple approach (in the frame of the Effective Mass Adiabatic model) can be applied: The height of a self assembled QD, in the growth direction (**z**), is really lower than the planar (**x-y**) dimensions; that allows to treat the problem as two uncoupled harmonic oscillators. The lower one, in the **z** direction determines the position of the ground states (GS) while the 2-D harmonic oscillator in the **x-y** is the main responsible of the rest of the electronic structure, including the energy difference between excited states (ES) and the nature and degeneracy of the confined levels: GS is s-like and doubly degenerated (due to spin), the first ES is p like and four times degenerated (spin included)...

As shown in Figure 3.5, depending on the strength of the Coulomb

correlation between e^- and h^+, one can treat optical or electrical excitation as excitons or as uncorrelated particles. The non-equilibrated capture of an e^- (h^+) excess leads to the formation of a charged exciton, negative,X^- (positive, X^+). If two excitons populate the GS (two e^- and two h^+) a biexciton (XX) is formed. Following the same reasoning, if the QD level, or a higher one, can accept more carriers higher charged quasiparticles can be created. This change in the occupancy of the QD levels is reflected in a different transition energy of the corresponding quasiparticle, other than minor effects like screening, strain and piezoelectric field changes, determining a rich electronic fine structure to the QDs, as shown in Figure 3.5.

Not all e^- and h^+can recombine: the interband selection rules of the confined levels avoid the radiative recombination of some combinations (a p-electron and a s-hole, for example); this non-radiative states are called dark states and, obviously, can not be observed directly through spectroscopy.

3.1.3 Quantum dot ensembles

The photon emission out of a single, isolated, quantum dot at low temperatures is really sharp. The homogeneous linewidth (Γ) of a single QD transition has been measured by Single QD spectroscopy[9], cathodoluminiscence[10] or absorption combined with Stark effect based measurements[11], finding a variety of values between 1 and 20-30 μeV. In a two level system approach, one can establish a relation between Γ and the exciton dephasing time, T_2, given by $\Gamma = 2\hbar/T_2$. Then, at low temperatures T_2 is in the range 100-1000 ps, that is, limited by the exciton lifetime. Since the QDs can be designed to have a confined level splitting of up to 100 meV, the structures may be addressed by sub-100 fs pulses without exciting energetically higher lying states. Hence it might be possible to perform up to $\approx 10^4$ coherent optical manipulations on the QD ground-state exciton before decoherence could destroy the possible optical information[12].

But when the spatial resolution of the measurement does not allow to isolate the emission from only one QD, the size, shape and composition fluctuations inherent to the self-assembling growth method broadens the

spectra. Normally these fluctuations can be accounted for by a gaussian distribution and, as a result, the optical properties measured are the convolution of the single QD emission and that gaussian distribution due to changes on the QDs dimensions.

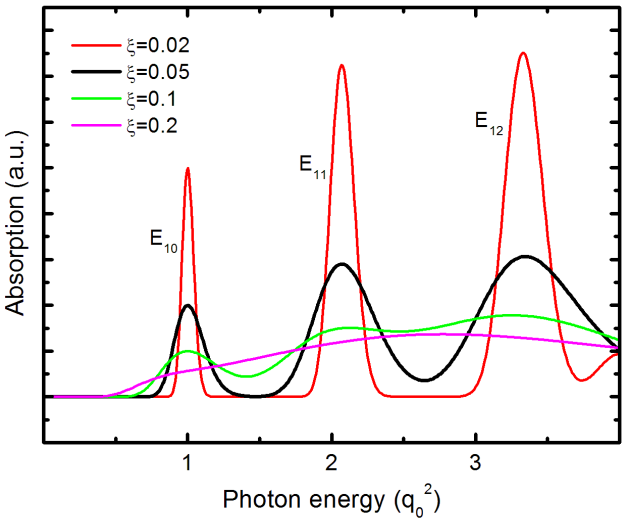

Figure 3.6: **Absorption of an ensemble of quantum spheres exhibiting a gaussian distribution of radii characterized by different standard deviations** (ξ)

As can be observed in Figure 3.6, a broad size distribution masks the observation of single quantum dot optical properties. Basically, the broad size distribution determines the inhomogenous linewidth associated to the emission of a QD ensemble.

3.2 Modeling the excitonic dynamics on Quantum Dots

In this section, we would briefly introduce two different approaches to the description of the dynamics on QDs. Even if both models are not

formally equivalent, they converge in most of the cases, offering compatible solutions.

3.2.1 Rate equation approach

Rate equations (RE) are used in many different physical systems and Semiconductor Physics has widely used them in the analysis of carrier recombination under both, bulk and quantum well systems. With the appropriated adjustments, in particular Pauli blocking inclusion, RE can be extended to the treatment of QD ensembles: they provide a simple description that is analytically solvable in some particular cases.

If we consider the average level population in a QD ensemble, we can establish simple relations between the different population probabilities (f_i) and the rates of relaxation, capture, escape and recombination among them. Following the discussion in references [13, 4], a two level rate equation system adapted to QDs, as simple as shown in 3.7 (a), is described as:

$$\frac{df_2}{dt} = -\frac{f_2}{\tau_r} - \frac{f_2\,(1-f_1)}{\tau_0} + G, \tag{3.5}$$

$$\frac{df_1}{dt} = -\frac{f_1}{\tau_r} + \frac{f_2\,(1-f_1)}{\tau_0}, \tag{3.6}$$

G stands for the generation rate and τ_r and τ_0 are the radiative (supposed the same for both levels) and relaxation times, respectively. Pauli blocking is included through the term proportional to $(1-f_1)$ that avoids the *overfilling* (average population above 1) of level 1, while converting the system into a non linear one. Some other key simplifications like low temperature (scape of excitons is not considered) or just one exciton confined in level 1 have been included the picture represented by 3.5.

The concrete RE system used depends on the particularities of the physical system under study. Excitonic pictures are useful when the binding energy of the exciton is greater than or in the range of the thermal energy (k_bT) associated to the experiment. Given that the exciton binding energy is in the range of 25-50 meV [14], room temperature experiments make necessary to consider separate and non equilibrated capture of e^- and h^+. In this case a two-particle picture is preferable.

3.2.2 Master equation for microstates

Instead of dealing with average populations, the Master Equation for Microstates (MEM) approach deals with the amount of QDs that can be found in a particular electronic configuration (population and level distribution): a microstate. The concept of microstate can be directly connected with the before defined quasiparticles (X, X^-, X^+, XX and higher charged ones) but, as we will explain later, some special cases have to be considered, in addition.

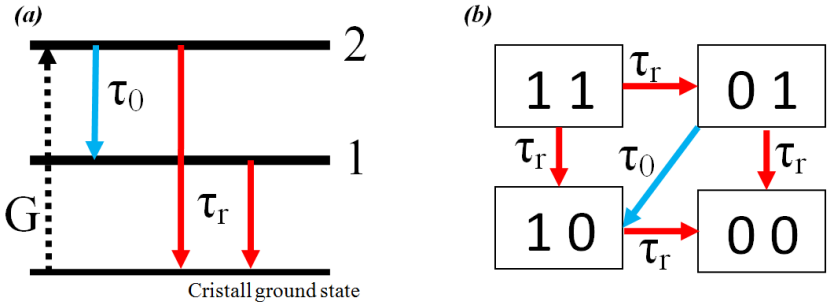

Figure 3.7: **Diagram of the (a) Rate Equation model and (b) Master Equation for Microstates in a two level system.**

As in atoms, a QD can be identified by its quantum numbers. To name a QD, a microstate label is defined using this concept: $[n_{GS},n_{ES1},n_{ES2}...]$, where $n_i = 0, 1, \ldots, d_i$ is the population in every confined level of the QD and d_i is the degeneracy of state i. Long before any excitation, an ensemble of QDs is "empty", that is, no excitons, electrons or holes are "captured" in any of the QDs. All QDs can be found in the [0,..,0] microstate, and the sum of all that empty microstates is equal to number of QDs in the ensemble (N_{QDs}). Capture, escape, radiative or non radiative relaxation of excitons in the ensemble just transform one microstate into another, so the sum of all microstates is always preserved as N_{QDs}. Figure 3.7(b) represent the equivalent system of Figure 3.7(a) in the MEM model, labeling the different microstates as $[n_1,n_2]$. Instead of two differential equations, MEM gives four:

$$\frac{n_{0,0}}{dt} = \frac{n_{1,0}}{\tau_r} + \frac{n_{0,1}}{\tau_r}, \tag{3.7}$$

$$\frac{n_{1,0}}{dt} = -\frac{n_{1,0}}{\tau_r} + \frac{n_{1,1}}{\tau_r} + \frac{n_{0,1}}{\tau_0}, \tag{3.8}$$

$$\frac{n_{0,1}}{dt} = -\frac{n_{0,1}}{\tau_r} + \frac{n_{1,1}}{\tau_r} - \frac{n_{0,1}}{\tau_0}, \tag{3.9}$$

$$\frac{n_{1,1}}{dt} = -2\frac{n_{1,1}}{\tau_r} \tag{3.10}$$

The main feature MEM provides is that *Pauli-blocking* forms part of the approach, it is a *"built in"* characteristic instead of included. Excited state population before the exhaustion of the ground state is the main striking result; it comes from the random capture process, inherent to the MEM approach, but hard to include in the RE approach; Monte Carlo simulations have been used in the bibliography [15]. Conceptually and mathematically both RE and MEM are not equivalent, even if they try to describe the same "problem". Sometimes both offer similar results when applied to a particular situation [16]. MEM describes better the special characteristics of QDs, but the systems of differential equations that gives have to be solved numerically, and does not provide direct results for some "measurable" constants (decay times can be directly obtained in the RE approach, but MEM calculates only the transitories, which eventually can be fitted to monoexponentials like in the experiments). The dilemma of simplicity and straight-forward physical interpretation versus conceptual correctness has to be considered in every concrete experimental situation.

3.3 Electric field and Temperature effects on QDs

Optical properties of QDs are affected by external fields (electric and magnetic) and temperature. In this section we summarize some of this effects, as they constitute part of the theoretical framework in which the posterior experimental results will be discussed. We center our attention on temperature an electric field effect, both directly affecting the present work, even if magnetic field is a powerful tool to study the intrinsic properties and fine structure of QDs [17, 14].

3.3.1 Temperature dependence of semiconductors band gaps

As temperature increases, bandgap in semiconductors experiments a red-shift; this behavior is usually fit by the semi-empirical Varshni's law:

$$E_g(T) = E_g(0) - \frac{\alpha_1 T^2}{T + \alpha_2} \tag{3.11}$$

The origin of this effect has to be found in the interaction of phonons: an increase in temperature changes the chemical bonding as electrons are promoted from valence band to conduction band, but, in the intrinsic temperature range direct effects due to thermal band-to-band excitations are negligible. The lattice phonons, on the other hand, have relatively small energies and are excited in large numbers at moderate temperatures. They influence the bonding through various orders of electron-phonon interaction[18]. Some equation proposals that directly take into account phonon distributions can be found in the literature[18]. QD emission suffers the same kind of effects as bulk semiconductors[19].

3.3.2 Linewidth evolution with temperature

The temperature dependence of the homogeneous linewidth $\Gamma(T)$ of an exciton is determined by its interaction with phonons. It is given by the probability for the exciton to scatter from the ground shell to higher lying states[12], and it depends on the phonon population. For higher dimensionality systems, Γ is governed by:

$$\Gamma(T) - \Gamma(0) = \gamma_{ac} T + \gamma_{op} \frac{1}{e^{\hbar\omega_{LO}/k_b T} - 1} \tag{3.12}$$

At low temperatures a sharp line characterizes the emission of QDs, like occurs in atoms (this is the reason by which QDs are often called "artificial atoms"). When increasing temperature, Γ broadens due to the availability and occupation of higher energy states due to scattering with acoustic and optical phonons reaching values around some meV for room temperature (dephasing times below 500 fs)[12, 20].

3.3.3 Exciton capture and relaxation

The discrete nature of the excitonic levels in a QD lead to the prediction of a "phonon bottleneck"[21, 22]: a slow capture process caused by the need of an exact optical phonon amount equal to the energy splitting between the original and the final states. Experimentally, only few experiments showed slow capture processes in QDs, and different theoretical hypothesis were proposed to relax the "phonon bottleneck" restrictions, for example, scattering by acoustic and optical phonons simultaneously[23]. The participation of acoustic phonos softens the restrictions for energy relaxation, opening energetic windows and allowing a faster relaxation. Some theoretical treatments describe QD electronic states and phonons as a new quasiparticle, the "polarons" based on a really strong e^--phonon interaction[24]. Other authors consider Auger-like processes[25], and even the existence of a continuum of states, energetically close to the confined levels, that offers a relaxation path until the final LO phonon emission[26]. Depending on the nature of the excitation, mainly determining the non equilibrium population, many differences can be observed in the QD capture dynamics[27]. In differential transmission pump and probe experiments, at really low pumping ratios, two different dynamics are observed[15]. Non-resonant absorption generates an e^--h^+ pair at the GaAs barrier, namely "far away" from the QDs. Given that e^- has greater mobility than h^+, they can be trapped either in a correlated way (geminate capture(Figure 3.8)) or an e^- can be captured alone (non geminate capture). The last situation leads to the observation of a slow dynamics in the transmission dynamics, given that the e^- in the configuration of non-geminate capture cannot relax radiatively.

3.3.4 Thermal distribution and scape

At low temperatures, QDs can be considered energetically isolated and no redistribution channel allows connection between them (tunneling in high density samples excluded). It is through the increase of temperature, when the exciton can reach the kinetic energy to populate the WL, a common 2-D level for all QDs in the ensemble that acts like contact between them. Due to the discrete distribution of energetic levels it was predicted that QD laser would be characterize by a great stability and insensitivity

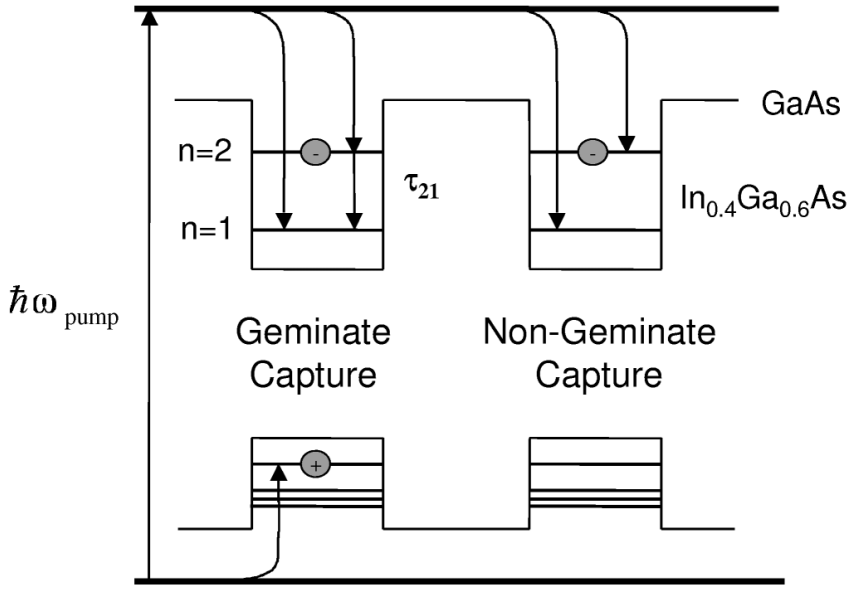

Figure 3.8: **Carrier capture model with geminate and nongeminate capture configurations. Taken from [28]**

to temperature. However, QD lasers do not reach their expected gain at room temperature due to thermal redistribution of carriers between their levels and, particularly, because the wetting layer takes part of that population, saturating the inversion of population in the confined levels.[29]. The escape time (τ_e) out of a localized trap, without any extra loss term) takes the form[30]:

$$\tau_e \approx \tau_{loc} e^{-\frac{E_{loc}}{k_b T}} \tag{3.13}$$

The Boltzmann factor, $e^{-\frac{E_{loc}}{k_b T}}$, is the ratio of the occupation probabilities between two given states in thermal equilibrium and can be used as the starting point to derive a Maxwell-Boltzmann or a Fermi-Dirac distribution. If recombination processes are slow compared with capture and scape, a detailed balance of thermal equilibrium dynamics in QDs leads to similar relations between the confined levels[31]. QD Pumping, electrical or optical, modifies the equilibrium condition and, as a consequence the temperature of the QD system. For example, transient excitation can derive in a small perturbation of the equilibrium whereas stationary pump-

ing can "heat up" not only the electronic temperature but also the lattice temperature, which is normally lower than the carrier one.

3.3.5 Quantum confined Stark shift effect

In the vertical direction, there are slightly different confining potentials for electrons and holes leading to a spatial separation of the electron and hole wave functions, i.e., a permanent dipole moment. In addition, the exciton has a polarizability, the extent to which an applied electric field can pull the electron and hole apart, reducing their total confinement energy. Both parameters are important. The permanent dipole moment influences the excitonic oscillator strength and in addition, it is sensitive to the detailed structure of the dots. The polarizability determines the sensitivity of the exciton energy to an electric field, effect that is known as quantum confined Stark Shift effect.

InAs quantum dots in GaAs have a permanent dipole moment compatible with an electron-hole separation of about 0.4 nm; the hole localized at the apex of the dot, above the electron whose wave function is spread over the entire dot[32] . The sign of this dipole moment has been interpreted as an evidence of a strong indium concentration gradient, with the apex indium-rich and the base indium-poor, and, also to a truncation of dotsafter GaAs capping.

The PL energy can always be fitted accurately to a quadratic function of the applied voltage, exactly as expected for an induced dipole under the effect of an external electric field. Overgrown samples with unusual shapes, like the ones studied in chapter 5 can present a higher built-in dipole moment[33].

The radiative lifetime (inverse of the oscillator strength) variation follows the inverse behavior of the e^{-}-h^{+} separation and it depends on the nanostructure and its intrinsic dipole moment: an external voltage can enhance (reduce) the oscillator strength depending if its applied forward (reverse) to the intrinsic dipole moment in the growth direction. The observed lifetime is a combination of two effects: Quantum Confined Stark Effect on the radiative lifetime and tunneling, as explained in a recent work developed in our group[34].

Chapter 4

Experimental techniques

In this chapter we will describe the experimental setups employed in the measurements that constitute this Ph.D work. Their peculiarities and characteristics are discussed while remarking the spectral, spatial and temporal resolution obtained. In addition, we will briefly introduce the physical background of the pulsed sources and detectors used.

4.1 Macroscopic measurements

Self assembled QDs samples present different dot areal density depending on the growth conditions (like in the shape and size dispersion case); low density samples, like the ones used in chapter 6 can offer densities below ten QD per μm^2; this low density offers the chance to study isolated QDs using high spatial resolution technics (like confocal microscopy, see section 4.2).

In contrast, high density samples, like the ones used as active medium in QD based lasers, present areal densities as high as 10 thousand QDs per μm^2 and the optical properties of only one QD cannot be experimentally isolated (ie. confocal microscopy). In the characterization of an ensemble of QDs, the required spectral resolution is not high, given the inhomogeneous broadening introduced by QD size fluctuations (section 3.1.3). Different spectral shapes can be measured in the same sample depending on its homogeneity and the diameter of the excitation-collection spot, but

this is not the usual case.

In order to work at low temperatures, samples are placed in the cold finger of a commercial compressed helium cryogenerator having a heater and a thermometer for temperature control from 10 K to room temperature. The excitation/collection optics is placed out of the cryogenerator, because a near infrared (NIR) transparent window separates the cryogenerator from the ambient.

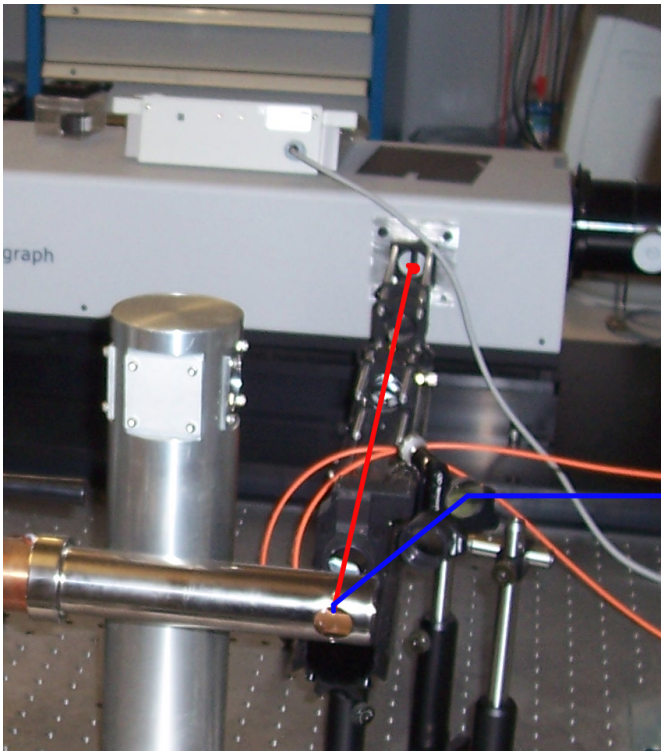

Figure 4.1: **Set-up for macro characterization of the QD samples. Blue line refers to the excitation path, red light to the main collection axis. All beams remain in a plane parallel to the optical table.**

The set-up shown in Figure 4.1 offers a simple and versatile way to perform different photoluminescence experiments keeping the collection-excitation spot in the same sample point, a critic issue that assures that one is working with "exactly" the same ensemble of QDs; to vary the

studied point on the sample, all the cryogenerator is moved in a plane perpendicular to the collection axis by a massive x-y positional stage.

The main optical axis is defined by the entrance slit of the Streak Camera (subsection 4.1.2), in the case of Time Resolved Photoluminescence (TRPL) experiments. Laying on a rail fixed to the Streak Camera's housing, the collection branch objective A is focused on the sample; lens B focus the light on the slit of the single 0.5 m focal length imaging spectrometer attached to the Streak Camera; this lens is chosen in order to fit the f factor[35] of the spectrometer, avoiding under- and over-illumination of the NIR gratings.

When measuring in Continuous Wave (CW) excitation conditions, light is redirected to a double 0.6 m focal length monochromator through a multimode optical fiber (200 μm core) adapted directly to the rail, and synchronously detected by a silicon avalanche photodiode (Si-APD), a cooled germanium detector using the Lock-in technique or a Si Charged Coupled Device CCD depending on the detectivity and spectral response needs. The light source employed in all macroscopic measurements is a Ti:sapphire laser (subsection 4.1.1); this laser can be used to excite the sample in Continuous Wave (CW) operation, and tune the excitation wavelength from 710 nm to almost 1000 nm. Fixing the excitation wavelength above the bandgap of the QD matrix material (GaAs) we measure the non-resonant photoluminesce (PL); resonant PL is obtained when exciting resonant to the WL or QD transitions.

4.1.1 Ti:Al_2O_3 laser and OPO

Coherent's Mira 900 is a commercial mode-locked Ti:Al_2O_3 laser; built to work in the femtosecond cavity drawn in Figure 4.2; a specially designed optics set (XW) allows pulsing over the 710-970 nm range approximately without changing any optic element in the cavity. A dry atmosphere is needed inside the cavity to work at wavelengths were water absorption is noticeable.

The Ti:saphire crystal is pumped with a doubled Ne-NO_4 laser, Coherent's Verdi, that provides up to 5.5 W of green light with the proper coherence and intensity stability.

The original femtosecond configuration provides pulses with a FWHM of 150 fs at a repetition rate of 76 MHz through passive mode-locking (auto-focusing kerr-effect, special coating chirp of the optical elements and compensation of the group velocity by glass prisms form part of the complex and commercial process employed in this laser), but two extra configurations of the laser have been used in addition.

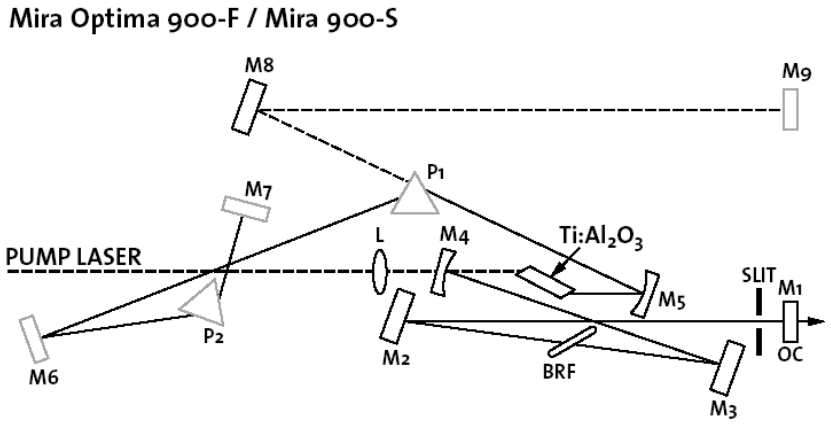

Figure 4.2: **Sketch of the Ti:Al_2O_3 laser Mira 900-f. The drawn cavity corresponds to the femtosecond configuration.**

The picosecond configuration substitutes one of the two branches of the cavity (M5 to M7 part in Fig. 4.1.1) redirecting the beam to an electronic stabilization system, Gires-Tournois Interferometer(GTI), and allows the generation of much broader pulses (with a FWHM around 2 ps) at almost the same repetition rate: the electronic signal of a fast photodiode right before the exit of the laser cavity is used as feedback for the GTI. These broader pulses offer the chance to work with time resolved experiments but with less peak power per pulse (the same average power is redistributed in a 10 times bigger time frame); saving saturation and non-linear effects that are not always desired.

Just by removing P1 from the beam path, M5 to M7 branch is replaced by the branch drawn in dot lines from M5 to M9; The new cavity configuration is called auxiliary cavity and was originally build for alignment purposes. The laser in that configuration can only work in continuous

wave mode, as no pulse compensation system is present at all. Even if it was originally thought just for "aligment" purposes, this cavity is free of the "pulse formation" perturbations that lead to pulsed operation, and as a consequence presents less amplitude noise compared with the other two cavities operated in continuous wave mode.

In the experiments summarized and discussed in chapter 7, an Optical parametric oscillator (OPO) has been used. Synchronously pumped by a Ti:saphire laser, it has a *twin cavity* whose own frequency has to completely match the Ti:saphire own cavity frequency; pulses up to 350 mW optical output power at wavelengths from 1050nm to 1300nm are generated through phase-matching in a KTP crystal. The cavity length is dynamically adapted to compensate the frequency drift of the Ti:saphire due to time and environmental changes, by using a feedback electronics controlling the position of one of the end mirrors, attached to a piezoelectric stage.

4.1.2 Streak camera

The time-resolved measurements discussed in chapter 5 have been performed with a commercial Streak Camera.

The working principle of the streak camera lays on the synchronization and triggering of a sweep voltage to the optical pulses out of our Ti:saphire laser.

Light is dispersed by a 0.5m focal length spectrograph and focused with the proper optics on a S1 cooled photocathode, electrons pulled out are accelerated and deflected by the saw voltage (between plates C on Figure. 4.3) that disperses them vertically before they enter in the Micro-Channel plate: the electron signal is amplified here and finally impacts a phosphor screen, the re-emitted signal is collected by a CCD and the data processed on a personal computer. The optical pulses trigger a saw voltage (an ultrafast photodiode detects every pulse and the positive edge of the generated electrical signal is used to shoot the saw voltage), which increases fast in the ns range, establishing a direct relation between the arrival of an electron and applied voltage: the deflection and, as a consequence, the vertical position of the final signal is time correlated.

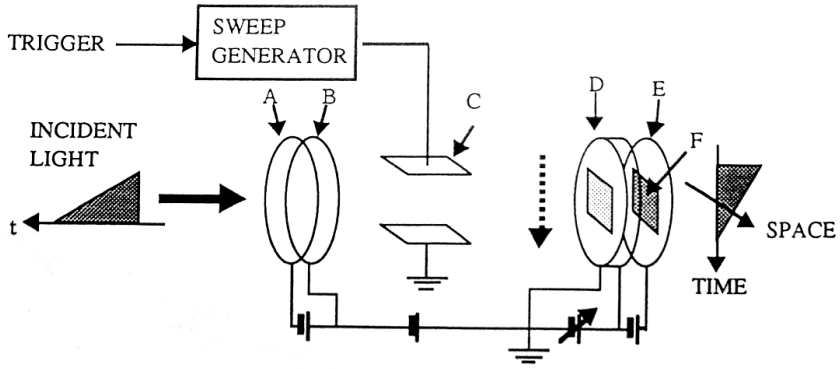

Figure 4.3: **3 Diagram of the main components of the Streak Camera A: Photocathode B: Acceleration mesh C: Sweep electrode. D: Micro channel plate E: Phosphor screen F: Streak Image.**

The overall time resolution in the widest temporal window (2 ns) was around 40 ps for excitation of 2 ps wide pulses at 76 MHz of repetition rate. For this study, the sample was held on the cold finger of a closed-cycle cryostat.

4.2 Microscopic measurements: Confocal microscope

In order to study the emission of an isolated QD, a better spatial resolution is required. The concept of confocal microscopy represented a great advance in optical instrumentation; it can be briefly described as the use of pupils to the spatial filtering of light generated out of the focus and it has been demostrated an essential tool to study single QDs, as illustrated in figure 4.4.

The data presented in chapter 6 was measured using a confocal microscope, Attocube model "attoCFM I" whose optical diagram is shown in figure 4.5. The aspheric lens over the sample, at the bottom of the diagram has a high numeric aperture, to maximize the detection of isotropic emitted photoluminescence.

The microscope was inserted in a He exchange gas chamber of an im-

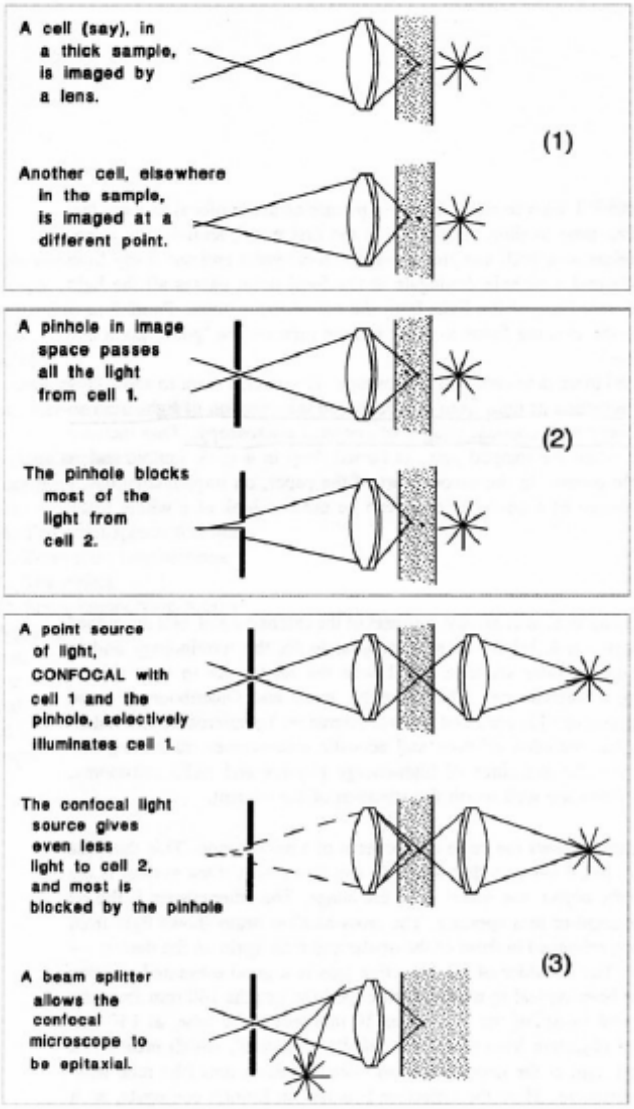

Figure 4.4: **Sketch of basic principles and fundamentals of confocal microscopy**

mersion cryostat to keep temperature on the 4-10 K range. Moderate vacuum in the microscope head prevents water condensation on the samples and piezoelectric motors, while the Helium chamber is isolated of the

environment through a liquid Nitrogen pre-stage.

Two optical fiber connections to the microscope were used for optical excitation and detection light (both monomode fibers adapted to work in the Near Infrared (NIR), 830 nm for excitation and 1060 nm for detection). Both fiber cores (Mode Field Diameter (MFD) in the range of 5 μm) act as pupils of the system (following nomenclature of figure 4.4, on source (excitation) and image (detection) branches), and hence responsible of its confocality.

The sample lays on an inertial piezo stage that allows its positioning with respect to the light spot ($\leq 1\mu m^2$) with a great accurancy (at cryogenic temperatures, the steps can be as small as 10 nm) but still preserving a great movement range, $7x7mm$ en the XY plane and $6mm$ in the focal axis. After the movement induced by a small electric "pulse", the inertial piezos remain at the desired position without any applied voltage, which confers a great stability to the whole system and avoids a source of signal drift; resulting in long time stable measurements.

The free edge of the detection fiber is connected and adapted to a 0.3 m focal length double spectrograph, while light is detected with a Si back-illuminated cooled CCD at the exit of the second spectrograph or by a Si Avalanche PhotoDiode APD detector operating in Geiger mode at the exit of the first one; a fast transition between both detectors is possible without altering the measuring conditions. Laser light coupling to the excitation fiber is carried out by means of a high precision massive holder to avoid, as much as possible, intensity fluctuations. The tunable Ti:sapphire laser of section 4.2 on any of its operative modes (continuous wave or pulsed) and different diode lasers (830 nm CW, 830 nm Pulsed, 780 nm CW..).

The spectral response of the whole system is carefully registered and used to correct the measured data , compensating at the same time the spectral response of the optical fibers, lenses, sources, monochromator and detectors.

4.2.1 Time correlated measurements

Micro time resolved PL (μTRPL) measurements were performed by using a Time Correlated Single Photon Counting (TCSPC) board to ana-

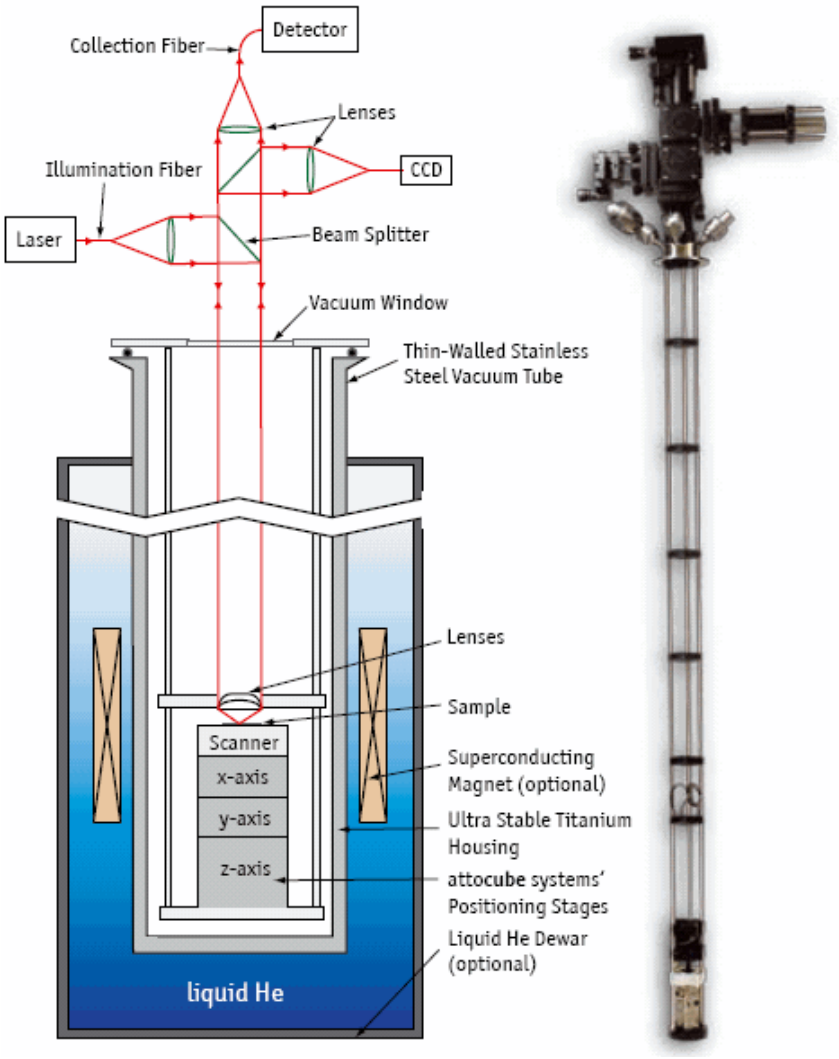

Figure 4.5: **Sketch of a free optics confocal microscope, prepared for immersion in a cryogenic dewar. At the bottom of the microscope the piezoelectric positioning stage is placed.**

lyze the light dispersed by the double spectrograph and detected with a Si Avalanche PhotoDiode APD detector operating in Geiger mode (Perkin Elmer SPCM-AQR-15FC). Time Correlated Single Photon Counting working principle lays on the capacity to detect fast electrical signals in two

channels (start and stop) and calculate the delay between them; the two signals employed in our case are:

1. Reference: The repetition rate of the source, that results to be the the positive slope edge of the electrical signal out of the direct detection of the light out of the laser by an ultrafast photodiode,

2. Signal: the detected photoluminescence signal out of the Si Avalanche PhotoDiode APD detector operated in Geiger mode.

Once a signal arrives to the start channel, the clock starts to count until a signal arrives to the stop channel. The result is *"one count"* in the histogram Counts vs time at the time measured by the clock.

In order to get correct temporal correlation of all photoluminescence events, one has to avoid the over-sampling systematic error: when two photoluminescence photons happen in the same laser pulse period, only one event is temporally correlated. As an example, if the photoluminescence signal was chosen as start, two starts before the arrival of an stop would lead to only one count: the first start would be discarded after the re-start of the clock and not included in the measurement, creating a systematic error in the measurement of "earlier" events. To overcome this problem, the amount of counts per second in the reference channel has to be really bigger than in the signal channel, and actually the rates of counts in both channels differ some orders of magnitude: while the repetition rate of the laser lays around tenths of megahertz (in the Ti:sapphire laser case 7.6 10^7 counts per second while in the 830 nm pulsed diode laser case it can be chosen among 40, 20, 10, 5 and 2.5 per 10^6 counts per second), the detected signal lays in the range of 200-0.2 counts per second: a QD does not absorb/emit a photon during every pulse time frame at the needed excitation intensities and, of course, only a small part of the emitted photons can be finally collected and detected.

If the reference signal is chosen as stop clock, the clock is not started without a contribution to the measurement, saving electronic events and maximizing the performance of the counting board and its temporal response.

The measured μTRPL transients are broadened due to the temporal response of the system; problems in determining precisely the exact shot time, jittering effects in the laser (random fluctuations of the pulse modes

on the cavity) and the temporal FWHM (full width at half maximum) of the detector and the laser pulse (the 830 nm diode laser is some ps broad), mainly. The whole time response of the system is measured for the experimental conditions and taken into account in the data analysis. A typical FWHM of around 400 ps is found, but time constants above 100 ps can be perfectly distinguished when fitting the experimental results to a mono-exponential decay convoluted with the system response.

4.3 Heterodyne pump and probe

Experimental results presented in chapter 7 are the result of a six-month collaboration-stay at the University of Dortmund under the supervision of Pr. Dr. Ulrike Woggon. Measurements where performed in the heterodyne set-up built there (figure 4.8), a flexible technique that facilitates different kinds of experiments (Differential Transmission, Pump-Probe, Four-Wave Mixing (FWM), Temperature and current injection control); we centered our efforts in Pump-Probe measurements on Semiconductor Optical Amplifiers (SOAs).

Pump and Probe experiment is a standard technique in Optical Spectroscopy, the changes induced by the "Pump beam" on the sample under study are checked through the variation on the transmission of the "Probe beam". The Probe beam power has to be kept well below that of the pump. The perturbation induced on the medium by the Probe beam has to be negligible compared with the changes induced by the Pump beam.

If Pump and Probe beams are pulsed, time response of the media can be measured statically through the delay between both pulses (τ_d). The lowest power pulse "probes" the changes in the medium after τ_d time the arrival of the Pump pulse. Changing the delay (usually through a precise delay line) the time resolved pump-probe curve can be registered. The time resolution of this kind of experiments is limited by the temporal FWHM of the pulses.

Figure 4.6 shows the normal scheme used in time resolved Pump-Probe measurements, where both beams are spatially resolved, the usual way to distinguish between both beams. It also allows to measure the FWHM, related with the polarization response of the sample (on $2k_2 - k_1$ direction

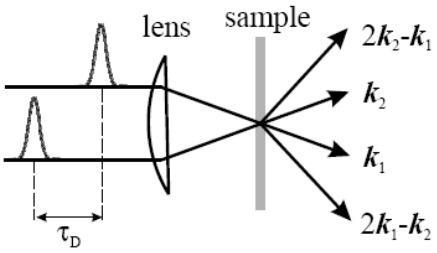

Figure 4.6: **Scheme of a pump-probe experiment with the pump pulse propagating along k_1 and the probe pulse along k_2. The FWM signal is usually detected in the direction $2k_2 - k_1$**

in figure 4.6).

That standard scheme fits for thin samples: the volume of the measurement is limited to the overlap of the two beams, but does not work for extended volumes and usually results in small signals difficult to detect. If one is interested on measuring bigger volumes or time resolve processes on waveguides, a different way of distinguishing beams has to be used. Alternatives include color or polarization selection. The heterodyne pump-probe solution consists in *"marking"* both beams by up-shifting them in frequency, afterwards beams are combined with a reference beam in the *"balance detection scheme"* in order to isolate the beat of the selected beam and obtain a measurement proportional to its electric field intensity. Degenerate (with the same "color" or wavelength) co-propagating beams are used to test waveguide devices while offering the chance to control the polarization evolution and providing not just information of the electric field evolution but also information about the dephasing beams experiment in the sample. Further details are provided in the following paragraphs. A detailed experimental description can be found in the pioneer work of Hall [36, 37] and a detailed theoretical analysis in reference [38].

An Acusto Optic Modulator (AOM) is a glass-made device that deflect part of the beam that crosses them when feeded by the proper electrical wave; the acoustic wave generated through that electrical wave creates a kind of grating that upshifts in the order of radio frequencies range the frequency of the deflected beam part. The upshifted frequencies are

carefully chosen in order to provide a difference between the repetition rate of the Ti:zaphire laser (75.4 MHz) and the AOM upshift frequency (for AOM1:ν_1=77MHz and for AOM2: ν_2=80 MHz) in the MHz range, that is the working frequency limit of the lock-in device that will isolate the ultimate measured beat.

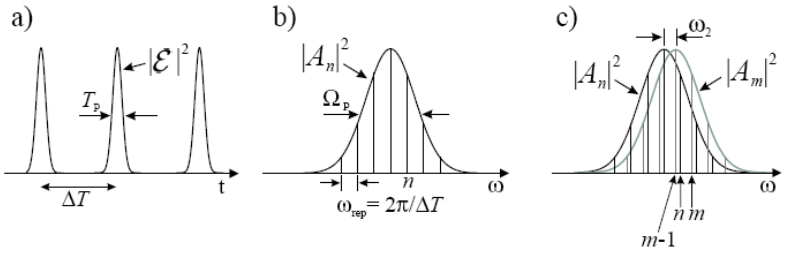

Figure 4.7: **a) Pulse train in time domain, T_P: pulse width, $|\varepsilon|^2$: envelope function in time and ΔT: distance of the pulses in time. b) Spectrum of a single pulse with the modes of the pulse train, Ω_P: spectral width and ω_{rep}: repetition frequency. c) Shift of the spectrum by ω_2.**

Figure 4.7 shows the effects on the temporal and spectral domains that the upshift process has on the deflected beams. A simple conceptual reduction of the whole process would lead to think about the heterodyne technic like a modification of the standard lock-in technic: instead of modulating the amplitude of the signal to distinguish it from the background, here we modulate the frequency.

The part of the heterodyne set-up used in Pump-Probe measurements is shown in figure 4.8.

Light out of the OPO crosses a two-Michelson interferometer, the controlled reflections provide an easy way to generate a small pulse train up to four pulses, with controllable delays between the pulses. If one mirror is blocked, the pulse train is reduced to two pulses, if another mirror (at the other beam splitter) is blocked, we recover the typical one pulse experiment. Excitation beam is divided at C_1 beamsplitter, redirecting 60% of it's energy to the Pump branch (Pump beam > Probe Beam); AOM deflected part of the beams in both branches, the *frequency modulated*

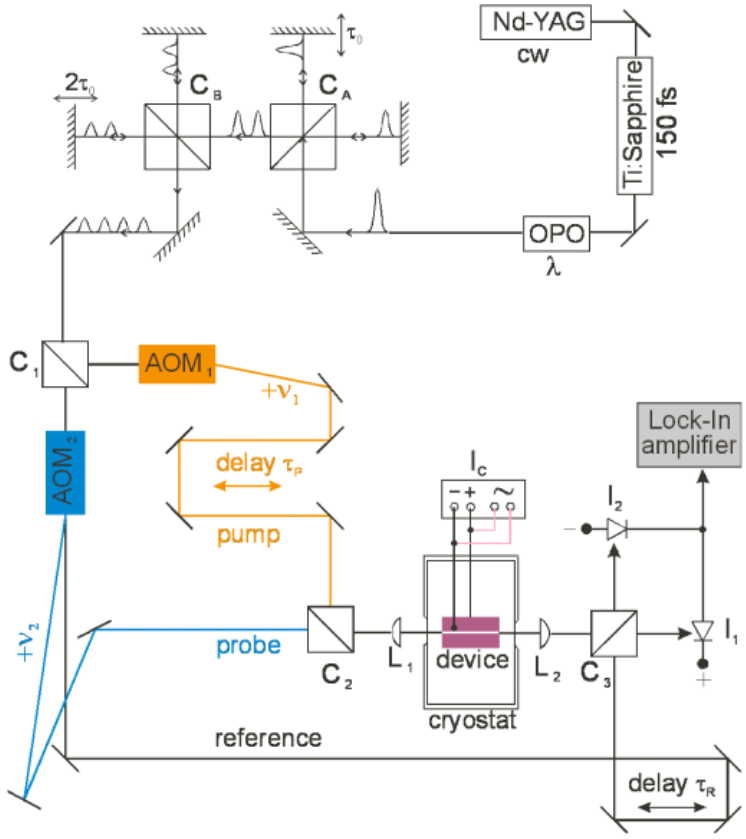

Figure 4.8: **Sketch of the Heterodyne setup used for Pump and Probe measurements**

beams are redirected to C_2 beam-splitter, a delay line is introduced in the pump beam path in order to control the delay between Pump and Probe pulses through a change on the total traveled distance. Optical elements are carefully aligned to assure that both beams propagate collinear out of the C_2 beam-splitter. The resulting overlapped beam is introduced in the waveguide of the device under study through a high numeric aperture lens L_1 laying on high precision positioning stage adjusted through an electrical controller. The device is placed in a Helium flow cryostat and carefully connected to a current source in order to control both temperature and

current in it. The transparent widows of the cryostat are specially designed to allow a reduced working distance between L_1 and the device waveguide entrance. The same procedure is followed at the exit of the device, L_2 also lays on a precise positioning stage and is carefully aligned to get all the light out of the waveguided device. The reference beam is the non-deflected beam out of AOM_2, another delay line is placed on the reference beam optical path; it provides a useful tool to perform *in-situ* cross-correlations between the reference beam and the Pump or Probe beams; optical path length has to be equal for reference beam and the detected beam, in order to interfere correctly on the detectors, so the careful calibration of the reference beam optical path is essential.

4.3.1 Balance detection

Figure 4.9 offers a detailed scheme of the balance detection system used to measure the amplitude of the Probe(Pump) beam.

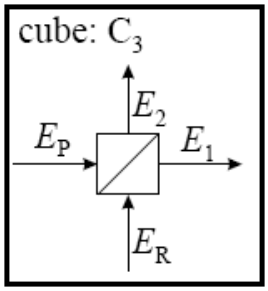

Figure 4.9: **Cube 3 detailed beam nomenclature.** E_P **stands for the pump-probe beam,** E_R **is the reference beam and** E_1 **and** E_2 **are the resulting beams detected by detectors 1 and 2**

As is shown in figure 4.7, the pulse out of the OPO is composed by the sum of longitudinal modes equi-spaced ω_{rep}(75.4 MHz) in the spectral domain but modulate by an envelope function centered at the emission frequency ω_0; the frequency upshift induced by the AOM modulator reflexes as a sum term ω_2 over the central frequency of the envelope function ω_0. In the following mathematical development we consider just the Probe beam electric field (E_P) and reference beam electric field (E_R) as Pump

beam follows the same reasoning:

$$E_P(t) = e^{-i(\omega_0+\omega_2)t}\sum_n A_n^P e^{-in\omega_{rep}t} + c.c. \quad (4.1)$$

$$E_R(t) = e^{-i\omega_0 t}\sum_n A_n^R e^{-in\omega_{rep}t-\tau_R} + c.c. \quad (4.2)$$

Where τ_R is the delay time existent between the Probe beam and the reference beam. C_3 is a 50:50 beam splitter, so the resulting electric field E_1 and E_2 can be expressed like:

$$E_1(t) = \frac{E_P + E_R}{\sqrt{2}} \quad (4.3)$$

$$E_2(t) = \frac{E_R - E_P}{\sqrt{2}} \quad (4.4)$$

The signal that arrives to the lock-in detector is the substraction of I_1 and I_2, integrated during the detector response time T_{det},

$$I_1 - I_2 \propto \int_{T_{det}} (E_1^2 - E_2^2)dt \propto \int_{T_{det}} (E_R E_P)dt = \quad (4.5)$$

$$\int_{T_{det}} dt[e^{-i(2\omega_0+\omega_2)t+i\omega_0\tau_R}\sum_{n,m} A_n^P A_m^R e^{-i(n+m)\omega_{rep}t+im\omega_{rep}\tau_R}$$

$$+e^{-i\omega_2 t-\omega_0\tau_R}\sum_{n,m} A_n^P A_m^{*R} e^{-i(n-m)\omega_{rep}t-im\omega_{rep}\tau_R} + c.c.]$$

Rapidly oscillating terms (for $1.3\mu m$, ω_0 corresponds to 240 THz) vanish when integrated over T_{det} ($T_{det} << \frac{2\pi}{\omega_0}$) and cannot be detected by the our detectors, but radio frequency variations can still be appreciated. The lock-in device can't be block to ω_2 or ω_{rep} frequencies, but some of the beats that compose equation 4.6 lay on the few MHz range, were they can be locked; for example, $m = n + 1$ gives a directly detectable term (as it's slowly varying compared with T_{det}):

$$I_1(t) - I_2(t) \propto e^{-i(2\omega_2-\omega_{rep})t}(e^{-i(\omega_0-\omega_{rep})\tau_R}\sum_n A_n^P A_{n+1}^{*R} e^{-in\omega_{rep}\tau_R}) + c.c \quad (4.6)$$

The bracket enclosed term can be easily approximate by the cross correlation between Pump and Reference pulses, while the exponential in front is a beat that can be easily obtained as an electrical signal (just combining AOM_2 reference signal and the electrical signal of a ultrafast diode detecting the input laser) and feeded to the lock-in for blocking purposes.

Chapter 5

Steady and time resolved optical measurements in different shapes quantum dot ensembles

Macroscopic measurements of QDs are usually the first step in the optical characterization of any sample; the photoluminescence of an ensemble reflects the properties of isolate QDs, but as it has been introduced in section 3.1.3, the inhomogenous broadening, due to the gaussian size distribution of the self assembled QDs, masks most of the intrinsic properties.

5.1 Different Shape Samples

Typical InAs/GaAs self-assembled QD emission takes place around 1.12 μm at room temperature. Therefore, the extension of their application range to the spectral windows of interest around 1.5 μm, the most common strategies are based in the use of the InGaAs[39] or GaAsSb[40] alloys, for either the dot or the dot capping layers. Similar efforts have been devoted to extend the emission towards shorter wavelengths and, some years ago, "quantum ring" (QR) structures were obtained emitting at 0.98 μm at room temperature[41].

These ring-shaped nanostructures were obtained by an in-situ technique based on the overgrowth of big self-assembled QDs under suitable growth conditions[42]. Now, this growth technique is better understood and different shape nanostructures can be obtained with different vertical and lateral confinement potentials. On the one hand, the strong vertical confinement determines the blue-shift of the ground state emission compared with standard InAs/GaAs QDs. On the other hand, the lateral potential is the main responsible for the energy separation between ground and excited states[43], and plays an important role in the room temperature performance of optoelectronic devices based on these nanostructures. In this work, we will study some basic optical properties of such a kind of different shape QDs, mainly those related to their electronic structure and exciton recombination dynamics at low and high temperatures.

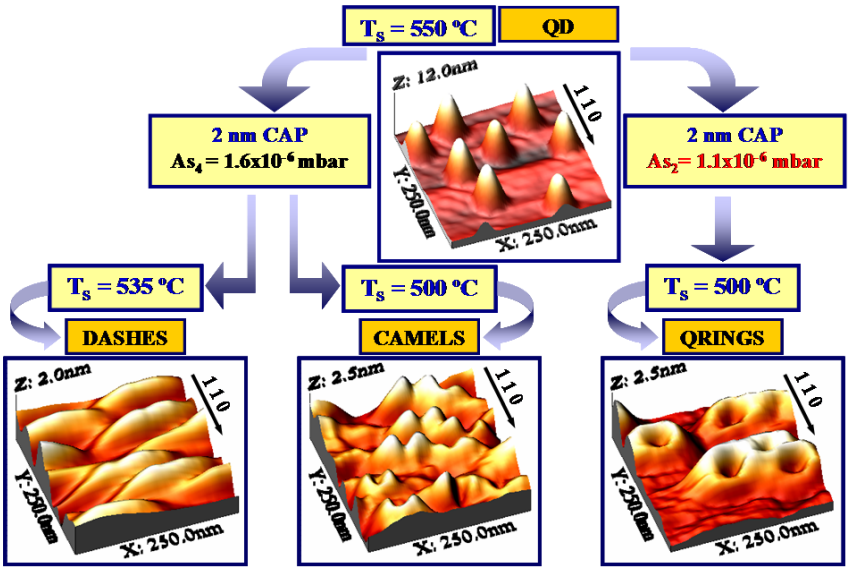

Figure 5.1: **Growth sketch of QDh, QC and QR. Original uncapped QDs on top. The different overgrowth processes are symbolized by arrows leading to the three different kinds of shapes**

The three samples studied in this work follow a similar growth procedure. An initial QD seeding layer is grown by depositing 1.7 monolayers (ML) of InAs onto a (001)-GaAs substrate (after a GaAs buffer layer) at

540 °C, under an As_2 beam equivalent pressure of 3–4 10^{-6} mbar. The InAs deposition takes place in a growth sequence of 0.1 ML InAs (at 0.06 ML/s) plus a 2 s pause under As flux. At the end of this sequence, the QDs are annealed 1 min to enhance the size distribution and to obtain medium density ensembles (10^9–10^{10}cm^{-2}). Subsequently, a thin GaAs cap layer is grown (at a rate of 1 ML/s) at different atmospheres and substrate temperatures, T_{CAP}. In this way, QR are obtained under As_2 atmosphere at 1.1 10^{-6} mbar and $T_{CAP} = 500\,°C$, whereas other two different shape nanostructures are obtained by using As_4 atmosphere, namely "quantum dashes" (QDh) at 1.6 10^{-6} mbar and $T_{CAP} = 540\,°C$, and "quantum camel-humps" (QC) are obtained at $T_{CAP} = 500\,°C$. The samples for Atomic Force Microscopy (AFM) characterization were cooled down immediately and removed from the growth chamber, while the samples for optical measurements were capped with a 50-nm-thick GaAs layer under a higher substrate temperature, 595 °C. More details of the sample growth and AFM characterization can be found on ref [42].

The nanostructure morphology was investigated by contact mode AFM (shown in Fig. 5.1). The uncapped nanostructures called here QDh are elongated islands with typical length-width product around 160x40 nm^2, QC have the aspect of two camel-hump-like islands (around 100x50 nm^2 each "hump") and QR are similar to previous reported ring islands (100x90 nm^2)[41]. These nanostructures are characterized by smaller heights than their pyramidal InAs/GaAs counterparts. Uncapped quantum rings show typical heights around 1.5 nm, while QCs and QDh are slightly higher (2 nm).

It should be noted that the absolute dimensions given here are derived from the analysis of uncapped nanostructures. As found recently in cross-section high resolution transmission electron and scanning tunneling microscopy characterization of capped QRs, the uncapped values only remain approximately valid[44, 45]. In addition, these studies also reveal a complicated composition profile resulting from the In/Ga exchange process taking place during the overgrowth step.

5.2 Low temperature PL and PLE: Origin of the emission

Figure 5.2 shows the PL spectra measured at low temperatures and using above barrier (GaAs) and low density excitation conditions. The ground state transitions are centered at 1.25, 1.34 and 1.35 eV for QDh, QC and QR nanostructures, respectively. As stated above, the ground optical transition energies for these kind of small nanostructures should mainly respond to the strong spatial confinement along the growth direction: QDh and QC are only 2nm high, 3 to 5 times smaller than usual QD structures, and their ground states thus lie at higher energies than those, as expected. Nevertheless, despite their similar height, the QDh and QC emission bands are separated by an average energy difference of 90 meV, while the difference is negligible between QCs and QRs, whose heights estimated by AFM differ by roughly 2 MLs. This contradictory result clearly show that the particular In/Ga-alloying process leading to the formation of different shape nanostructures also leads to different composition profiles. This fact masks the simple and intuitive correlation between nanostructure size and confinement energy and makes difficult to compare our results with the electronic structure calculations reported for standard QDs in the literature.

The PL spectra shown in Fig. 5.2 exhibit important size dispersion for the three samples, as revealed by the large full width at half maximum (FWHM): 60, 45 and 80 meV for QDh, QC and QR samples, respectively. The PL bands are approximately single Gaussians in the two latter cases, whereas three components can be nicely resolved for the sample containing QDh nanostructures as depicted by the three-Gaussian fit in Fig. 5.2(a). These three Gaussian components are peaked at 1.222, 1.250 and 1.274 eV and have linewidths below 30 meV. Given the low excitation conditions used here, a multi-modal behavior is assumed leading to three different QDh sub-ensembles whose average height would differ in 1 ML (two of the QDh families giving rise to two consecutive PL components split by 25 meV). With the given caution, such assignment is compatible with estimates for small lens shaped QD[46], whose vertical dimensions are comparable to our nanostructures.

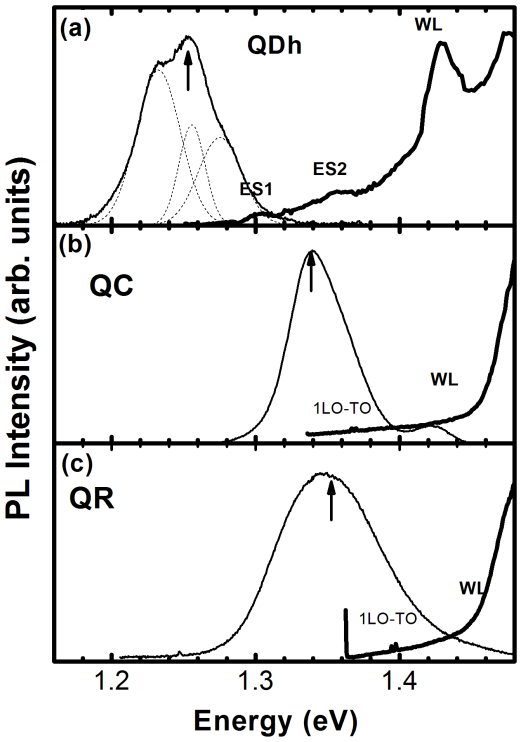

Figure 5.2: **PL (thin line) and PLE (thick line) spectra of (a) QDh, (b) QC and (c) QR ensembles. The arrows indicate the PLE detection energy. The first and second exited state (ES1 and ES2, respectively) and wetting layer (WL) resonances are indicated when observed.**

Figure 5.2 also shows the PLE spectra recorded for each sample. The PLE spectrum for the QDh sample reveals two resonances at around 55 meV and 110 meV above the detection energy, 1.250 eV. They must be related to the absorption at the p- and d-like excited state shells of the QDh family represented by that detection energy. When the PLE signal is detected on the low or high energy parts of the PL spectrum (namely, QDh families at 1.222 or 1.274 eV, respectively) we find similar values,

consistent with an smooth change of the carrier confinement energy with the average QDh dimensions. We cannot observe any resolved contribution from excited state absorption in the PLE spectra of QC and QR ensembles, as observed in Figs. 5.2 (b) and (c).

The contribution of the states at the continuum can be also investigated in the three samples. The WL related emission cannot be detected in the PL spectrum of the QDh sample [Fig. 5.2(a)]. However, a well-resolved absorption line at 1.425 eV is associated to the WL exciton absorption peak in the corresponding PLE spectrum. On the contrary, the WL layer emission is observed clearly at around 1.44-1.45 eV for the QC ensemble, and also recognized in the high energy tail for the QR ensemble, but its corresponding absorption cannot be distinguished from the GaAs absorption edge in their PLE spectra [Figs. 5.2(b) and (c)]. The outlined differences could indicate that the WL states are strongly (fast trapping times) correlated to the QDh carrier states thus producing strong PLE signal at the WL energy. Apparently, the relaxation is less efficient in the other two samples and the WL emission peak can be observed due to the dwelling time of the exciton in the continuum states. Another possibility is the swearing of the absorption edge at the WL due to the observed extremely large QD size inhomogeneities.

More information can be obtained following the PL excitation density dependence for each sample. State filling of the p- and d-like excited state transitions can be observed for the QDh ensembles by increasing the pumping power, as observed in Fig.5.3(a). We can identify contributions to the PL at around the aforementioned 55 and 110 meV above the ground state (the ground state emission and p-d excited states of the three QDh families are needed to obtain a reasonable multi-Gaussian fit to the experimental results). In the QC ensemble PL we find p- and d-like excited state recombination at around 35 and 68 meV above its ground state emission energy. This time only one Gaussian band for every state is needed as shown in Fig. 5.3(b). Finally, we could not find any evidence of excited state recombination in the investigated QR sample, as shown in Fig. 5.3(c). A value around 40 meV for the energy splitting of the s-s and p-p exciton transitions has been found in similar samples with better size homogeneity, as reported in the literature[43, 47, 48, 49, 50]. This small value, as compared

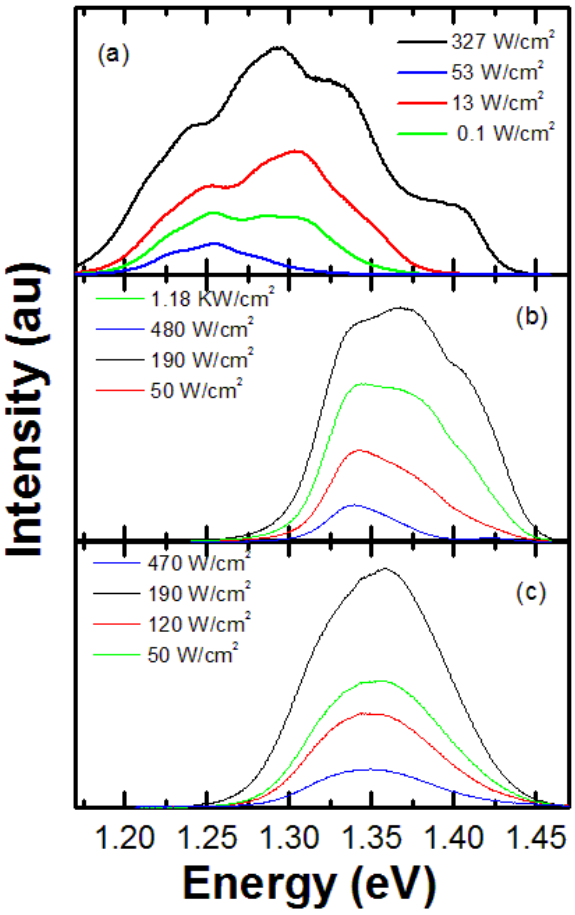

Figure 5.3: **PL at different excitation densities, as indicated inside each plot, for the different ensembles: (a) QDh, (b) QC and (c) QR.**

to the broad PL band representative of our QR ensemble (approximately 80 meV throughout the sample surface), makes the p-like emission unresolved on the high energy side of the measured PL spectra under high excitation density conditions. We finally should note that the splitting just

found among the ground and excited shells are considerably smaller than the corresponding energies found in pyramidal InAs dots (70-100 meV). Again, with the caution given, this fact must be related with the larger lateral dimensions of our nanostructures in comparison to the latter.

5.3 Exciton radiative recombination at low temperatures

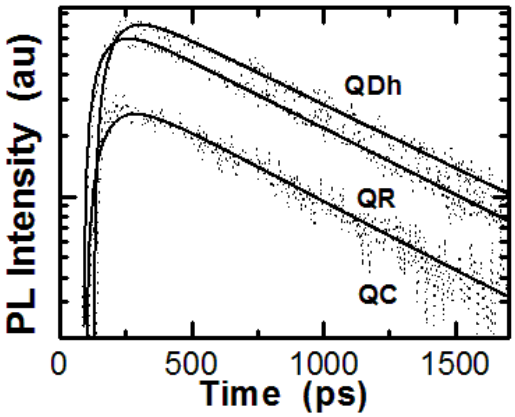

Figure 5.4: **PL transients measured at 10 K at the PL peak energy in the three samples under low excitation density conditions. The excitation wavelength was 765 nm.**

Figure 5.4 shows typical PL transients at 10 K for the three samples at the average PL peak energies. A fast rise time of the order of the experimental resolution is measured for the three types of ensembles and hence no phonon bottleneck is observed. The decay transient curves do not exhibit saturation effects at the relatively low powers used here. Nevertheless, we must note that we have not found significant changes of the PL decay time by increasing the excitation density by more than three orders of magnitude (after appropriate modeling of the saturation effects due to excited state filling).

Figure 5.5 summarizes the decay times measured under the same con-

ditions as a function of the emission energy for the three samples. The PL decay time at the PL peak energy is typically larger for QDh nanostructures (850-950 ps) than for QC (750-800 ps) and QR (750-820 ps). The measured decay times are not very far from values found in literature for pyramidal InAs dots [51, 52], for which a certain dispersion of absolute values (within the range 1 - 2 ns) are found. Such a significant dispersion is usually attributed to different pyramidal truncation degrees, which could give rise to different oscillator strength of the ground state exciton optical transition[53].

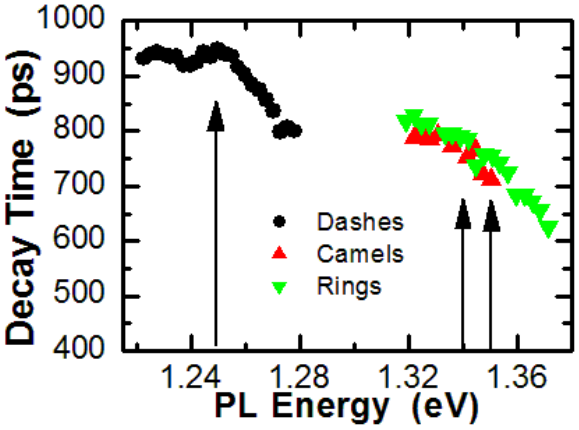

Figure 5.5: **PL decay time as a function of the detection energy under very low excitation densities for the different nanostructures.**

If we only consider radiative mechanisms, due to the enhanced overlap among the electron and the hole wavefunctions, a shorter decay lifetime is expected for smaller QDs. As observed in Fig. 5.5, our TRPL results exhibit such behavior and quantum confinement energy and decay lifetime are inversely correlated in the different samples. Also, for each sample, the decay time does not remain constant over the whole emission band: decreases on the high energy side of the PL bands, mainly above the average PL peak energies, as observed in Fig. 5.5. Such a similar effect has been reported in pyramidal QD ensembles, and it must be attributed here to the increase of confinement by reducing the size volume of the nanostructure[54] and the participation of excited states of the biggest

dots of the distribution.

5.4 Radiative and Non-radiative exciton dynamics

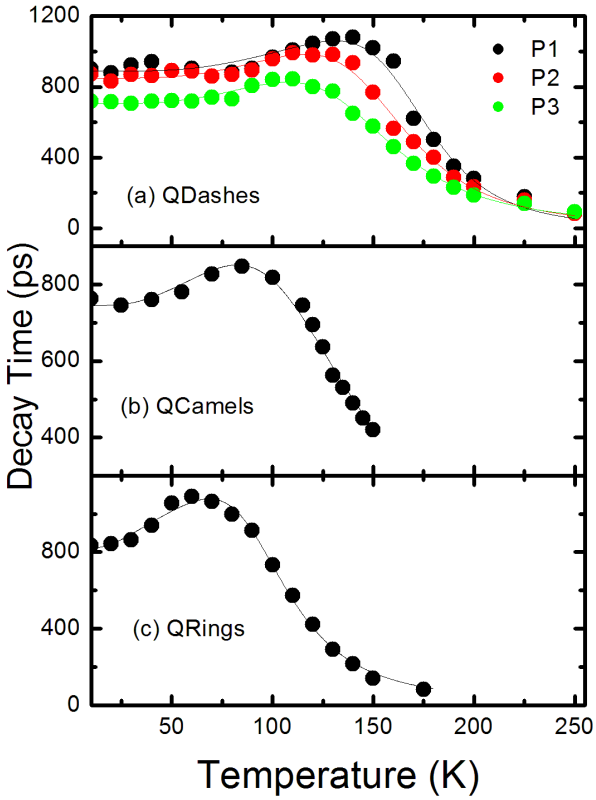

Figure 5.6: **PL decay time for QDh (a), QC (b) and QR (c). The evolution for the three QDh families resolved at 1.225 (black), 1.250 (red) and 1.274 eV (green) at low temperature are represented in (a).Continuous lines stand for the best fit to the experimental data obtained using Eqs. 6.**

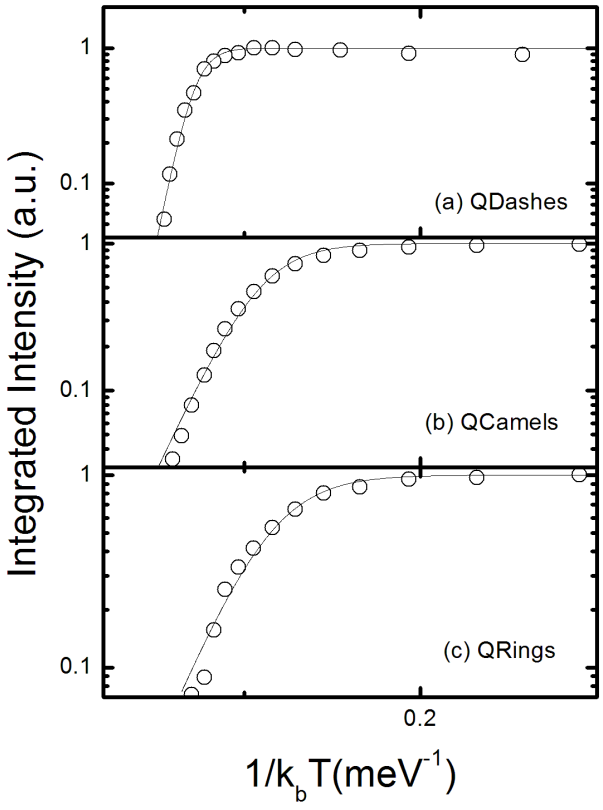

Figure 5.7: **Arrenhius plot of the integrated PL intensity of the whole band for QDh (a), QC (b) and QR (c).Continuous lines stand for the best fit to the experimental data obtained using Eqs. 12 (left panel).**

The temperature evolution of the integrated PL intensity and the ground state exciton lifetime (detection at the PL peak energy) are plotted in Figs. 5.6 and 5.7. As observed, all samples are characterized by a similar behavior and two temperature regions can be defined in view of our results. In the first regime, the exciton recombination time increases with increasing temperature while the integrated intensity remains essentially constant. At a given temperature, the decay lifetime reaches its maximum and the

second regime begins. Here, the exciton lifetime decreases monotonically with temperature while the PL band becomes quenched. Above a given temperature, that depends on the carrier confinement energy, a thermally activated carrier escape towards the continuum states is the main mechanism producing the observed PL intensity reduction[55, 56, 57, 58]. Our nanostructures are capped only by GaAs barriers, thus the carrier escape towards the wetting layer states opens the non radiative recombination channels at high temperatures: the corresponding non radiative recombination times should be comparable if not faster than the recapture time in the nanostructures[59].

The behavior at low temperatures deserves more attention. Its origin is attributed here to the thermal population of the first non-radiative excited state (electron in a s-like state and hole in a p-like state), competing with the exciton radiative recombination at the ground state (electrons and holes at s-like states)[58]. Emission and retrapping involving WL states[56] is disregarded since we observe the same behavior over the entire PL band (different dot sizes) and no carrier redistribution in the ensemble is observed.

The participation of s_e-p_h dark states in the thermalization process of the photogenerated excitons can be described as a two particle (uncorrelated) phenomenon. However, the capture and thermal escape of carriers does not take place independently for electrons and holes (unipolar escape), but involve Coulomb correlated electron-hole particles[60]. That is, a QD state occupied by an electron (hole) increases its probability to capture a hole (electron). Therefore, in order to model the temperature evolution by taking into account dark state thermalization, we develop a single particle (exciton) model similar to the one in ref [61] instead of a two particle model[27, 62]. In the first case we will obtain an analytical expression, whereas the second leads to a system of coupled differential equations without analytical solution.

The energy level scheme representative of our model is depicted in fig. 5.8. The populations at ground, dark and WL (exciton) states are given by n_1, n_2, n_{WL}, respectively. The decay times for excitons at WL and ground states are labeled as τ_{dWL} and τ_r, respectively. The relaxation time from dark to ground state is τ_{2-1} and the exciton capture at n_1 and

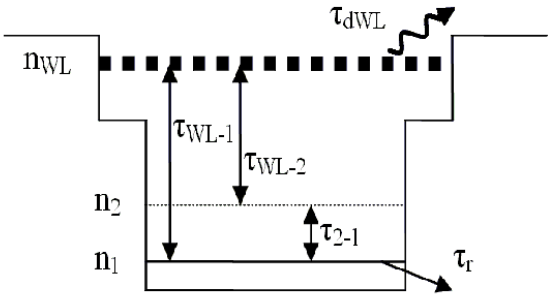

Figure 5.8: **Level distribution scheme in a simplified QD model.**

n_2 QD-levels from the WL states is represented by τ_{WL-1} and τ_{WL-2} times. The times for the opposite processes (up arrows in Fig.5.8 indicating the particle transfer from low to high energy levels) can be found by assuming the system reaches a quasi-Fermi equilibrium without external excitations[16, 31], as referred in section 3.3.4:

$$\tau_{e2-1} = \frac{1}{g}\tau_{2-1}e^{\frac{\Delta E_{2-1}}{kT}} \quad (5.1)$$

$$\tau_{eWL-i} = \frac{1}{g'}\tau_{WL-i}e^{\frac{\Delta E_{WL-i}}{kT}} \quad (5.2)$$

where ΔE_{2-1}=E_2-E_1 is the energy difference between dark and ground states and E_{WL-i}=E_{WL}-E_i the energy difference between the WL and the particular lower energy i-state (i = 1,2). The g-factor accounts for the relative degeneracy between ground and dark states. The validity of the equations 5.1 was also discussed in Ref.[60] and attributed to the participation of phonon emission and absorption in the capture and escape processes, respectively. In a first approximation both kind of assumptions should depend on the degeneracy of the initial and final states involved in the relaxation process.

The exciton recombination dynamics (neglecting carrier recapture in the nanostructures) in our nanostructures would be described by the following

rate equation system:

$$\begin{aligned}\frac{dn_1}{dt} &= -\frac{n_1}{\tau_r} - \frac{n_1}{\tau_{WL-1}}e^{-\frac{\Delta E_{WL-1}}{kT}} - \frac{n_1}{\tau_{2-1}}e^{-\frac{\Delta E_{2-1}}{kT}} \\ &+\frac{n_2}{\tau_{2-1}} + \frac{n_{WL}}{\tau_{WL-1}}, \end{aligned} \tag{5.3}$$

$$\begin{aligned}\frac{dn_2}{dt} &= \frac{n_1}{\tau_{2-1}}e^{-\frac{\Delta E_{2-1}}{kT}} - \frac{n_2}{\tau_{2-1}} - \frac{n_2}{\tau_{WL-2}}e^{-\frac{\Delta E_{WL-2}}{kT}} \\ &+\frac{n_{WL}}{\tau_{WL-2}}, \end{aligned} \tag{5.4}$$

$$\frac{dn_{WL}}{dt} = G - \frac{n_{WL}}{\tau_{WL-1}} - \frac{n_{WL}}{\tau_{WL-2}} - \frac{n_{WL}}{\tau_{dWL}(T)}. \tag{5.5}$$

First of all we can calculate the integrated PL intensity evolution. Under steady state conditions thermal equilibrium is achieved and the PL intensity due to exciton recombination at the ground state can be obtained. Assuming $\tau_r >> \tau_{2-1}$ and neglecting high order exponential terms we arrive to:

$$\begin{aligned} I_{PL}(T) &= \frac{G \cdot p_{cQD}}{p_{cQD} + p_{eWL}(T)} \\ \left(1 + \tau_r \left(\frac{1}{\tau_{WL-1}} + \frac{g}{\tau_{WL-2}}\right) e^{\frac{\Delta E_{WL-1}}{kT}}\right)^{-1} &= \\ &\frac{I_{PL}(0)}{1 + B_{WL} e^{\frac{\Delta E_{WL-1}}{kT}}} \end{aligned} \tag{5.6}$$

where $p_{cQD} = \frac{1}{\tau_{WL-1}} + \frac{1}{\tau_{WL-2}}$ and $p_{eWL} = \frac{1}{\tau_{dWL}(T)}$ are the QD capture rate from WL, and WL recombination rate (radiative and non radiative), respectively, and B_{WL} is proportional to the effective loss rate (inverse of the nonradiative recombination time) in the the WL.

By fitting the experimental data shown in Figs. 5.7 (a)-(c) to equation 5.6, we obtain the corresponding activation energies, E_{WL-1}, and B_{WL} parameter, for each sample. In our samples, the exciton ground state lies not far from the WL states. Particularly, we measure a value E_{WL-1} around 150-175-200 meV for the three QDh families, and around 100 meV for QC-QR nanostructures (Fig. 5.2). At the same time, the WL states are also close to the bulk GaAs bandgap, around 90 meV in all samples.

Therefore, the PL quenching with increasing temperature is due to the thermal activation of excitons from confined states at the nanostuctures towards WL states, from where they are transferred with a faster thermal rate towards the GaAs barriers. Once there the carriers will recombine non radiatively and hence recapture by WL and nanostructures is negligible, as assumed above. Due to the approximations made, above the PL intensity evolution represented by equation 5.6 was independent of the dark state energy and the relaxation time (τ_{2-1}). However, the decay time evolution will be more sensible to the dark state contribution, as discussed below. Firstly, we will assume a short excitation pulse writing for the gain function G=δ(t-t$_0$). In this way, we can integrate Eq. 5.5 alone to obtain:

$$n_{WL}(t) = C \cdot e^{-(p_{cQD}+p_{eWL}(T))t} \tag{5.7}$$

and showing that the WL population will vanish rapidly after pulsed excitation. At low temperatures, the exciton capture at nanostructures will produce a fast depletion of WL states. At high temperatures, their depletion will be produced by non radiative loses at the GaAs barrier, as discussed above. Therefore, at long times after pulsed excitation (t$\sim \tau_d$, where τ_d is the effective exciton recombination time), we can eliminate the WL contribution reducing the differential equation system only for ground and dark state populations, which can be solved by using initial conditions:

$$n_2(0,T) = 0; \tag{5.8}$$

$$n_1(0,T) = e^{\frac{p_{cQD}}{(p_{cQD}+p_{eWL}(T))}} \tag{5.9}$$

This it is not a strictly valid assumption, as the carriers should populate both ground and dark states right after pulsed excitation. However, as far as we are interested in the exciton population dynamics at long times after laser pulse(t>>t$_{2-1}$), if τ_{2-1} is short enough, we know that this system will arrive rapidly to equilibrium by thermalization of the n$_1$ and n$_2$ populations at a given temperature. The time evolution of the ground state population is thus given by:

$$n_1(t >> \tau_{2-1}, T) = C \cdot e^{-\frac{t}{\tau_d(T)}} \tag{5.10}$$

where τ_d is obtained from the relevant constants entering in the exciton recombination dynamics:

$$\tau_d(T) = \frac{p_{cQD}}{p_{cQD} + p_{eWL}(T)}$$

$$\frac{\tau_r \left(1 + g \cdot e^{-\frac{\Delta E_{2-1}}{kT}}\right)}{1 + \tau_r \left(\frac{1}{\tau_{WL-1}} + \frac{g}{\tau_{WL-2}}\right) e^{\frac{\Delta E_{WL-2}}{kT}}} =$$

$$\frac{I_{PL}(T)}{g} \tau_r \left(1 + g \cdot e^{-\frac{\Delta E_{2-1}}{kT}}\right) \tag{5.11}$$

and we have used $\tau_r >> \tau_{2-1}$ and $e^{-\frac{\Delta E_{2-1}}{kT}} >> e^{-\frac{\Delta E_{WL-1}}{kT}}$ in the studied temperature range.

The time decay constant given by Eq. 5.11 does not depend on τ_{2-1}, but it does strongly on the energy difference between the dark and ground states, E_{2-1}. Now, we can use Eq. 5.11 to fit the temperature evolution of the experimental PL decay time, as shown by continuous lines in Figs. 5.6 (a)-(c).

As we can see, the parameter B_{WL} in Eq. 5.6 can be determined by either the PL intensity quenching or the time decay decrease, at high temperatures(represented by Eq. 5.11). One could use the values of B_{WL} obtained from the steady state evolution shown in Figs. 5.7 (a)-(c) to fit the whole temperature behavior of t_d. However, TRPL and PL experiments have inherent different excitation conditions making B_{WL} to be different in both cases, as was discussed in ref [60]. In our case, we also obtain different values for this constant in the fits of both PL and TRPL data to Eq. 5.6 and 5.11, respectively. It is also worth noting that small changes in the fitting parameters E_{WL-1} and E_{2-1} (within the error estimate) produce important changes in the value of B_{WL}. To reduce the degrees of freedom, we have fixed the parameter E_{WL-1} to be the same in both fitting sessions. The degeneracy relative factor g of the s_e - p_h dark exciton transition is also fixed as 2[58]. Therefore, we only use as free fitting parameters E_{2-1} and B_{WL}, the first is determining the increase of t_d with temperature and the second is determining the decrease of t_d at high temperatures, thus establishing the temperature at which takes place the maximum value of t_d in each sample (see Fig. 5.6).

Following this procedure we obtain for the QDh ensemble band: $E_{2-1} = 24.6 \pm 1.2$ meV for the lowest energy family, $E_{2-1} = 23.2 \pm 1.0$ meV for the middle energy family and $E_{2-1} = 20.7 \pm 1.0$ meV for the highest energy family. These energies are less than half the energy splitting between the p_e-p_h and s_e-s_h optical transitions found to be 55 meV in the previous sections. Within our model, they would correspond to the energy separation among s_h and p_h states with respect to the ground exciton. For the other two samples, QC and QR, we find $E_{2-1} = 16.9 \pm 0.7$ meV and $E_{2-1} = 10.0 \pm 0.8$ meV (or 12.2 ± 0.96 and 6.2 ± 1.4 meV, if g= 1, which could be more appropriate if we think that circular symmetry is broken for lateral confinement in these nanostructures), respectively. The values found in all cases are consistent with reported values for s–p hole energy differences in small QDs, being attributed the different values to the different lateral dimensions of the nanostructures. As aforementioned, the proposed rate equation model explains the evolution of the radiative and non-radiative exciton dynamics in the investigated temperature range. The thermalization between the ground and the first excited states dominates the intermediate temperature regime and is mediated by a thermally activated mechanism. However, this intermediate temperature behavior cannot be resolved from the dominant recombination mechanisms at low and high temperatures. At higher temperatures, carrier scape out of the nanostructures becomes important leading to a strong reduction of the exciton lifetime and the PL integrated intensity due to the non-radiative losses in the continuum states.

5.5 Resonant excitation

Figure 5.9 shows the changes produced in the QDhs PL spectra when laser excitation is done below the WL absorption edge (resonant excitation). Apart from the obvious reduction of the whole PL intensity, due to a large decrease of the absorption when exciting below the WL band edge (the carriers are being created directly at the nanostructures), we observed a clear change on the shape of the PL. The relative intensity of the three QDhs families that compose the normal PL spectra (above barrier excitation) varies strongly as the excitation energy is reduced.

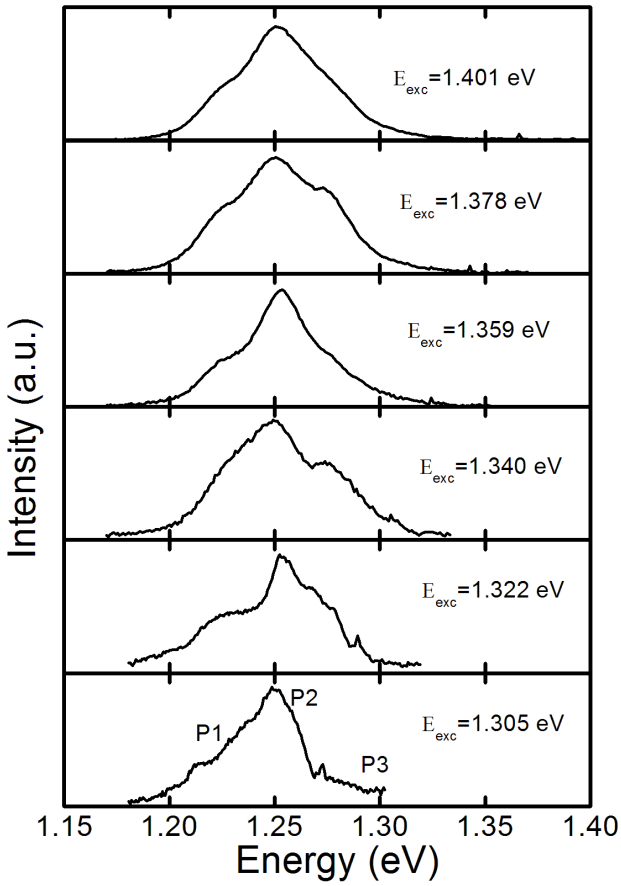

Figure 5.9: **Pls under resonant excitation.**

This observation is clearly consistent with the excited states picture presented in the previous sections. Excited states are split by the same energy for all families, but shifted in energy due to the different ground state energies. When exciting at a precise energy, we are more in resonance with the excited states of one family over the rest, creating more $e^- - h^+$ pairs *in the QDs* of that family, the feeding equilibrium is altered and the relative importance of the families changes as a consequence. In a similar way, the other two studied samples (QC and QR) show a reduction

of the PL FWHM, in this case there are not any families at all, so it is not expected any deep shape change, nevertheless the FWHM reduction is thought to come from the preponderance of well-formed QDs (the central part of the size distribution) absorption over the others.

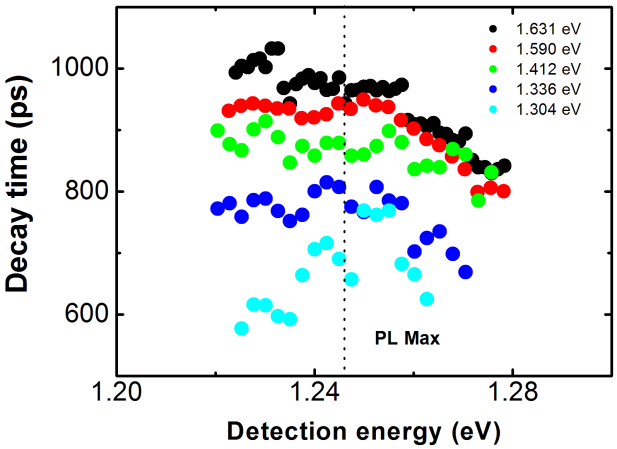

Figure 5.10: **Decay time evolution under resonant excitation.**

One interesting discussion going on the QD literature corresponds to the effect of correlated and uncorrelated capture of $e^- - h^+$ pairs and its effect on the linear or super-linear dependence of the integrated intensity with power[60]. In a recent work [63], the super-linear dependence of the QD emission intensity on the excitation power density under non resonant PL condition, is attributed to the saturation of temperature activated trap states, affecting the carrier diffusion in the barrier instead of being considered as the fingerprint of a decoupled electron and hole dynamics in the QDs[60]. On the contrary they observed a linear dependence of the integrated luminescence on excitation power, when the QDs are excited under resonant conditions, up to room temperature. This behavior suggested the presence of a high correlation of the time dependence between electron and hole populations in the QDs. In order to interpret their experimental data, they supposed the radiative recombination rate constant or invariable, but in our case, a strong reduction of the decay time is observed while reducing the excitation energy (figure 5.10); that reduction should be taken into

account during modeling and could represent a high impact on the final conclusions.

The origin of that strong reduction is not easy to be explained because the radiative decay time is related to the inverse of oscillator strength of the ground state transition. As long as the confining potential does not change the overlap of the electron and hole wavefunctions (lifetime) will not change. We can find a possible origin in a thermal influence due to the excess energy (effective temperature of the excitons) with respect to the ground state. We can expect a change of the capture mechanism and relaxation time, but it would not affect the measured decay time.

5.6 Conclusions.

We have investigated InGaAs self-assembled nanostructures whose size and shape strongly depend on a single overgrowth step introduced during the self-assembling process. We have found that their electronic structure differs appreciably from typical QDs emitting at 1.1 eV. On the one hand, due to their smaller height, we observe a strong blue shift of the ground state energy. In spite of the strong energy shift, the three-dimensional confinement is still very efficient in these nanostructures and the radiative lifetime measured at low temperatures is below 1 ns in all cases, thus producing strong emission bands. The excited state structure has been also investigated and correlated with the exciton recombination dynamics at low and high temperatures. We observe an important increase of the radiative lifetime with temperature, which is attributed to the thermalization between the ground radiative exciton state and the first excited dark state. A rate equation model has been developed to account for this exciton thermalization at intermediate temperatures and the non-radiative losses through WL states at high temperatures. The model reproduces our experimental data and gives insight on the exciton recombination dynamics in this system which should be taken into account in future design of devices. Experimental results under resonant excitation conditions show changes in the shape of PL spectra, while a strong reduction of the radiative recombination time appears. The origin of the exciton lifetime reduction cannot be understood without complicate theory out of the scope of this work.

Chapter 6

Single Quantum Dots

In this chapter, we present experimental data on single QDs. Low density samples used here are described in the first section of this chapter. The isolate optical properties of a single QD were characterized using the confocal microscope described in section 4.2.

The motivation to perform μPL combined with μTRPL is discussed on the framework of a microstate master equation model to account for the complete recombination dynamics at the ground state s-shell of a QD.

6.1 Low Growth Rate Samples

The InAs QDs investigated in this chapter were grown by the group of Prof. Secondo Franchi at the "Istituto dei Materiali per l'Elettronica ed il Magnetismo (Università di Parma and CNR, Parma, Italy)", by using the MBE technique on a GaAs semi-insulating substrate. The process starts with a 100 nm-thick GaAs buffer grown on a GaAs semi-insulating substrate at the temperature of 600 °C, followed by the InAs deposition at 505 °C of an equivalent coverage of 2.5 monolayers using a very low growth rate (0.009 ML/s) and ends with a 100 nm-thick GaAs cap layer grown by atomic layer MBE at 360 °C. Samples are not rotated during the growth procedure, producing a gradient in the QD density over the sample [64]. The combination of low growth rate (LGR) and graded coverage allows obtaining very low density samples, which are suitable for single

QD spectroscopy. In particular, the sample under study has a density of 16.5 QDs per μm^2, as estimated by atomic force microscopy images (see figure 6.1). In the laser spot in the confocal microscope we find a small amount of QDs, and due to their spectral dispersion, we can perfectly isolate the excitonic emission of a single QD.

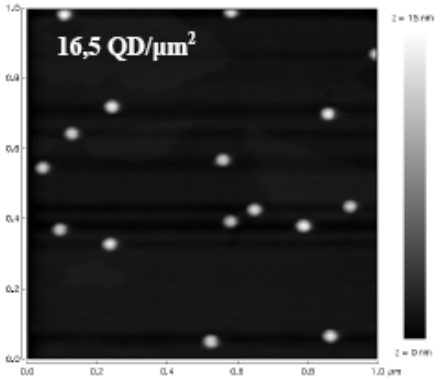

Figure 6.1: **AFM Image of the studied sample.**

Hall measurements of similarly grown GaAs buffer layers reveal a residual doping concentration $n = N_D - N_A \sim 10^{15}\text{cm}^{-3}$. This residual impurity concentration is not important in usual samples with higher dot densities, but it will play an important role in low density samples, as discussed in next section. The sample under study has been optically characterized in [65, 66]. Two QDs families are identified and emit in two different energy ranges. We will concentrate on the recombination dynamics of that emitting around 1.3 eV, because its emission lays on the energy range of Si-based detectors range and allows us to combine μPL and μTRPL at the same time. Macro– and micro– PL experiments as a function of excitation density confirm the existence of only one confined exciton shell (due to a s-shell for electrons), typically. Figure 6.2 shows the μPL evolution at different excitation powers of the typical emission of a Single QD of the SQD family under non resonant excitation (760 nm). The evolution of the PL integrated intensity below the labeled peaks is presented in the inset of figure 6.2. Peaks labeled X, X^+, X^- and XX stand for the different

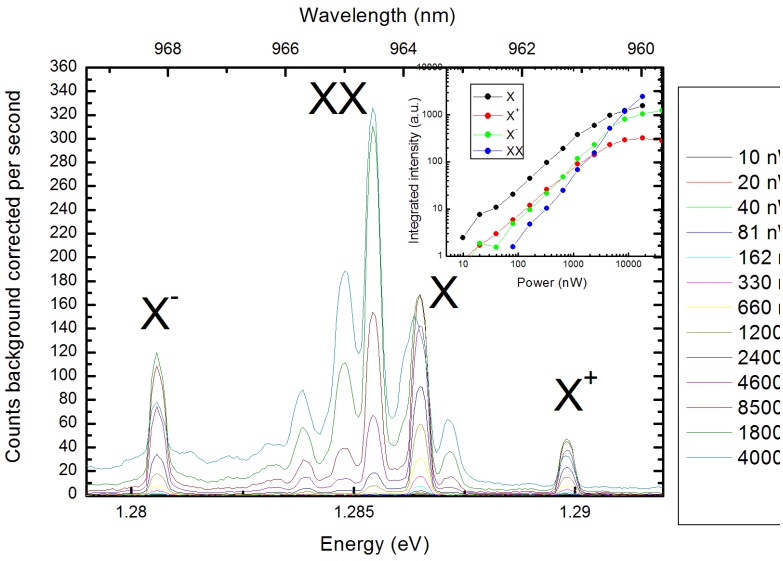

Figure 6.2: **Single QD μPL emission of a SQD type QD (labeled as QD1) as a function of reference power on CW excitation conditions. Inset presents the evolution of the integrated PL intensity.**

excitonic species presented in section 3.1.2. SQD-type QD emission follows a fixed pattern with power excitation, at least over ten different QD examinated through different experiments [65, 66, 67]. Low power excitation μPL is clearly dominated by the peak labeled X; it can be safely attributed to the exciton emission. As power increases the peaks labeled as X^+ and X^- appear at higher and lower energies with respect to the X peak emission, but never exceed the X–intensity. When an exciton recombines in a QD that has an additional uncorrelated particle on it, its emission energy experiments a coulomb correction, typically negative (positive) if the extra particle is an electron (hole). The energetic splittings measured in our QD agree with what is reported in In(Ga)As shallow single QDs [68, 69], even some dispersion is found depending on size and composition, inherent to real QDs, and affecting our QDs too, but it does not change the general trend. When increasing the excitation power, the biexcitonic emission (XX) appears and grows near quadratically, thus dominating the

μPL spectra at the highest powers. At such high levels of excitation, a background emission and some extra peaks appear; the extra peaks are attributed to higher charged particles (more probably XX configuration with negative/positive extra charges), while the background is attributed to an interaction with the WL continuum. The identification of X, XX and charged excitons has been also made by using polarization resolved μPL: X and XX peaks exhibit a opposite small energy shifts, whereas X^+ and X^-do not move. These features are known as the Fine Structure Splitting (FSS)[70].

6.1.1 Above barrier excitation dynamics

The appearance of charged excitonic species in above barrier excitation dynamics is attributed to uncorrelated capture of electrons and holes in the QD. Once a photon is absorbed above the WL, the different diffusion of electrons and holes (that have really different mobilities[71]) and their interaction with the QD environment allows the possibility of unpaired capture.

In Figure 6.3 we show a more detailed study of another QD, but this time μPLs are measured under pulsed excitation conditions, so μTRPL transients can be directly compared to their corresponding μPL spectra registered exactly at the same excitation conditions. We will come back to comparisons between both kinds of excitation (CW and Pulsed) later. As aforementioned, the energy splittings and the overall structure of the emission resembles the case presented in figure 6.2 and excitonic species are labeled accordingly; we can only observe a difference: the relative importance of X^+ and X^- is opposite this time, a clear hint that the capture of unbalanced charges depends on the interaction of the QD with its material environment and, as a consequence, is a phenomenon that can change locally. In the right part of figure 6.3, some TRPL transients are shown (if a peak of the μPL spectrum has lost its corresponding μTRPL transient is due to signal comparable/below the noise level).

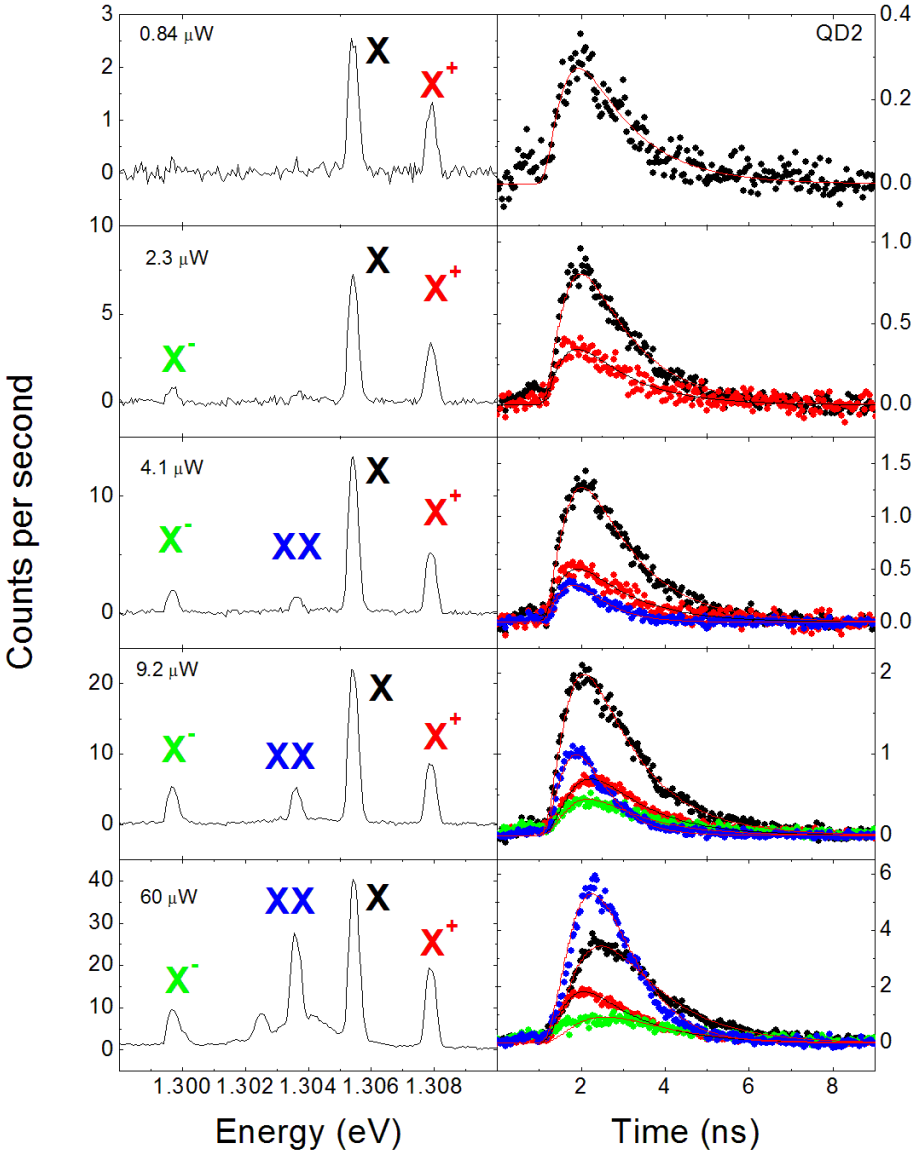

Figure 6.3: **μPL spectra under pulsed excitation conditions and μTRPL transients of a single QD (labeled as QD2) using optical pumping at 775 nm. Colors identify the right hand side TRPLs with their corresponding excitonic peak. Thin continous lines stand for fits to equation 6.1.**

The experimental μTRPL transients are represented by dots while a continuous line is used for the best fit. The fitting procedure takes into account the system response through a numerical convolution of the system response and the expression [72]:

$$A(e^{-\frac{t-t_0}{\tau_d}} - e^{-\frac{t-t_0}{\tau_r}}) \tag{6.1}$$

A first fitting of the different transients provides a consistent decay time (τ_d) value of 1.27 ns. The rise times (τ_r) are well below the experimental resolution until the largest excitation power: the FWHM of the TRPL system response is around 400 ps (see section 4.2.1). Even with this high FWHM value the fitting procedure can give us an approximate minimum deconvoluted time of around 100 ps. If one fixes the decay time and repeats the fittings (it reduces the variations induced by compensation between the values of decay and rise times), one can obtain the trend of the rise time when increasing the excitation power as represented in figure 6.4.

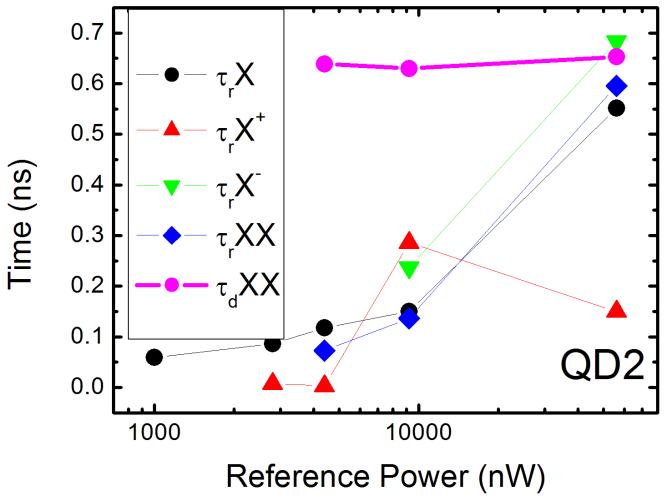

Figure 6.4: **Rise times of X, X^+, X^- and XX as a function of the excitation power obtained by fitting experimental results to 6.1. Decay time for XX is also plotted**

The biexciton decay time is found to be half of the excitonic lifetime,

reinforcing the labeling of X and XX lines made before. Rise times grow as power does, providing reliable values (above 100 ps) only for relatively high powers, when all the four excitonic species are present. The competition between quasiparticles is determining long values for their rise times. As an extreme example, while biexciton exists exciton recombination cannot take place, so the TRPL exciton rise time must increase, even for the biexciton itself. In order to measure excitonic capture times really low power excitation is needed; in this case only exciton emission should appear and the rise time extracted through the expression 6.1 would be approximately the exciton capture time. Following the tendency shown on figure 6.4, we can see that exciton capture time is well below the time resolution of our setup.

6.1.2 Optical switching

The spatial confinement of electrons in QDs protects their spin against the primary relaxation mechanism in bulk, that comes from coupling between spin and orbital momenta. As a result, spintronic looks at QDs as a promising solid-state candidate to implement devices for quantum computing. However, electron hyperfine interaction with the lattice nuclei is enhanced by confinement too, leading to spin decoherence and dephasing and, consequently, difficulting the processing of quantum information. Approaches using single charged quantum dots offer a robust solution to that problem, transforming electron hyperfine interaction with the lattice nuclei into an advantage [73, 74, 75]. The remaining electron after recombination provides a long decoherence time exceeding by several orders of magnitude the exciton lifetime. Different strategies are being used to control the charge inside a QD:

- n-modulation doping really near the QD layers. QDs are filled with extra electrons permanently; as an example, in references [74, 75] one electron per QD in average is expected with a doping nominally equal to the QD density .
- Coulomb Blockade effect in field effect samples.[43, 73]. Offers the chance to precisely control the amount of electrons in the QD by tuning the applied external voltage, however, the applied voltage

causes a shift in the entire spectrum and deforms the wave functions, which eventually leads to a relatively shift of the interaction energies [34].

- Optical methods:
  - Photodepletion mechanism[76], in which the initial situation is a charged dot (due to a strong impurity background) and optical excitation depletes this charge.
  - Different mobility of electrons and holes[71]. Determined, partially, by the energy excess of the excitation.
  - Resonant excitation into impurity levels originated by (non) intentional doping. An excess of electrons is generated and effectively captured into the QDs[77, 78]. A higher control of the exact charge at the QD could be achieved by combining this method with an extra infrared excitation below the QD ground state energy [79].

Optical switching is clearly observed in our sample [65, 67, 66]: strong differences in the μPL emission are detected as the excitation energy is shifted from non resonant to resonant with impurities. Changes in the emission ratio between the excitonic species by varying the excitation energy are also observed [71]. This situation is possible due to absorption from ionized acceptors towards ionized donors or the conduction band at the barriers.

A detailed evolution of the same QD of figure 6.3 is now shown in figure 6.6 under pulsed resonant excitation. In the left hand side of figure 6.6, it can be observed that the intensity of the previously identified peaks suffers a dramatic change. Now the negative charged exciton dominates the emission spectra at moderate and high excitation powers, while the exciton peak is still the most intense line at the lowest power.

Right panels in figure 6.6 correspond to the μTRPLs transients of the different excitonic peaks at the left panels. We appreciate that the neutral exciton recombination clearly appears (max. intensity) before that of the negative trion; at least for the lowest excitation powers (8 and 16 μW), even if the X^- line ends dominating the temporal emission after some ns.

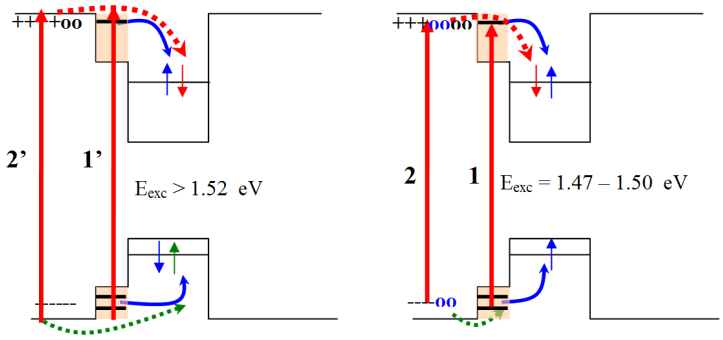

Figure 6.5: **Energy level sketch of the Optical Switching origin. Arrows refer to the capture possibilities: under excitation above barrier ($E_{exc} >$ 1.52 eV), e^--h^+ uncorrelated(1' arrow) and exciton capture(2' arrow). When resonant to the impurities levels($E_{exc} = 1.47 - 1.50$ eV), exciton capture into the WL states (1 arrow) and D^0C^0/e^-C^0 transition (2 arrow).**

One can safely infer that the injection of an electron excess in the QD under resonant excitation with the impurity level is slower than the direct capture: an outstanding delay around 300-400 ps is observed (it is clearer for lower excitation power, where there is not any "competition" among the excitonic species to hide the capture delay). This delay could be used to locate the impurities with respect to the QD if one could estimate exactly the electron mobility in the sample at 10 K.

μTRPL transients are taken under pulsed and periodic excitation, in this case a pulsed diode laser set to work at 40 MHz (25 ns of period). *The resulting μTRPL is not the result of one isolated event, it is the statistical result of a huge amount of events, all of them responding to a particular QD situation.* What can be positively stated about that events is that *all events are preceded by a previous excitation 25 ns before.*

After the negative trion recombination, an unpaired electron remains in the QD. If this electron stays in the QD until next excitation, the capture of an exciton would lead to another emission of a trion and the emission of neutral exciton would become impossible.

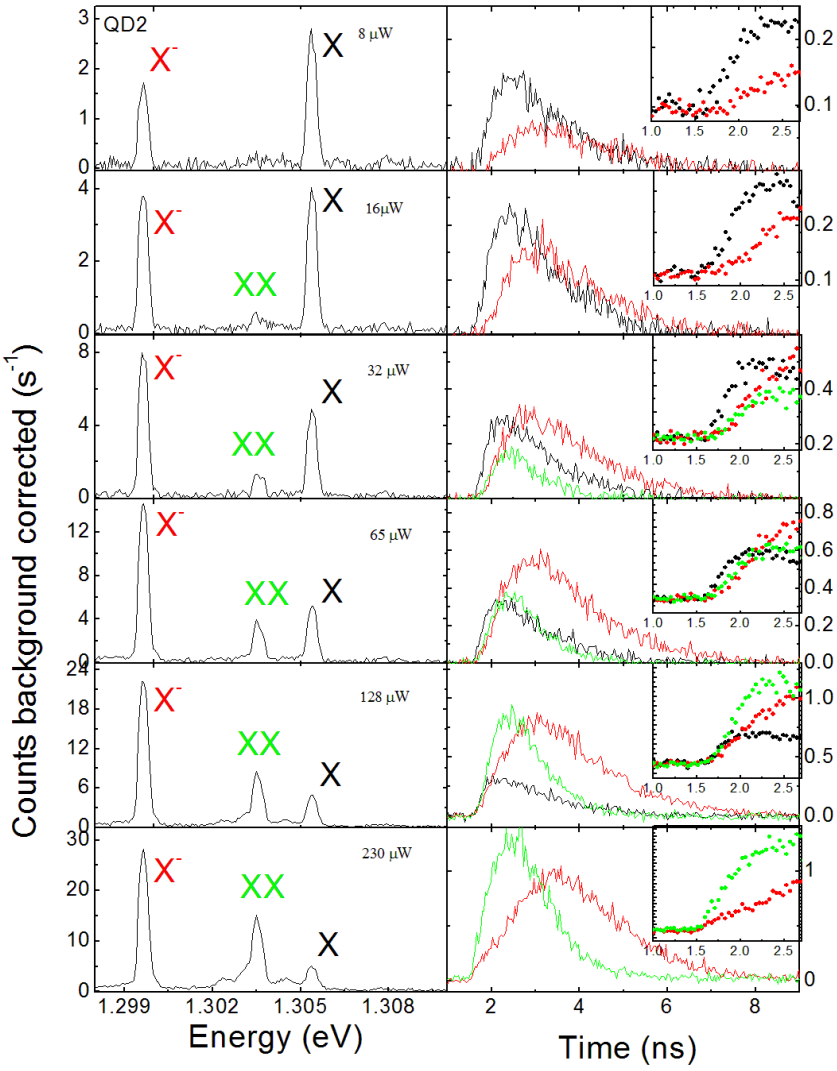

Figure 6.6: **μPL spectra under pulsed excitation conditions and μTRPL transients of the same single QD of figure 6.3 but exciting at a wavelength of 830 nm. Colors identify the right hand side TRPLs with their corresponding excitonic peak. The insets zoom the first PL transient rising.**

The fact that the TRPL of the exciton appears before the trion emission directly suggests two possible situations:

- after being captured the electron escapes out of the QD between excitations (an average lifetime in the range of the repetition period, 25 ns)
- when a QD is negatively charged holes are captured faster (geminate capture (see section 3.3.3)), enhanced by the coulomb attraction, leading to a final neutral emission.

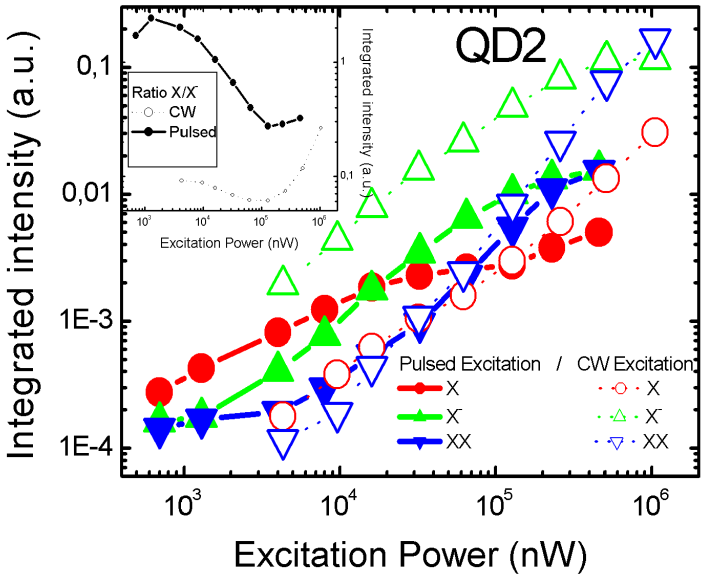

Figure 6.7: **Integrated intensity evolution exciting at 830 nm. Thick lines and symbols correspond to pulsed excitation, dashed lines and symbols to continuous wave.**

Comparing CW and Pulsed excitation at 830 nm will help us to discern between both possibilities: in figure 6.7 IPL for both excitation conditions. The most striking observation is the complete change in the X/X^- ratio; while in CW excitation the X^- dominates the emission with a marginal

contribution of the X line at high powers, in pulsed excitation the X line dominates the emission at low-medium powers.

In CW excitation there is not a fixed separation time between excitation events, which results in a continuous electron injection in the QD (under excitation at 830 nm) and hence a clear predominance of the negative trion emission. On the contrary, exciton emission dominates under pulsed excitation. This behavior suggests that after a "long period" without electron injection, the injected "extra" electron escapes out of the QD, leaving it in its original empty situation. The electron non radiative escape out of the QD at 10 K has not a straight forward explanation. Direct or phonon assisted tunneling is not probable without the existence of an accessible electronic level, like a neighbor QD. The access towards WL states by thermal scape would be a possibility given the small energy difference from the QD ground state. This energy can be only some meV and hence not very large compared to the small thermal energy at 10 K ($\sim$ 0-9 meV).

Time resolved two excitation color experiments could provide a way to directly extract the time constant associated to that mechanism, using a low power non resonant pulse to monitor the QD excitonic emission after a C^--CB delayed resonant excitation.

6.2 Microstates approach to describe the excitonic dynamics

In a preliminary work[67], we proposed an adaptation of the Master Equation Microstate (MEM) model to reproduce the capture and recombination dynamics of the different exciton species in a shallow confined single QD (only one electron shell confined (s shell, s_e-s_h). Our model was parameterized by using like inputs the time constants directly deduced from Time Resolved Photoluminescence (TRPL) experiments in the same single QD studied under continuous wave (CW) conditions. The model was applied to the description of the PL intensity as a function of the CW power. Throughout this section we will explain the Master equation microstate model and check the validity of our assumptions when comparing its application to the experimental data.

6.2.1 Model description

Figure 6.8 presents a flow diagram of the MEM model. Boxes represent the different charge configuration that a QD can present (microstate), the left number in the box specifies the amount of electrons in the ground electron s shell (s_e), while the right number refers to the amount of holes in the ground hole s shell (s_h). Some Microstates can be easily labeled as the conventional excitonic species: [1 1] ≡ X, [2 1] ≡ X^-, [1 2] ≡ X^+ and [2 2] ≡ XX, while [0 0] is an empty QD. Coloured arrows refer to the possible mechanisms that effectively change the charge inside the QD: their result is always a microstate change.

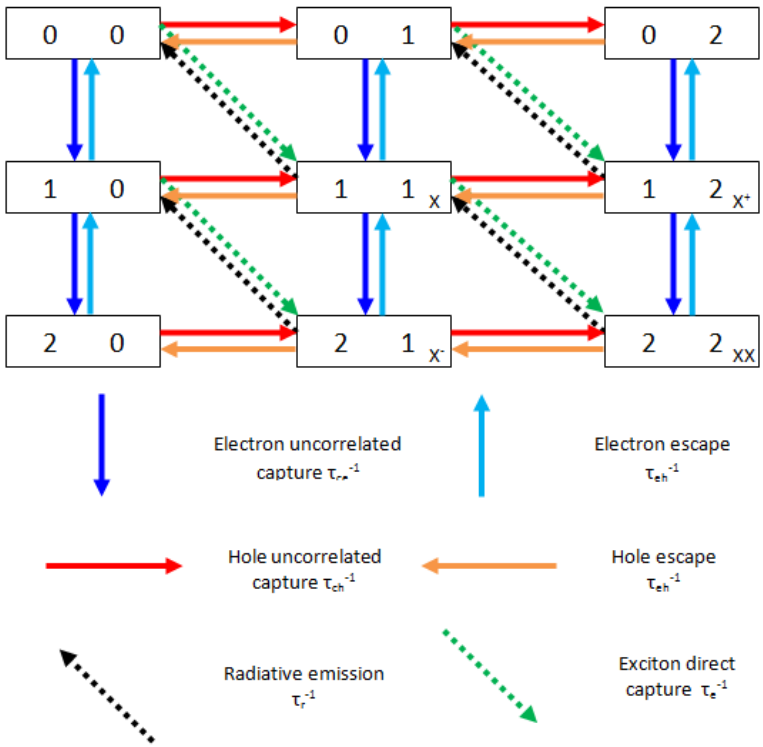

Figure 6.8: **Diagram of the MEM model**

MEM were developed to be applied on QD ensembles [13]; but all spectroscopy measurements shown here for a single QD are the result of

multiple emissions at different times. In this case, we can treat the optical properties of a single QD as generated by a "temporal ensemble". On a time acquisition lapse of one second excited by a 40 MHz pulsed laser is the result of 4 10^7 excitation cycles. Every of those cycles can be understood as an independent virtual QD-event. The temporal superposition of all QD-events will be a given μPL/μTRPL measurement, just that we are calling a "temporal ensemble". Following this argument, every microstate will represent the amount of QDs of our "temporal ensemble" that can be found with a particular electronic configuration. For example, before any excitation the QD is empty in all the periodic cycles, all virtual QDs of that "temporal ensemble" are in the [0,0] configuration, and the microstate populations ($n_{s_e,s_h} = n_{ij}$ with $i,j = 0,1,2$) are:

$$\begin{aligned} n_{00} &= N_{QDs}, \\ n_{01} &= n_{02} = n_{10} = n_{11} = n_{12} = n_{20} = n_{21} = n_{22} = 0 \end{aligned} \tag{6.2}$$

Imagine that only an exciton is captured in one of the excitation cycles. The virtual QD corresponding to that cycle would transform from empty to occupied with one exciton and, as a consequence the QD would change its microstate ($n_{00} \rightarrow n11$). The total microstate population would evolve to:

$$\begin{aligned} n_{00} &= N_{QDs} - 1, \\ n_{11} &= 1, \\ n_{01} &= n_{02} = n_{10} = n_{12} = n_{20} = n_{21} = n_{22} = 0 \end{aligned} \tag{6.3}$$

The sum of all microstate populations remains always fixed to the total amount of virtual QDs (N_{QDs}). If we normalize the microstates population, that is, we set N_{QDs} to 1, the microstate population directly refers to the probability of finding the QD in a particular microstate.

The QD is charged via the WL in two different ways: correlated exciton capture and uncorrelated e^- and h^+ capture. In this way, two different WL level structures for both kinds of capture mechanisms are considered, as sketched in figure 6.9. In addition, an ID level is included to account for the extra e^- injected when optical pumping is resonant to the ionized impurity levels.

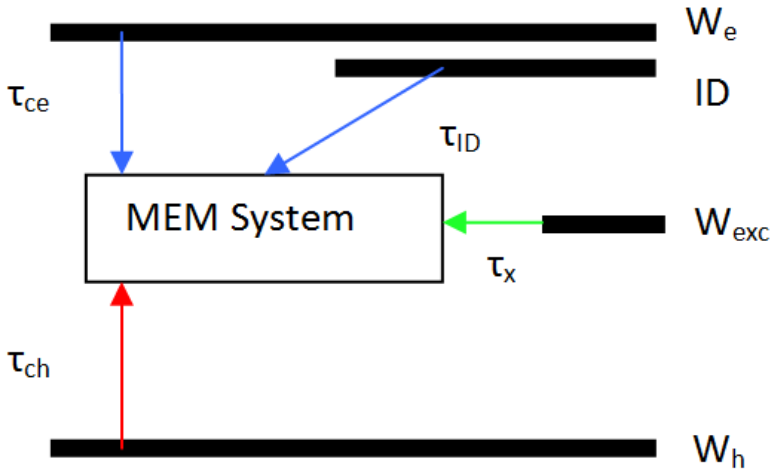

Figure 6.9: **Interaction between the QD and its environment in the MEM model. WL_{exc} corresponds to the WL level for exciton correlated capture, WL_e and WL_h to the WL levels for uncorrelated electron and hole captures, respectively and ID is the source for extra electrons under resonant excitation to the impurity levels. The time constants $\tau_X, \tau_{ce}, \tau_{ch}, \tau_{ID}$ are the QD capture times from WL_{exc}, WL_e, WL_h and ID levels, respectively.**

The dynamics of the system is governed by the following differential equations system:

$$\begin{aligned}
\frac{dn_{ij}}{dt} &= R_{ij}^{exc} WL_{exc} + R_{ij}^{e} WL_e + R_{ij}^{h} WL_h \\
&\quad + R_{ij}^{ee} - R_{ij}^{eh} + R_{ij}^{ID} ID - R_{ij}^{r}, \qquad (6.4)\\
\frac{dWL_{exc}}{dt} &= \sum_{ij} E_{ij} R_{ij}^{exc} WL_{exc} - \frac{WL_{exc}}{\tau_W} + G_a, \qquad (6.5)\\
\frac{dWL_e}{dt} &= \sum_{ij} i R_{ij}^{e} WL_e - \frac{WL_e}{\tau_W} + G_b, \qquad (6.6)\\
\frac{dWL_h}{dt} &= \sum_{ij} j R_{ij}^{h} WL_h - \frac{WL_h}{\tau_W} + G_b \qquad (6.7)
\end{aligned}$$

$$\frac{dID}{dt} = i\sum_{ij} R_{ij}^{ID} ID + G_c \tag{6.8}$$

G_a, G_b and G_c are the excitation parameters to the levels WL_{exc}, WL_e (WL_h) and ID, respectively. The population at WL_e and WL_h is symmetrically generated under above barrier excitation. The R_{ij} terms refer to the capture or escape/lose processes that a single QD can experiment, as indicated by arrows in figure 6.8. Obviously these terms depend on the particular configuration of the QD. For example, and empty QD can not lose an exciton via radiative decay. The overall "temporal ensemble" evolution depends on the probability of finding the QD in every microstate. In the following subsections we will describe and explain these R_{ij} terms. Firstly we introduce the microstate population in a matrix-like formalism:

$$n_{ij} = \begin{pmatrix} n_{00} & n_{01} & n_{02} \\ n_{10} & n_{11} & n_{12} \\ n_{20} & n_{21} & n_{22} \end{pmatrix} \equiv \mathbf{N} \tag{6.9}$$

6.2.2 Correlated exciton capture

Correlated exciton capture (dashed green arrow in figure 6.8) is accounted through the term R_{ij}^{exc} in equations 6.5 and 6.6. If one defines τ_X as the exciton capture time of an empty QD, the probability that a microstate loses population through exciton correlated capture is:

$$\mathbf{R}_{out}^{exc} = \frac{1}{\tau_X}\begin{pmatrix} 1 & \frac{3}{4} & 0 \\ \frac{3}{4} & \frac{1}{2} & 0 \\ 0 & 0 & 0 \end{pmatrix} * \mathbf{N} = \frac{1}{\tau_X}\begin{pmatrix} n_{00} & \frac{3}{4}n_{01} & 0 \\ \frac{3}{4}n_{10} & \frac{1}{2}n_{11} & 0 \\ 0 & 0 & 0 \end{pmatrix} \tag{6.10}$$

Note that we have defined multiplication element by element and not an usual Matrix multiplication. The probability that an empty QD captures an exciton is proportional to $\frac{1}{\tau_X}$ and the percentage of the virtual QD on our temporal ensemble that are empty (n_{00}). In contrast, in a half full configuration, like $[1,1]$, the probability is $\frac{1}{2\tau_X}n_{11}$; the factor $\frac{1}{2}$ comes from the fact that the QD in that configuration has only one free exciton level ($s_e - s_h$) instead of two. Probabilities for $[0,1]$ and $[1,0]$ are set to $\frac{3}{4\tau_e}n_{01}$ and $\frac{3}{4\tau_e}n_{10}$ following similar reasonings. For the rest of microstates the probability of losing population through a correlate exciton capture is

null (as an example, a QD with 2 e^- in s_e can not capture an additional exciton, only an uncorrelated hole to complete one exciton). Let remember that the sum of all microstate probabilities is always one: the decrease in population of one microstate results in an increase of the population by other microstate. It strictly means that the increment on n_{11}, n_{12}, n_{21} and n_{22} due to correlated exciton capture is due to the corresponding population decrease in n_{00}, n_{01}, n_{10} and n_{11}, respectively. In this way, we can define the "in" matrix like:

$$\mathbf{R}_{in}^{exc} = \begin{pmatrix} 0 & 0 & 0 \\ 0 & (\mathbf{R}_{out}^{exc})_{00} & (\mathbf{R}_{out}^{exc})_{01} \\ 0 & (\mathbf{R}_{out}^{exc})_{10} & (\mathbf{R}_{out}^{exc})_{11} \end{pmatrix} \tag{6.11}$$

The effective change in the dot microstates induced by correlated exciton capture in our temporal ensemble will be:

$$\mathbf{R}^{exc} = R_{ij}^{exc} = \mathbf{R}_{in}^{exc} - \mathbf{R}_{out}^{exc} \tag{6.12}$$

The amount of excitons actually captured from the WL_{exc} level can be calculated as a function of the MEM's induced population change, $\mathbf{R}^{exc}$, by taking into account how much excitons can be found in a particular microstate (E_{ij}). It gives the term in equation 6.6:

$$\sum_{ij} E_{ij} R_{ij}^{exc} WL_{exc} \tag{6.13}$$

Where E_{ij}, excitons in the microstrate $[i, j]$, are the terms of the matrix:

$$\mathbf{E} = \begin{pmatrix} 0 & 0 & 0 \\ 0 & 1 & 1 \\ 0 & 1 & 2 \end{pmatrix} \tag{6.14}$$

6.2.3 Uncorrelated $e^- - h^+$ capture

The arguments given in the last subsection can be also applied to uncorrelated $e^- - h^+$ capture (dark blue and red arrows in figure 6.8); free spaces in the receptor levels (s_e for e^- and s_h for h^+) determine the factors applied

to every microstate:

$$\mathbf{R}^e_{out} = \frac{1}{\tau_{ce}} \begin{pmatrix} 1 & 1 & 1 \\ \frac{1}{2} & \frac{1}{2} & \frac{1}{2} \\ 0 & 0 & 0 \end{pmatrix} * \mathbf{N} \quad , \tag{6.15}$$

$$\mathbf{R}^e_{in} = \begin{pmatrix} 0 & 0 & 0 \\ (\mathbf{R}^e_{out})_{00} & (\mathbf{R}^e_{out})_{01} & (\mathbf{R}^e_{out})_{02} \\ (\mathbf{R}^e_{out})_{10} & (\mathbf{R}^e_{out})_{11} & (\mathbf{R}^e_{out})_{12} \end{pmatrix}$$

$$\mathbf{R}^h_{out} = \frac{1}{\tau_{ch}} \begin{pmatrix} 1 & \frac{1}{2} & 0 \\ 1 & \frac{1}{2} & 0 \\ 1 & \frac{1}{2} & 0 \end{pmatrix} * \mathbf{N} \quad , \quad \mathbf{R}^h_{in} = \begin{pmatrix} 0 & (\mathbf{R}^e_{out})_{00} & (\mathbf{R}^e_{out})_{01} \\ 0 & (\mathbf{R}^e_{out})_{10} & (\mathbf{R}^e_{out})_{11} \\ 0 & (\mathbf{R}^e_{out})_{20} & (\mathbf{R}^e_{out})_{21} \end{pmatrix} \tag{6.16}$$

The changes induced in the MEM system through these processes are:

$$\mathbf{R}^e = R^e_{ij} = \mathbf{R}^e_{in} - \mathbf{R}^e_{out} \tag{6.17}$$

$$\mathbf{R}^h = R^h_{ij} = \mathbf{R}^h_{in} - \mathbf{R}^h_{out} \tag{6.18}$$

The changes in the feeding levels, WL_e and WL_h, that is, the amount of captured e^- and h^+, are calculated (in equations 6.7 and 6.8) as a function of R^e_{ij} and R^h_{ij} and the amount of e^- (i) and h^+ (j) in microstates [i,j].

6.2.4 Radiative decay

At cryogenic temperatures radiative recombination is the main mechanism for exciton losses. In our shallow QD the biexciton lifetime (0.65 ns, as plotted in figure 6.3) is half the exciton lifetime (1.27 ns). The radiative recombination probability is the same for every exciton: the two electrons at s_e can recombine with equal probability with every of the two holes at s_h. However, not all quantum dots exhibit the same behaviour [80]. In our MEM approach, the radiative recombination term reads as:

$$\mathbf{R}^r = \frac{1}{\tau_r} \begin{pmatrix} 0 & 0 & 0 \\ 0 & 1 & 1 \\ 0 & 1 & 2 \end{pmatrix} * \mathbf{N} \tag{6.19}$$

6.2.5 Injection of e^- under excitation resonant with impurities

Normally one could use an extra amount of e^- in the WL_e level to simulate the previously experimentally discussed effect of resonant pumping into the impurity energy levels. However, the spatial distance between the excited impurities and the QD should play a role in the electron capture time. In order to differentiate both processes, uncorrelated e^- capture and impurity mediated injection, we have included and extra level in our model that allows us to modify this capture time of electrons and its delay (as experimentally observed), independently. Further discussion on the delay time will be held in section 6.3. The matrix term $\mathbf{R}^{ID}$ has the same functional terms as $\mathbf{R}^e$, as both account for the same conceptual problem, uncorrelated e^- capture, but coming from different energetic levels and thus with different times. Now τ_{ID} applies to the transfer of e^- from impurities towards microstates, but we also take into account a delayed arrival of electrons after the pumping pulse.

6.2.6 Uncorrelated escape out of the QD

Evidences of the uncorrelated carrier scape out of QD was experimentally inferred (section 6.1.2) for excitation resonant to the impurity levels, even if they are not expected at cryogenic temperatures due to the low phonon occupation and the small number of receptor levels for tunneling processes. An alternative mechanism is the non radiative transfer towards deep levels acting like electron traps. Uncorrelated hole scape could be also a feasible possibility if one thinks in the effect of a remaining positive charge in the QD long after excitation (it would enhance strongly X^- emission). This kind of effect needs a careful and quantitative study; wich can be performed within the MEM model framework. When inspecting the outcoming data of the model (next section) we will come back to reconsider the role of uncorrelated e^-/h^+ escape. However, we have to include this mechanism in our model if we want to discuss its influence on the optical properties

of a single QD:

$$\mathbf{R}^{ee}_{out} = \frac{1}{\tau_{ee}} \begin{pmatrix} 0 & 0 & 0 \\ 1 & 1 & 1 \\ 2 & 2 & 2 \end{pmatrix} * \mathbf{N} \quad , \tag{6.20}$$

$$\mathbf{R}^{ee}_{in} = \begin{pmatrix} (\mathbf{R}^{ee}_{out})_{10} & (\mathbf{R}^{ee}_{out})_{11} & (\mathbf{R}^{ee}_{out})_{12} \\ (\mathbf{R}^{ee}_{out})_{20} & (\mathbf{R}^{ee}_{out})_{21} & (\mathbf{R}^{ee}_{out})_{22} \\ 0 & 0 & 0 \end{pmatrix}$$

$$\mathbf{R}^{eh}_{out} = \frac{1}{\tau_{eh}} \begin{pmatrix} 0 & 1 & 2 \\ 0 & 1 & 2 \\ 0 & 1 & 2 \end{pmatrix} * \mathbf{N} \quad , \quad \mathbf{R}^{eh}_{in} = \begin{pmatrix} (\mathbf{R}^{eh}_{out})_{01} & (\mathbf{R}^{eh}_{out})_{02} & 0 \\ (\mathbf{R}^{eh}_{out})_{11} & (\mathbf{R}^{eh}_{out})_{12} & 0 \\ (\mathbf{R}^{eh}_{out})_{21} & (\mathbf{R}^{eh}_{out})_{22} & 0 \end{pmatrix} \tag{6.21}$$

Exciton escape as a whole should not have a consequence on the QD dynamics, because its effects would be equivalent to a reduction of the exciton capture. At low temperatures the scape of an exciton is even more improbable than the uncorrelated scape (the energy confining an exciton is the sum of the energies confining e^- and h^- plus the correction due to the binding energy). For the sake of simplicity we will not consider exciton scape in an explicit way.

6.3 Simulation with the MEM model of CW and pulsed μPL

The inputs to the MEM system come from the parameters controlling the aforementioned processes. The output of the MEM model is the population of different microstates as a function of time. For both excitation conditions the μPL emission of X, X^-, X^+ and XX can be directly compared with the calculated population of [1,1], [2,1], [1,2] and [2,2] microstates. The master equation for microstates is a non linear coupled differential equation system that has no analytical solution. The numerical integration is carried out with a commercial routine (from Matlab) based on an explicit Runge-Kutta formula, the Dormand-Prince pair. The initial conditions of our MEM system can be particularly specified, but normally the initial state is an empty QD, $n_{00} = 1$ and $n_{ij\neq 00} = 0$.

The injection terms (G_a, G_b and G_c in equations 6.6 to 6.8) produce populations in the 2D levels (WL_{exc}, WL_e, WL_h and ID) that induces

changes in the microstate occupation probability through carrier trapping/escape from the QD. The continuous wave pumping evolves towards an equilibrium situation, i.e. a steady state solution, that can be calculated setting to zero the derivative terms in equation 6.6. The system is non linear and has no analytical solution, which forces us to get a numerical solution. In figure 6.10, we solve the original differential non linear equation system by using constant injection terms (G_a, G_b or G_c). The output of the MEM model is a **time dependent** population evolution that ends up converging to well defined values in less than 2 μs after the injection. These equilibrium values (microstate occupancies) will correspond to the steady state solution (derivative terms equal to zero) and they can also be directly compared with the μPL intensity for the different excitonic species under CW excitation. The variation of the pumping parameters allows us to reproduce the experimental power dependence of the μPL intensity (IPLs) (see figure 6.7 or inset of figure 6.2, for example). One of the

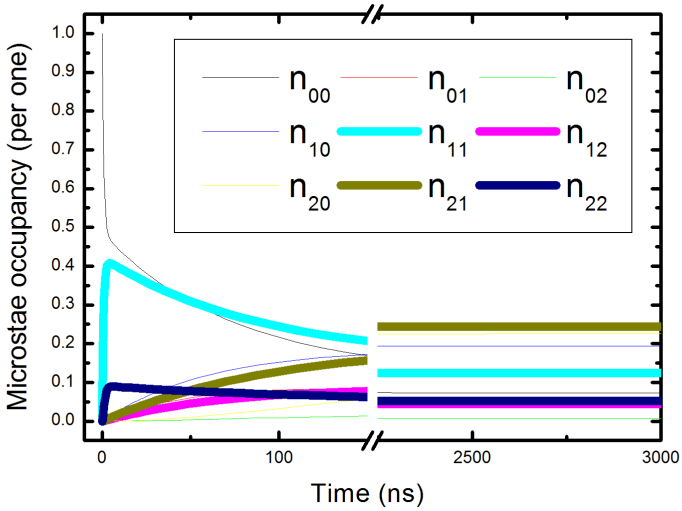

Figure 6.10: **MEM typical output. Thicker lines correspond to X(n_{11}), X^+(n_{12}), X^-(n_{21}), XX(n_{22}). Values used:** $G_a = 0.1\,excitons/ns, G_b = 0.02\,e^- - h^+/ns, G_c = 0, \tau_{ch} = 0.3\,ns, \tau_{ce} = 0.7\,ns, \tau_{eh} = 40\,ns, \tau_{ee} = 12\,ns, \tau_X = 5\,ps, \tau_r = 1\,ns, \tau_W = 0.45\,ns$

main tools to identify exciton and biexciton is the slope of their IPL power dependence. The slope of the exciton emission in a double logarithmic plot IPL vs. excitation power should be close to 1, as the excitonic emission process is related one to one with e^--h^-/excitons created through optical injection. The slope for biexcitonic emission should be near 2 because absorption of two excitons is needed in this case.

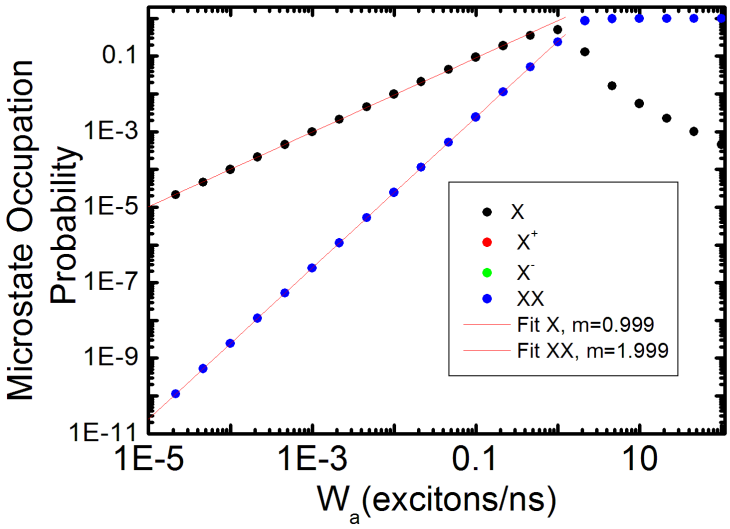

Figure 6.11: **MEM output for only exciton capture and no escape mechanism**

Figure 6.11 shows a MEM output as a function of the excitation power when only correlated exciton capture is considered. The slopes of X (0.99) and XX(1.99) nicely reproduce the ideal situation. A saturation plateau zone is achieved for a nominal excitation of 1 exciton/ns (1 ns is chosen as the exciton radiative lifetime in this simulation). The XX emission intensity grows at expenses of a reduction in the X emission intensity, leading to a XX probability close to one. There is no emission observed for X^- and X^+. The emission peaks X^- and X^+ appear when uncorrelated capture is considered, which is not the case of this example.

The situation depicted in figure 6.12 is just the contrary to that illus-

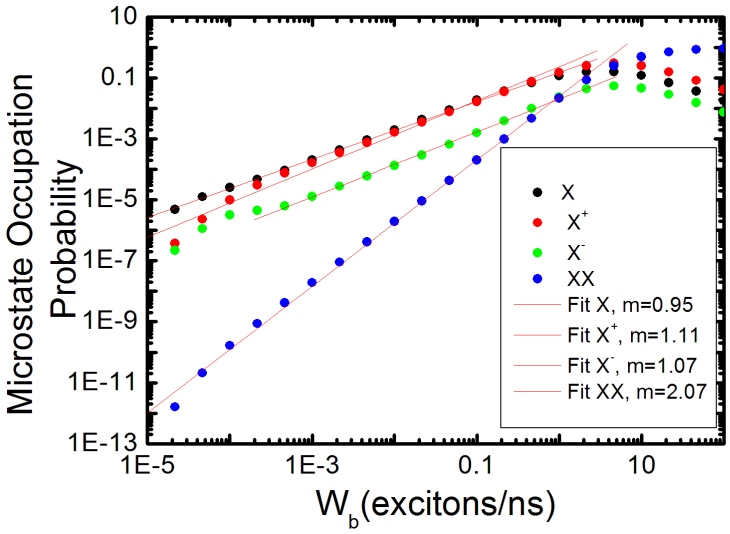

Figure 6.12: **MEM output for only uncorrelated e^--h^- capture and no escape mechanism**

trated above, i.e. only uncorrelated capture of e^- and h^+. In this case we do not observe a linear dependence over the whole power range. When the linear behavior is observed, the slopes for X and XX species present values slightly different from 1 or 2. The biexciton emission can be still identified through a near 2 slope. Our experiment observations under non resonant excitation did not exhibit trion dominating over X emission. One can guess that correlated and uncorrelated capture will be both present at the same time. Exciton emission will continue to dominate the emission at low powers as occurs in the example shown in figure 6.12. Let note that residual e^- or h^+ tend to be compensated by the capture of its antagonist particle (and hence contributing to enhance the X emission).

6.3.1 MEM approach to uncorrelated escape of carriers

As introduced in subsection 6.2.6, the impact of uncorrelated escape on the single QD dynamics is difficult to quantify, if exists. There are not direct measurements of the process itself and no concrete time frames attributed

to that process.

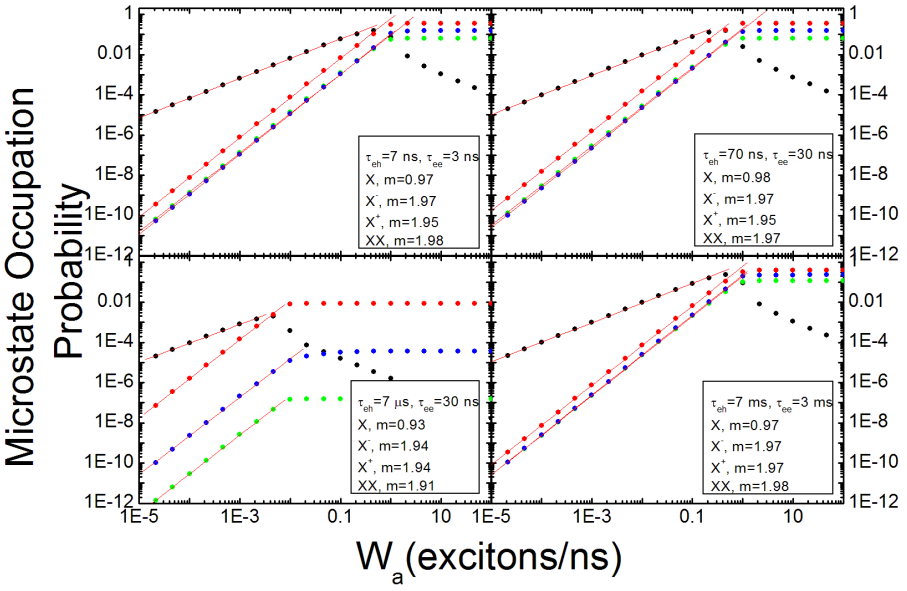

Figure 6.13: **MEM output for only uncorrelated e^--h^- capture and uncorrelated e^--h^- escape**

In order to simplify the analysis, we limit the study of the uncorrelated e^--h^+ escape to the case of correlated capture. If we include uncorrelated capture we will mask the effects, but conclusions should be very similar. Figure 6.13 shows IPL simulations for different escape constants, particularly changing the values of τ_{eh} and τ_{ee} from the ns range to the ms range. Long electron and hole escape times are needed to recover the ideal situation of figure 6.11 being comparable to the measuring time used to acquire the μPLs. Varying τ_{eh} and τ_{ee} we can change the relative importance of the trion ratios and the saturation points, but the main feature of the simulations remains unchanged: the slope of X^- and X^+ is around 2 independently of the time range considered. Conceptually, it is clear that the trion emission should exhibit a biexcitonic behaviour within the theory framework used here, because two exciton absorption is needed to arrive

to the trion configuration. After that, one of the captured excitons can lose one of the carriers to vary the QD electronic configuration to the trion state. The trion slopes found in ours experiments are all equal or below one (as also referred commonly in literature). As a consequence, we can rule out that uncorrelated e^--h^+ scape as a remarkable effect in the time frame used to measure our QD.

6.4 Fitting experimental data.

With the aim of checking the suitability of the developed model to the experimental results, we have developed a fitting routine for both, CW and TRPL experiments.

6.4.1 Above barrier CW excitation

For the CW fitting, some of the main parameters are chosen following the direct experimental measurements: $\tau_{WL} = 0.45$ ns, $\tau_r = 1$ ns (We have used $\tau_r = 1$ ns instead of $\tau_r = 1.27$ ns value obtained through a monoexponential fit because we find better agreement in the TRPL fittings for all species with a reduced value (as shown below in figures 6.15 and 6.16)). For τ_X, the capture time for excitons, well below our time resolution, we use a value taken from literature $\tau_X = 5$ ps [28].

Table 6.1: CW Fitting parameters corresponding to figure 6.14

τ_{ch}	78 ps
τ_{ce}	20 ps
% of uncorrelated captures	2.310^{-3}

The axes in figure 6.14 also form part of the fitting result. A nice agreement is observed for the power dependence of all excitonic species, except the biexciton, for which the model overestimates the slope of the power dependence and the saturation value. The MEM result for XX fits better to the blue open circles that takes into account the existence of higher charged particles (XX^* extra peaks in high power spectrums of figure 6.2) and a background lying under the excitonic emission peaks for

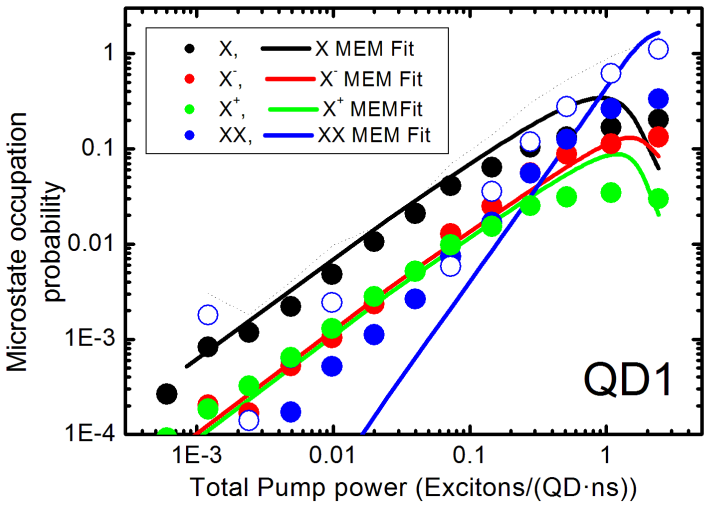

Figure 6.14: **Integrated intensity evolution under above barrier exitation. Solid lines correspond to the outcome of the MEM model for values on table 6.1. Dashed black line corresponds to the integration of the full Single QD spectra, open blue circles are calculated by the subtracting the sum of IPL of X, X^- and X^+ to the black dashed line.**

the highest excitation powers. A better agreement could be obtained by adding to the model excited microstates and/or screening effects with the environment, but it will increase the time to perform an operative fitting procedure to the experimental results, as done in this work.

Even limiting the model accuracy to low powers, a relevant conclusion can be extracted out of the fitting parameters: a really small amount of uncorrelated captures ($2.3\ 10^{-3}$ %) has a dramatic impact on the appearance of charged excitons.

6.4.2 Above barrier pulsed excitation

In order to fit time resolved experiments, a special variation of the MEM model has been developed. Delta like functions are used as excitation, and the temporal evolution during a τ_{rep} (the repetition time of the pulse

laser used) is calculated; empty QDs and WL are used as the first initial conditions, but the results (the resulting microstate populations) after τ_{rep} are used as new initial conditions for the new pulse arrival and so on. Let remember that 1s represents 76 10^6 cycles in the Ti:sapphire used in the present experiment, but such a huge amount of repetitions is not necessary and out of our computational capabilities.

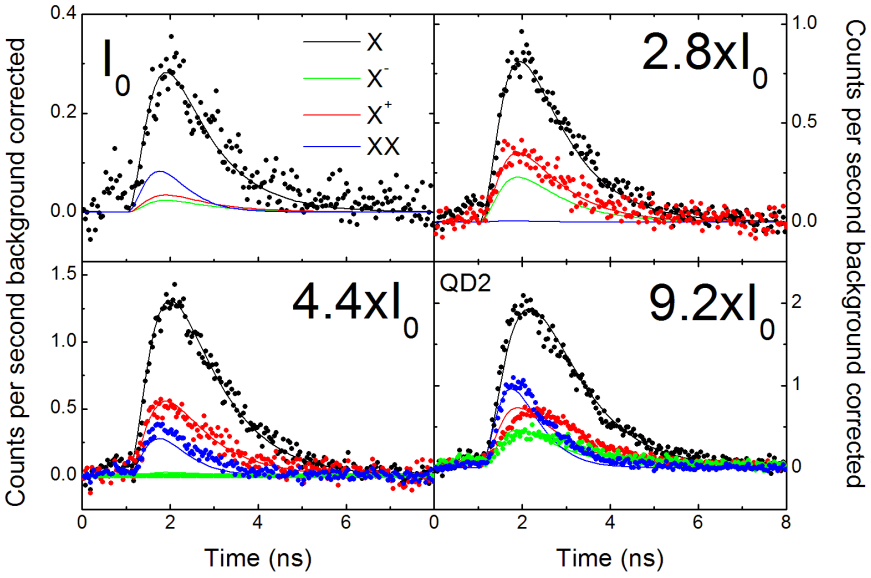

Figure 6.15: **Time resolved photoluminescence evolution under above barrier excitation. Solid lines correspond to the outcome of the MEM model for the values on table 6.2. Only 50 pulses are simulated.**

Table 6.2: TRPL under Non resonant excitation fitting parameters corresponding to figure 6.15

τ_{ch}	1 ns
τ_{ce}	1.6 ns
% of uncorrelated captures	7

Even with this clear drawback, in figure 6.15 we can have a taste of how this could be done. The best fitting parameters listed in table 6.1 were obtained by minimising the four situations depicted in figure 6.15 by using 50 cycles of excitations. When comparing these values to the ones obtained in the CW fitting procedure (τ_{ch} = 78 ps and τ_{ce} = 20 ps) we find a huge difference. Obviously 50 pulses are not enough to reach a stable situation. The percentage of uncorrelated captures is clearly overestimated.

6.4.3 Resonant excitation with impurities under pulsed excitation

In the case of resonant excitation with impurities, after checking that the real percentage of uncorrelated captures is really small compared to the excess injected e^- to produce the optical switching, we could neglect the uncorrelated capture. As previously discussed in section 6.1.2, μTRPL experimental data clearly points to the situation of empty QDs before the arrival of every pulse, in that case just one pulse simulation would be enough to describe them. For completeness reasons, we have simulated 50 pulses anyway in order to take into account any residual occupation accumulated between pulses. It always corresponds to dark microstates (without radiative emission), that is, the QD has 1 or 2 electrons or holes on it, but any electron–hole pair.

Table 6.3: TRPL under Non resonant excitation fitting parameters corresponding to figure 6.16

τ_{ee}	10.8 ns
τ_d	0.23 ns
τ_i	0.16 ns
% of impurity absorption for I_0	28
% of impurity absorption for 2 x I_0	38
% of impurity absorption for 4 x I_0	67
% of impurity absorption for 8 x I_0	86

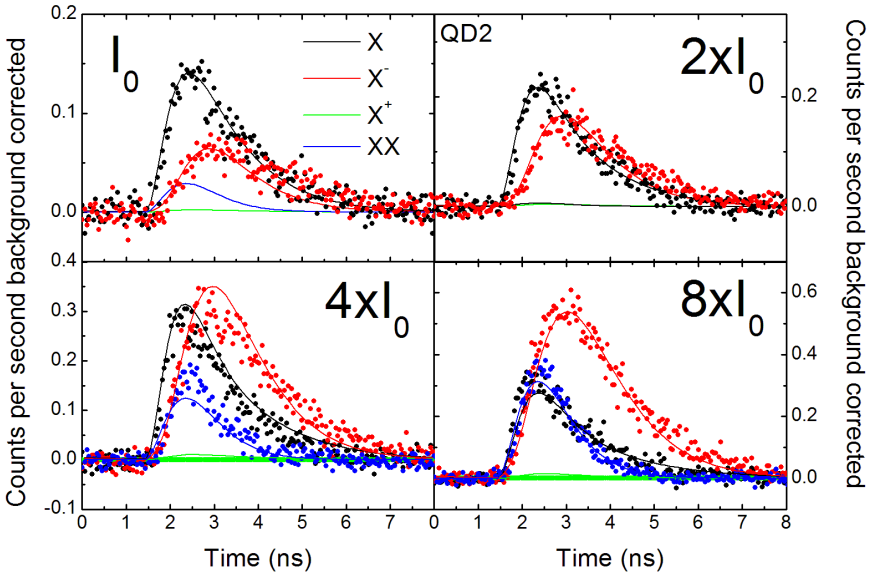

Figure 6.16: **Time resolved photoluminescence evolution under resonant to the impurities excitation. Solid lines correspond to the outcome of the MEM model for the values on table 6.3. Only 50 pulses are simulated.**

The fitting procedure consists in the minimization of the global least squares of all 4 curves in Figure 6.16. The four curves share τ_{ee}, τ_d, τ_i and differ in the pumping constants: the total pumping constant (as measured) and the percentage of the optical pumping that contributes to the impurity related absorption (fitting results for it are also presented in table 6.3). The output of the model quantifies the delay between resonant capture into the QD and the impurity related capture (τ_d in table 6.3) and provides a slower capture through that channel ($\tau_i >> \tau_X$). The time that extra-electrons remain in the QD (τ_{ee}=10.8 ns) is below the repetition period of the diode laser used in the experiment (25 ns), compatible with the empty QD assumption, but well below the infinite (in the time range experimentally studied) escape time assumed for non resonant excitation (see 6.2.6). Somehow one could attribute the e^- escape time to the time

the system needs to recover the original situation after an impurity injects an extra electron to the QD.

6.5 Conclusions.

In conclusion, we have developed a model based on microstates to account quantitatively for the appearance of charge excitons under above barrier excitation as a result of low uncorrelated capture (around 10^{-3} % of the total captures, as estimated from the CW experiments in subsection 6.4.1). The capture times for correlated carriers or excitons extracted with the model are below our experimental setup temporal resolution, while the uncorrelated capture times for e^- and h^+ depend on the local environment of the QD. Optical switching under resonant excitation to impurity levels is observed and studied in time resolved experiments. The μTRPL transients for the exciton emission appear before the negative trion emission, but its intensity exceeds completely that of the exciton after some hundreds of ps. The extra electrons are captured with a finite delay of around 230 ps (fitting result for τ_d in table 6.3) for QD2. The origin of this delay is ascribed to carrier diffusion after photon absorption by an impurity level. The study of the PL intensity under the different excitation conditions (pulsed and continuous wave) evidences uncorrelated electron escape with a finite escape time around 10.8 ns. This escape time is well below the estimated above barrier excitation (above 1 μs). Its origin could be connected through some non radiative transfer towards deep levels (electron traps, possibly), thermal promotion towards WL or both.

Chapter 7

Quantum Dot based Semiconductor Optical Amplifiers

Many quantum dot (QD) based new devices have been proposed and extensively studied in the last decade [7]. Among these devices, quantum dot based lasers and semiconductor optical amplifiers (SOAs) outperform their actual commercial counterparts. In particular, QD SOAs offer high performance characteristics like improved linewidth enhancement factor, low temperature operation sensitiveness and low chirp [6]. But in order to be a technological solution in above 10 Gbit Ethernet networks, high modulation bandwidth is needed while emitting in the optical telecommunications windows[81]. This high bit rate response needs a complete and fast gain recovery in the device, which lays on in basic physical aspects of carrier capture and relaxation in quantum dots, or in the maximal modal gain[82] assuming thermal quasi-equilibrium distribution between barrier, wetting layer and inhomogenously and homogenously broadened distribution of quantum dot levels[29, 83]. To overcome the intrinsic limitations of the overall QD SOAs system, two different strategies can be found in literature: cold carrier tunnel injection [84, 85] and p-modulated doping[86]. P-doping strategy is being widely used to improve temperature operation insensitiveness and its impact in bandwidth modulation has also

been theoretically studied [87]. Doping produces a permanent excess of holes near the QDs that end up in populating QD levels, enhancing carrier capture and relaxation through carrier–carrier scattering[15, 88, 89] or by an increased capture rate in charged dots (positive in that case) due to triggering of the surrounding vibrating polarization field[90]. Impressive results have been lately obtained in un-doped QD based devices,[91, 92] and better performance is expected from new processed p-doped samples.

7.1 Device description

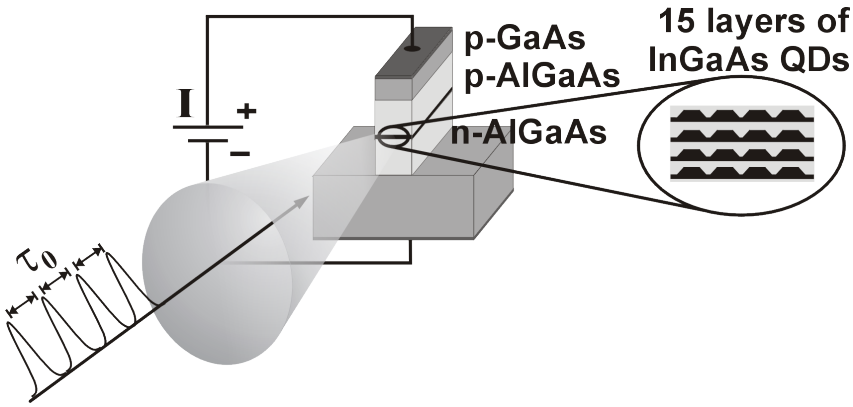

Figure 7.1: **Sketch of the device structure**

Our sample consists of a deeply etched ridge waveguide, 2 μm width, see Fig. 7.1(a). This deep etched structure provides strong index guiding of the optical mode and suppression of current spreading.[93] The active medium is formed by 15 layers (a larger maximum gain favors band width modulation[82]) of MBE grown quantum dots-in-a-well nanostructures with a nominal areal density of 2 10^{10} cm^{-2} and a nominal delta p-doping of 5 10^{17} cm^{-2}. A 33–35 nm GaAs spacer prevents electronic coupling between layers. The sample's length is 1 mm and antireflection coating is applied on both ends of the sample to avoid lasing and allow single pass pulse experiments.

QDs are exciton populated through electrical injection; part of their isotropic spontaneous emission couples to the waveguide structure and

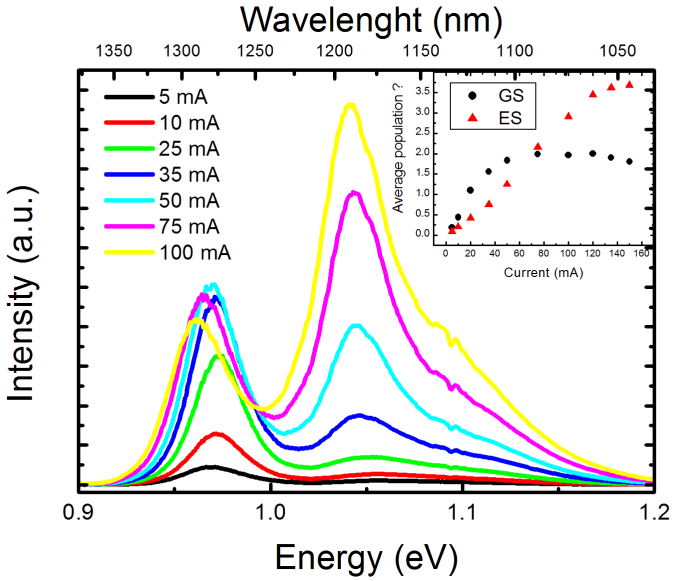

Figure 7.2: **Amplified Spontaneous Emission for different injection currents. The inset shows the characteristic diode I-V curve measured for our device.**

propagates through it, being amplified through stimulated emission of the neighboring QD with energetically resonant energy levels in the process. At the waveguide exit of the device one can measure this Amplified Spontaneous Emission(ASE) as shown in Fig. 7.2. Emission from ground state transition can be identified at 965 meV(1285 nm) and shifts to 954 meV (around 1.3 μm) under high current injection. A well resolved p-shell excited state transition is observed 70 meV in average above ground state. A small size distribution, as the one obtained (33 meV, on average, when fitted to a gaussian), is highly recommendable for high bandwidth modulation [87]. Spontaneous emission for the wetting layer is not seen even at the highest current injection. The clear red-shift of the whole emission observed as current (and voltage) is increased is caused by the Stark shift effect (see subsection 3.3.5) over the whole QD ensemble.

The inset in figure 7.2 shows the integrated ASE evolution of the GS and ES; ASE spectrums are fitted to a two gaussian expression, one for the GS level and one for the ES one, the quantity plotted in the inset

is the area below those gaussians. The scale is arbitrary set to two for the GS saturation and naturally results into 4 for the ES maximum value: it's chosen accordingly to the supposed degeneracy of the GS and ES in self-assembled QDs (see subsection 3.1.2). The experimental findings reproduce the expected population evolution: the ES population begins to grow with a significant GS population and keeps growing after the GS is saturated at 40 mA. The GS population remains saturated for higher currents, as one should expect from the Pauli exclusion principle. With the help of an appropriated modeling, the average population of the ground and excited states will be discussed in section 7.3

7.1.1 Optical amplification.

The main technical characteristic of a SOAs is its optical amplification as a function of injection current. The magnitude of the Gain is defined as the light intensities quotient between the amplified pulse at the output of the device and the original pulse before entering the device.

$$G = \frac{I_{out}}{I_{in}} \tag{7.1}$$

That magnitude is directly related to the population inversion achieved in the used QD level. If that confined level is empty, the pulse will be absorbed and the light out of the device will have less intensity than at its entrance; if the level is full, the pulse will be amplified through stimulated emission.

If we use only one pulse beam in the incoming pump beam (without michelsons interferometers in the setup), equivalent to a big temporal separation between pulses (the inverse of the repetition rate (13 ns)), we can assure a complete gain recovery after every pulse action. That allows to measure light intensity changes directly with a low temporal response detector. Figure 7.3 shows gain (G) as a function of injected current (I_c) measured through two methods: directly using a Ge-detector in a Locked-in scheme and with the Heterodyne setup (probe beam without any pump beam) of section 4.3. G grows fast with I_c, and finds a maximum around I_c = 45 mA. In addition, figure 7.3 presents the overlap between ASE emission and pulse spectra properly scaled. That overlap is also propor-

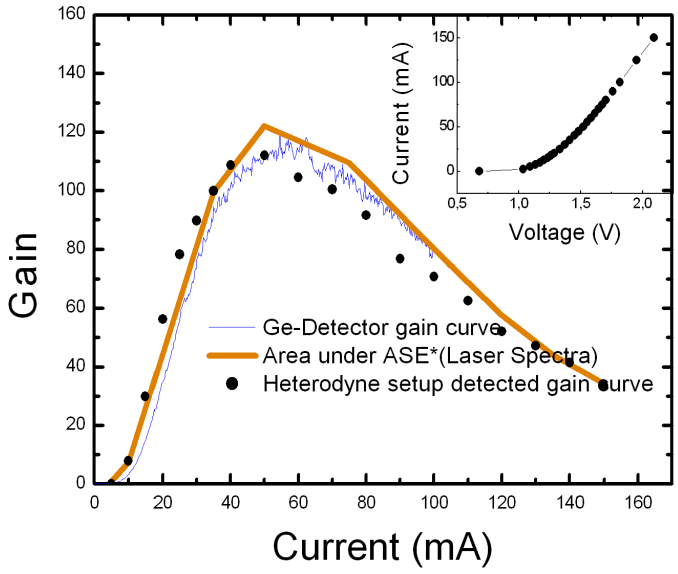

Figure 7.3: **Gain of the GS (1.3 μm) as a function of current measured independently with a Ge-detector and in the Heterodyne setup. Orange line presents the overlap between ASE emission and pulse spectra properly scaled.**

tional to the amount of filled and resonant QDs and is in good agreement with the gain evolution with current. It's important that one notices that at currents higher than 40 mA the Stark-effect induced red-shift reduces the amount of QDs that present GS emission at the same energy than the pulse does. As a consequence, the gain reduces; but the population inversion does not, as the inset of figure 7.2 confirms.

The device response depends also on the intensity of the pump pulse. The Gain remains constant in the linear regime, but saturates for high pulse powers, when the light intensity is sufficient to deplete the population inversion in the GS.

The physical characteristics of the device (like length (L), QD density or number of layers) determine almost fully the absolute gain values. In contrast, the temporal evolution of the gain will be discussed in next sec-

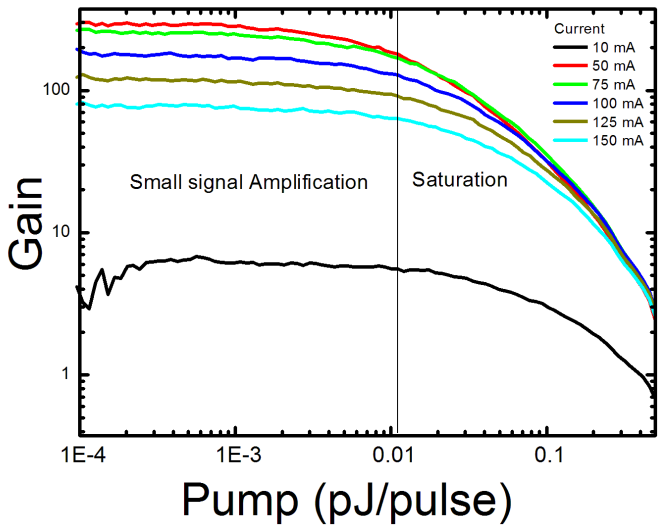

Figure 7.4: **Gain of the GS (1.3 μm) as a function of pump power for different currents.**

tions more in terms of temperature, current or energy splittings of the QDs.

7.2 Heterodyne pump and probe. Gain recovery.

With the setup described in section 4.3 it is possible to measure the temporal gain response of a SOAs to the action of an external pulse propagating through the device. The probe pulse tests the changes induced by the pump pulse. Its power has to be kept in a regime where it only causes small perturbative changes in the device. Even in that case, the influence of the probe pulse in the device dynamics should be taken into account during the results analysis.

7.2.1 Current dependence

Two different regimes can be clearly delimited as a function of current:

- Absorption, where the pump beam is absorbed by the device, generating a temporal excess of population that increases temporally the probe gain afterwards

- Gain, where the pump beam is amplified, causing a decrease in the GS population available and, as a consequence, a temporal decrease of the probe gain.

The current at which the device experiences a transition between both situations is called transparency current (I_{tr}).

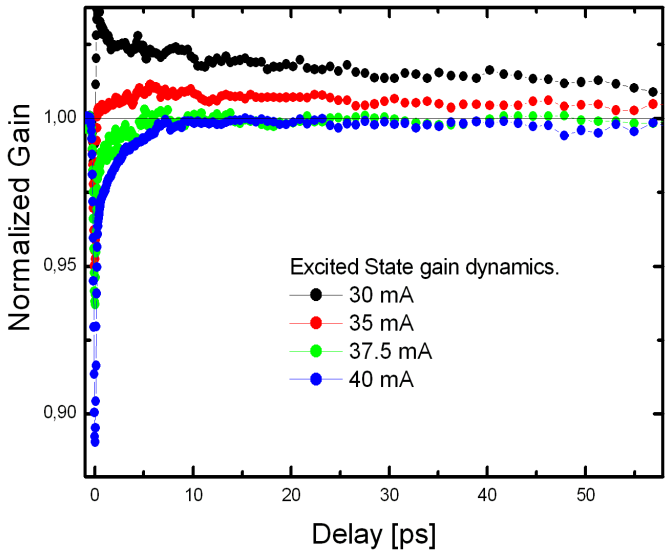

Figure 7.5: **Determination of the transparency current for the ES.**

Figure 7.6 shows gain curves taken around the transparency current for the excited state. It can be clearly observed that at 30 and 35 mA the device is in the absorption regime, while above that currents its in the gain regime. For our device we find a transparency current of $I_{tr} = 7 - -8$ mA for the ground state transition and of $I_{tr} = 35 - -37.5$ mA for excited state.

At I_{tr}, the pulse out of the device is neither absorbed nor amplified. So a pulse exits the device exactly as it was coupled in. The gain, by definition, is set to 1.

The goal of a QD based SOA is to amplify pulses without changing their temporal line shape. near the transparency current the recovery is fast (see, as example, how the 37.5 mA recovers faster than the 40 mA curve in figure 7.6) but the pulse is not amplified at all.

The study of the recovery dynamics and the physical parameters that impact it when current is increased are in the center of the discussion in and after the section 7.2.3.

7.2.2 Pump Intensity dependence

The recovery dynamics depend strongly on the optical power applied at the entrance of the device (Pump intensity), as shown in figure 7.6 and the following.

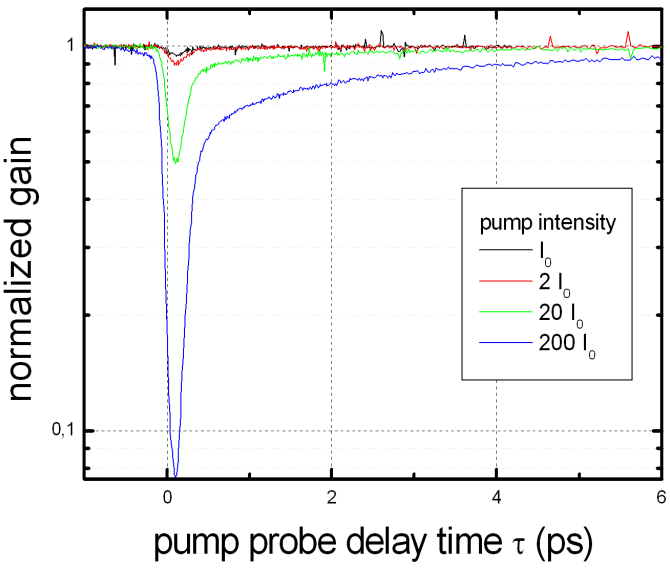

Figure 7.6: **Pump-Probe curves as a function of pump power for a current of 100 mA.**

As one could expect, the depth of the gain depletion after the pulse arrival grows with the Pump intensity. As long as we stay in the linear gain regime, known as small signal amplification [94] (see figure 7.4), the recovery dynamics follow a similar evolution: a fast recovery is observed in the same time regime for different pump powers; the percentage of recovery compared to the initial depletion does not significantly vary.

When we increase the pump power to the saturation regime, the gain recovery takes longer. An accurate analysis will be carried out in the next sections, trying to model numerically the gain recovery in such extreme situations and even under the action of a train of more than one pulse.

7.2.3 Multiple pulses experiments

Ultrafast gain recovery is observed as long as higher energy levels are populated for both, ground and excited states, as in ref. [95]. But some concerns about a speed bottleneck after excited state depletion were formulated in analysis of this kind of experiments[96, 97]: ground state gain dynamics evolution under a pulse train remained still undone. In order to check gain recovery under a pulse train, we introduced a Michelson interferometer at the entrance of our heterodyne set-up[98], with it, we could generate two 150 fs long Fourier-limited pulses, and specify an arbitrary delay between them. ES mediated capture into the GS was exclude as the only relaxation mechanism, introducing direct capture from the 2D reservoir as the key mechanism.

In order to obtain more information about the physical background of the gain dynamics in a QD based SOA, we have pushed our device [98] to the available limits of current and optical pump beam power, while increasing the number of pulses in the excitation train up to four. We are now not longer looking for small signal amplification, moreover, we are interested in completely removing the ground state population inversion, forcing the system until depletion the reservoirs that refill the ground state after amplification. With increasing I_c the electroluminescence (EL) shifts to longer wavelengths as a result of the well known Stark-shift effect(see figure 7.2). Choosing a fixed wavelength, the pump and probe beams excite resonantly different subensembles of QDs at different currents. That

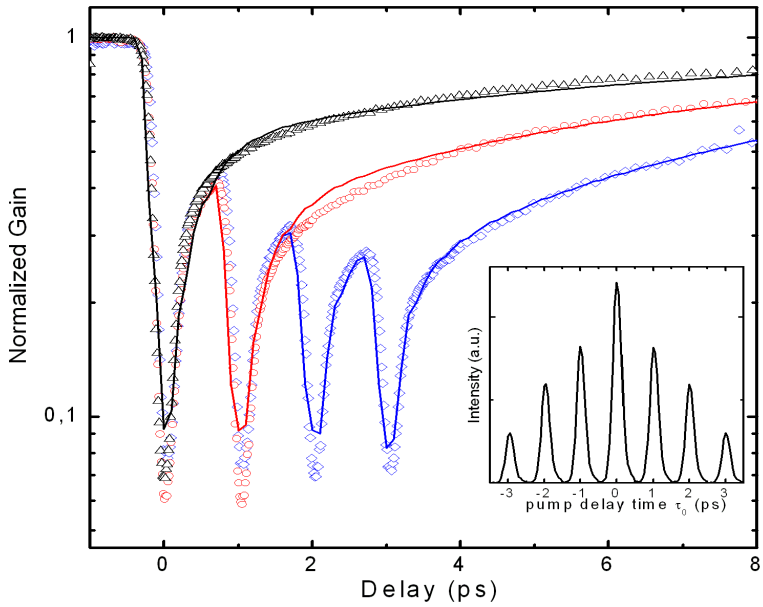

Figure 7.7: **Normalized gain as a function of pump-probe delay at** 35 **mA for** $1, 2$ **and** 4 **pulses in the pump beam. The inset shows the autocorrelation of the pump and reference pulse for** 4 **pulse beams. Solid lines are the outcome of the theoretical model developed in section 7.3**

affects directly the absolute amplification of the device. For different I_c it is not available or in resonance the same amount of QDs at different currents (see figure 7.4 and subsection 7.1.1). To take into account that effect, we normalize the gain, even if the percentage of resonant QDs extracted from the overlap of ASE spectrums and the pulse spectra is taken into account during the modelization and analysis of the experimental data (orange line in figure 7.3). The inset of figure 7.7 shows the crosscorrelation of the pump and reference beams, for a four pulse train with 1 ps delay between the pulses. All pulses have the same power and a FWHM of 150 fs. By blocking mirrors in the interferometers we choose among 1, 2 and 4 pulse experiments.

In the main part of Fig. 7.7, a direct comparison of the dynamics after excitation with different pulses is shown. The system is set to detect the

first pulse of the probe beam after propagation through the device; doing so the rest of the probe train does not interfere with the measurements. The big gain depletions observed at 0, 1, 2 and 3 ps are the direct consequences of the four pulses forming the pump beam. When any of those pulses coincides with the chosen first probe pulse a strong reduction of the gain is observed. The amplification of such strong light pulses and the two photon absorption (TPA) phenomena remove the population inversion in the ground state (GS) after every pulse. There isn't any extreme change after any of the pulses, even if the system is driven to its limits four consecutive times, which is a sign that a depletion of the available reservoirs (the excited state (ES) if the GS refills through internal relaxation or the 2-D reservoir if it is refilled through direct capture) doesn't dramatically change the device dynamics.

7.3 Modeling SOAs dynamics

With the aim of applying recent theoretical developments [87, 83] to the analysis of our measurements, we have adapted some of the available models in the literature [99, 100] to take into account the peculiarities of heterodyne pump-probe experiments on QD based SOAs.

First we will present the peculiarities of our QD system and its interaction with its environment. The new physical concepts will be introduced in the next subsection (7.3.1). Afterwards the integration method is discussed following the experimental pump and probe concept. The propagation effects that the device waveguide introduces are accounted through this integration procedure.

7.3.1 Energetic scheme and thermal distribution

At room temperature, non-equilibrium situations between the QDs and the high energy levels have to be taken into account[29]; at the same time, the experimental evidences of direct capture into the GS of the QD that have been reported for 1.3 μm SOAs [101, 98] make the cascade-capture model uncompleted. Direct capture from the 2D reservoir has to be taken into account too.

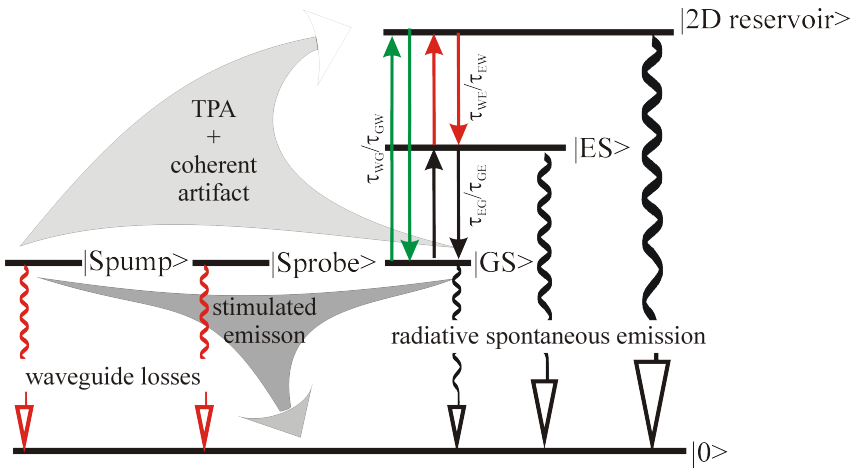

Figure 7.8: **Energetic scheme of the SOAs equation system**

The n doping in the device leads to an excess of holes near the QD and a hole built-in population in the QDs levels [90]; so we assume that the overall dynamics is governed just by the electrons as a first simplified approach.

Figure 7.8 presents the energetic diagram used to describe the SOAs system. The crystal non excited level is represented by $|0\rangle$; at the ground state energy (0.97 eV) we can find the GS population and the *"photon population"* of both light beams, as Pump and Probe beams are resonant in energy to the ground state. Higher in energy we can find the ES population (1.45 eV), while a generic 2D-reservoir level is used to account for the higher energy levels that feed the QD (the edges of WL or the GaAs barriers that are directly connected to the QD).

The processes that result in a carrier change between levels are represented by arrows; each of those arrows corresponds to an specific term in the rate equation system describing the QD based SOA:

$$\begin{aligned}\frac{dn_W}{dt} &= ic + R_{GW} n_1^{rs,nrs} - R_{WG}\left(2N_{QDs} - n_1^{rs,nrs}\right) \\ &\quad + R_{EW} n_2^{rs,nrs} - R_{WE}\left(4N_{QDs} - n_2^{rs,nrs}\right) \\ &\quad - R_{rW} n_W + R_{TPA} n_1^{rs} S^2. \end{aligned} \tag{7.2}$$

$$\begin{aligned}
\frac{dn_2^{rs,nrs}}{dt} &= R_{WE}(4N_{QDs} - n_2^{rs,nrs}) - R_{EW}n_2^{rs,nrs} \\
&\quad -R_{EG}n_2^{rs,nrs}\left(1 - \frac{n_1^{rs,nrs}}{2N_{QDs}}\right) + R_{GE}n_1^{rs,nrs}\left(1 - \frac{n_2^{rs,nrs}}{4N_{QDs}}\right) \\
&\quad -R_r n_2^{rs,nrs}. \qquad (7.3) \\
\frac{dn_1^{rs,nrs}}{dt} &= R_{WG}(2N_{QDs} - n_1^{rs,nrs}) - R_{GW}n_1^{rs,nrs} \\
&\quad -R_{GE}n_1^{rs,nrs}\left(1 - \frac{n_2^{rs,nrs}}{4N_{QDs}}\right) + R_{EG}n_2^{rs,nrs}\left(1 - \frac{n_1^{rs,nrs}}{2N_{QDs}}\right) \\
&\quad -R_r n_2^{rs,nrs} + R_{SG}(n_1^{rs} - N_{QDs})S - R_{TPA}n_1^{rs}S^2. \qquad (7.4) \\
\frac{dS}{dz} &= R_{SG}(n_1^{rs} - N_{QDs})S - R_{TPA}n_1^{rs}S^2 - \alpha S. \qquad (7.5)
\end{aligned}$$

Where $\mathrm{n}_G^{rs,nrs}(t,z)$, $\mathrm{n}_E^{rs,nrs}(t,z)$ and $\mathrm{n}_2D(t,z)$ are, respectively, the electron population of GS, exited state (ES) and the 2D reservoir. N_{QDs} is the total amount of QDs in the considered volume and $\mathrm{S}(t,z)$ (S_{pump}+S_{probe}) refers to the photon flux that goes through the device. R_r, the rate of spontaneous emission, is the inverse of the effective lifetime in the GS and ES (assumed the same) while R_{r2D} is the inverse of the effective residence time in the 2D (the time that an injected carrier stays in that 2D reservoir before being remove by the same current that has injected it). Capture rates from the 2D to the GS (ES), $\mathrm{R}_{2DG(E)}$, depend on the available electron population in the 2D, normally this term is expressed as $\frac{n_{2D}}{\tau_{2DG(E)}\epsilon N_{QDs}}$ (where $\epsilon = 2, 4$ for GS, ES respectively and $\tau_{2DG(E)}$ stands for the 2D to GS(ES) capture time) in the literature, but the term could result in a rate greater than one for $\mathrm{n}_{2D}>>\mathrm{N}_{QDs}$, so we approximate the terms by:

$$R_{2DG} = \frac{1}{\tau_{2DG}}\left(1 - e^{\frac{-n_2D}{2N_{QDs}}}\right) \qquad (7.6)$$

$$R_{2DE} = \frac{1}{\tau_{2DE}}\left(1 - e^{\frac{-n_2D}{4N_{QDs}}}\right) \qquad (7.7)$$

that tend to one when $\mathrm{n}_{2D}>>\mathrm{N}_{QDs}$, but recover the standard form for $\mathrm{n}_{2D}<<\mathrm{N}_{QDs}$.

Thermal escape to higher states is taken into account through $\mathrm{R}_{G(E)2D}$ rates, which result from multiplying the inverse of $\tau_{2DG(E)}$ by the Boltzmann factor $\left(e^{\frac{\Delta E_{2DG(E)}}{k_B T_c}}\right)$ with T_c being the carrier temperature. This

term results in thermal equilibrium if the system evolves sufficiently long. The Two Photon Absorption (TPA) phenomena is proportional to the square of the photon flux and proportional to the resonant level population (n_G^{res}); R_{TPA} is the proportionality constant, while α is the waveguide losses.
Finally, the amplification/absoption rate, R_{SG}, can be expressed as:

$$R_{SG} = \left(1 - e^{gS}\right) \tag{7.8}$$

where g stands for the modal gain; the term recovers the usual form (gS) for $S << N_{QDs}$, and does not give an amplification rate bigger than n_G (when multiplied by the rest of the term) for high photon fluxes, allowing us to reproduce the high photon flux regime.

As stated before, the percentage of QDs resonant to the incoming beams is taken into account. We define two subensembles of QDs, resonant(rs) and non resonant(nrs), which are just connected through the QW level they share, and write different equations for both; in the QW level equation, the sum of both populations is performed. Two different photon fluxes equations are also taken into account (S_{pump}+S_{probe}); that allows us to directly difference both beams as in the real experiments. Further details on the S integration process are explained in the next subsection.

7.3.2 Propagation effects

While operating in the gain regime a pulse grows as it propagates through the device: the pulse strength is not the same along all the device, and as a consequence, different spatial populations should be found after the amplification of the really different local light intensities (at least in the time scale we work (0-8 ps), that doesn't facilitated a spatial redistribution);

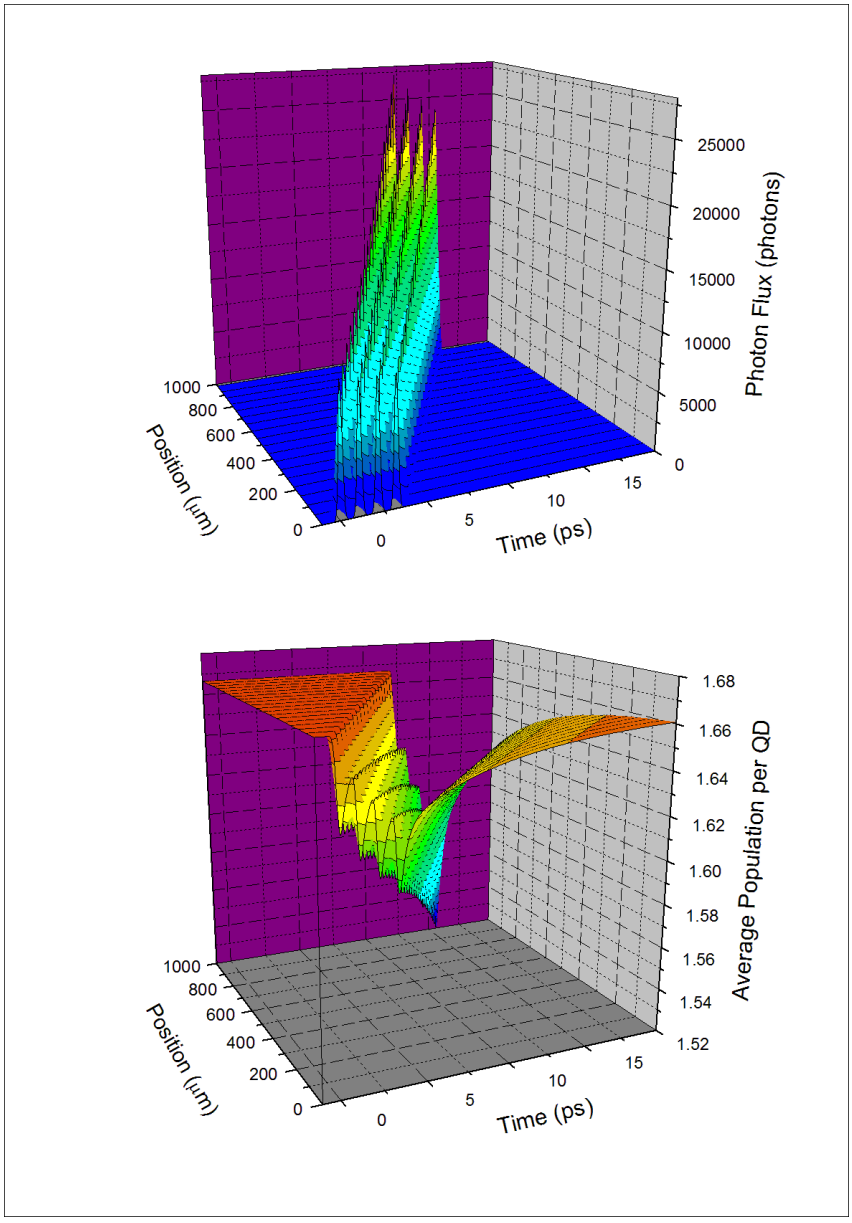

Figure 7.9: **3-D Output of the SOAs model. At the top propagation of a four pulse train, at the bottom, impact of that propagation in the GS population. Both figures are plotted as a function of time and position in the device.**

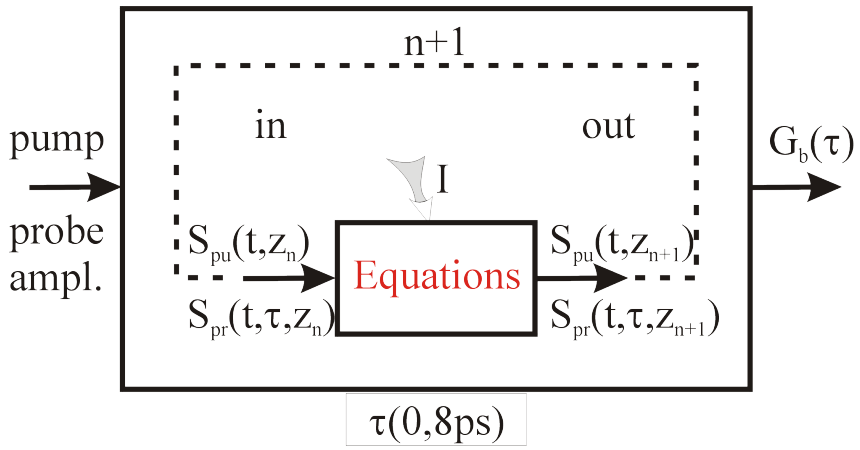

Figure 7.10: **Diagram of the integration procedure of the SOAs model**

In order to reproduce the propagation effects, we divide the device into 200x5 μm-long slices (perpendicular to the propagation direction): given an incoming photon flux we calculate the temporal population evolution and the resulting outcoming pulse for a slice; afterwards we use the propagated outcoming pulse as incoming pulse for the next slice.

A typical outcome of the model is plot in figure 7.9, in that case for small signal amplification. It consists in the set of populations ($n_G^{rs,nrs}(t,z)$, $n_E^{rs,nrs}(t,z)$ and $n_2D(t,z)$) and the photon flux (S(t,z)) as a function of time and position in the device. In the figure only S(t,z) and $n_G^{rs}(t,z)$ are plotted.

Figure 7.10 describes the iterative integrating procedure performed for obtaining the gain curves. To exactly reproduce the experimental situation of an heterodyne pump-probe measurement, the propagation of two different photon fluxes (pump and probe) is calculated for different delays between them.

The quantity $G_b(\tau)$ is the probe photon flux amplification:

$$G_b = S_{probe}(t = \tau_{prop}, z = L, \tau)/S_{probe}(t = 0, z = 0, \tau) \qquad (7.9)$$

Where L is the device length and $\tau_{prop} = nL/c$ is the time it takes to the pulse to cross the whole device (n, index of refraction, is rounded to 3.5 for GaAs). G_b is calculated, point by point, changing the delay between

pulses (τ), obtaining finally the $G_b(\tau)$ curve that is compared with the experimental data.

7.3.3 Model outcome and fitting procedure

The first simulation is done for a four-pulse experiment at low injection current, i.e. as found as standard in literature. For 35 mA injection current we obtain a complete fit (solid color lines in figure 7.7) with the parameter set shown in table 7.1. The fitting procedure consists in a least square routine written in Matlab; the solution of the rate equation differential system is obtained through a standard finite difference method and afterwards combined with the experimental data to calculate the square quantity that is minimized. While most of the extracted parameters look reasonable, the fitted capture times (τ_{2DG} and τ_{2DE}) are below the nominal time resolution of the measurement (the FWHM of the pulses is around 150 fs) and very short. As normally accepted for QD based SOAs, the physical origin behind such a fast capture relies in scattering or Auger-like mechanism inside the quantum dot[100, 102]. Theoretical calculations limit the fastest scattering rates to the range of half a picosecond [103, 104]. The faster times found represent a contradiction with that theoretical calculations and could push new calculations to revise the role of the high density nonequilibrium free carriers in the 2D reservoir and the current crossing the device.

Normally capture times are extracted through multi-exponential fitting (up to four exponentials) and it's dependence with current is interpreted as changes in the underling physical mechanism [105, 102]. Rate equation models are more population oriented, that is, the available carriers in the reservoirs play a role as important as the capture rates. For the further analysis we fix most of the parameters obtained in the 35 mA gain curve fitting and tried to reproduce the rest of the gain curves just varying the effective injected current, the non-equilibrium electron temperature in the device, and the effective residence time in the 2D reservoir. Some of the fits are shown in figure 7.11. Figure 3 shows the experimental data for the InGaAs QDs SOA gain recovery with increasing injection current after 1, 2 and 4 pulses. The subsequent increase of the number of pulses enhances

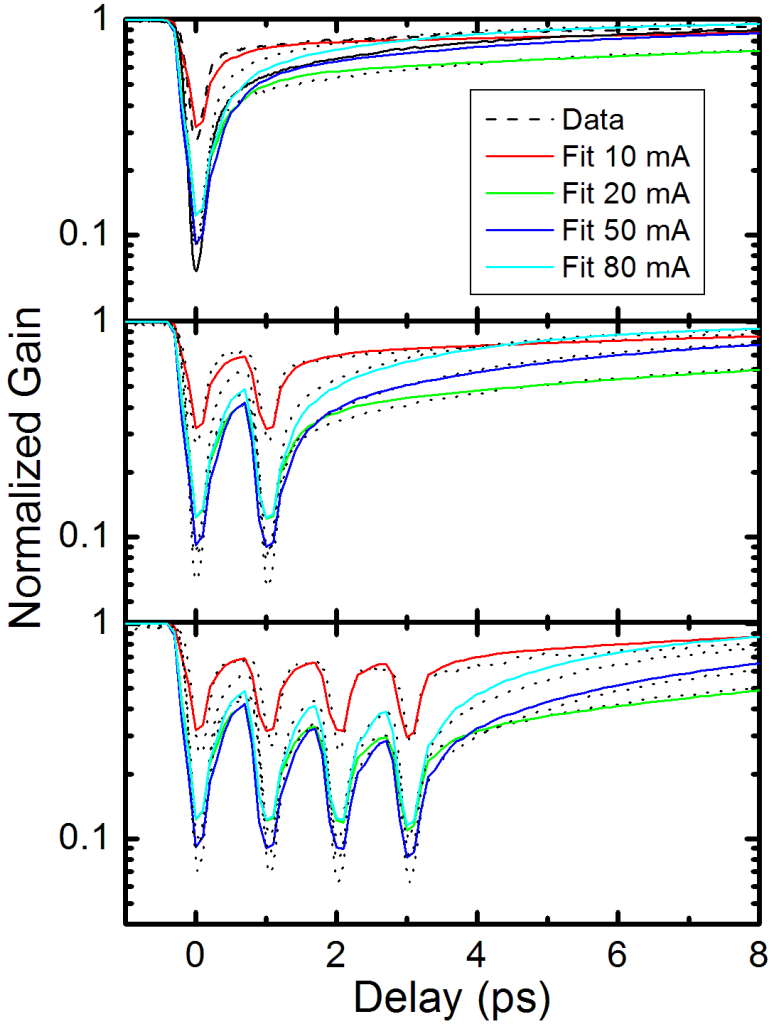

Figure 7.11: **Normalized gain curves for different currents are compared for 1, 2 and 4 pulses. Solid line shows the corresponding fit.**

Table 7.1: Best fit parameters for the 35 mA curve

Parameter	Value (Units)
τ_{2DG},τ_{2DE}	100 fs
τ_{E-G}	500 fs
τ_{rG}, τ_{rE}	445 ps
ΔE_{E-G}	45 meV
ΔE_{2D-G}	210 meV
Γ_{modal}	25 cm^{-1}
α	5 cm^{-1}
f_{TPA}	210^{-5} cm^{-1}
Effective injected current	5 mA
Temperature	403 K
τ_{r2D}	0.7 ps
Pump Intensity	0.1 pJ per pulse
Probe Intensity	0.001 pJ per pulse

the reliability of the simulation, since the full set of 1,2 and 4 pulse-curves will be fitted with only one set of parameters for each injection current.

A slow, normalized gain recovery is observed for the 20 mA curves in all three pulse trains, even when expecting that the reservoirs (ES or 2D) change dramatically their occupation after the amplifications (1 ps is not sufficiently long time to recover the relaxed population to GS, at least in the ES case). The general trend of the data indicates that the dynamics is governed by the overall injected current rather than the average population of the high energy levels. To confirm this qualitative observation, we extract from the fit routines the effective injected current in the whole device, electron temperature and effective lifetime in the 2D reservoir and the thermal equilibrium population for the different quantum levels and plot them in figure 7.12.

The dash line in figure 7.12 serves as eye guideline comparing the real injected current in the device and the calculated effective injected one in the QW-QD system. Just a part of the current crossing the device translates into QD or QW population.

As expected, we can describe the normalized gain evolution just adjust-

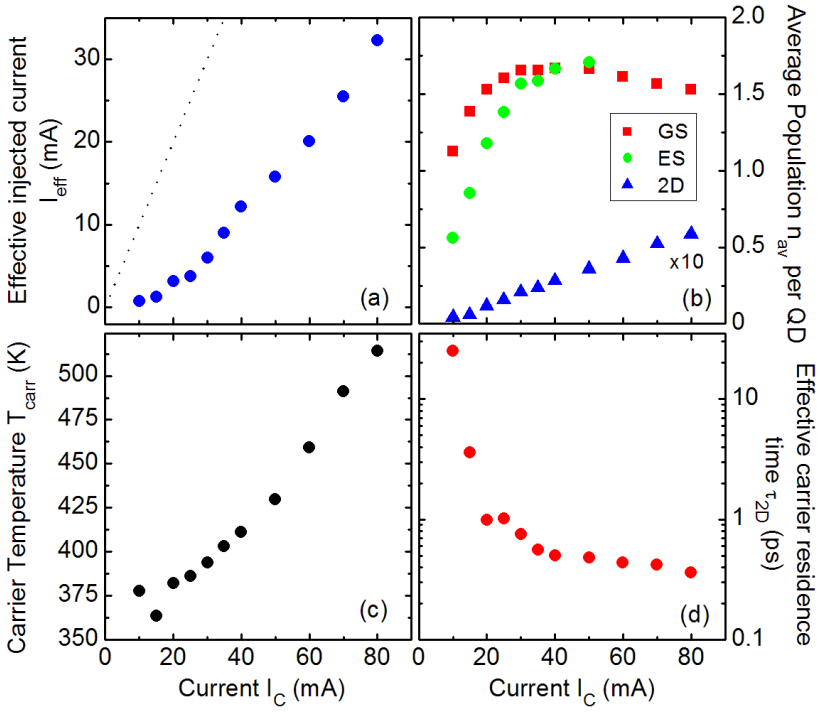

Figure 7.12: **Effective injected current in the whole device(a), electron temperature(b) and effective lifetime in the QW(c) versus the different applied currents to the device, as extracted from the fitting of the different experimental gain curves. (d) Thermal equilibrium population for the different quantum levels**

ing the injected current and the effects it has on the device: (i) the electron temperature grows quickly with current, exceeding the lattice temperature (external measurements estimate a 80 degrees increase for 150 mA), (ii) the effective carrier lifetime in the 2D reservoir, that is strongly connected to the barrier continuum at such high temperatures, decreases, and (iii) the population of the ground state saturates to 1.5 in average population for high injection currents (showing that the high temperatures achieved represent a drawback for better device features).

Figure 7.12 (d) shows the estimate population for the GS, ES and 2D reservoir levels before the arrival of the pulse(s), i.e. the status of the device given by the electrically injected carrier concentration. If one takes the ASE from the device, and integrates the area under the GS and ES, a first approach to the relative GS and ES population can be estimated (figure 7.2). For low currents, this kind of estimation resembles the calculate populations shown in figure 7.12 (d), but for high currents, the ES calculate population decreases slowly while the ASE-estimated one keeps on growing: even with the high complexity achieved in the model, an intrinsic feature of the device is underestimated: spontaneous emission is taken into account through the radiative losses terms (R_r), but not the amplification of it; part of the isotropic emitted spontaneous light couples into the waveguide, and, as it is amplified/absorbed while propagating, depletes or repopulates resonant neighboring QDs. To simulate that effect, recurrent integrations of the whole system should be performed (not just one in the pulse propagation direction), increasing the calculation power demand tremendously. Given the degeneracy of the GS (2) and the ES (4), and that the amplification grows with current, the error associated with that underestimation is bigger for high current ES population estimation and cannot be compensated by a smaller radiative lifetime.

7.4 Conclusions

In conclusion, we have performed heterodyne pump-probe measurements on InGaAs QDs-in-a-well based SOAs. The gain dynamics after 1, 2 and 4 pulses is studied in the saturated gain regime, where the SOA is operated at its optical and electrical amplification limit. A rate equation

model has been adapted to reproduce most of the intrinsic characteristics of QDs as active medium and used to extensively fit our experimental data. The sudden change in the gain dynamics predicted after the 2nd pulse by cascade-capture like models is not observed [96], while considering direct capture to the GS allows us to reproduce the time dynamics in the intermediate ps-range simply as thermal re-equilibrium between capture and escape from the GS. Reproducing the injection current dependence just by changing current dependent parameters (effective injected carriers, electron temperature and escape time from the quantum well) and not the capture and relaxation times itself, allows us to identify the long range dynamics (around 10 ps) of the gain recovery as simply affected by the rate of the carrier injection. The ultimate limit for high-speed applications is therefore assigned to the ability to couple quantum dots to a reservoir of non-equilibrium free carriers.

Chapter 8

General conclusions and outlook

We have combined continuous wave photoluminescence (PL) and time resolved photoluminescence(TRPL) to the study of different shape quantum dots (QD) ensembles. A systematic analysis of the decay times as a function of temperatures is presented within a rate equation model including carrier scape at high temperatures. The increase of the decay time in the range of low temperature is described through exciton thermalization to a dark state.

We have performed confocal microscopy on a single QD, that exhibits optical switching effect under optical selective pumping. The analysis of micro-PL and TRPL combined experimental data in the framework of a microstate master equation model, allows to accurately estimate the time ranges involved in the different physical processes.

Future experiments are proposed to directly measure the time that the extra electron stays on the QD after the impurity mediated capture and evaluate its origin.

Finally, the gain dynamics of a QD based Semiconductor optical amplifier (SOA) under short train pulses is measured. The role of direct capture from the 2D reservoir to the QD ground state is clarified when working in the optical saturation regime. A rate equation model allows us to describe the gain recovery process as a thermal re-equilibrium process. This

description allows to extract the parameters governing the amplification dynamics, and use them in the design or performance analysis of QD based lasers and amplifiers.

Nowadays, the author of this PhD is working at the University of Dortmund, where further experiments on QD based SOAs are carried out to clarify the role of coupled polarization and population dynamics. A better understanding of the physics of population inverted system is under current research, through the four wave mixing technique and variations of the short pulse trains experiments presented here.

Hemos combinado fotolumiscencia en onda continua (PL) y resuelta en tiempo (TRPL) en el estudio de colectivos de puntos cuánticos (QD) con diferentes formas. Se presenta un análisis sistemático del tiempo de decaimiento en función de la temperatura a través de un modelo de ecuaciones de balance que incluye escape térmico de portadores. El incremento del tiempo de vida en el rango de baja temperatura se describe a través de la termalización excitónica a un estado oscuro.

Hemos realizado microscopía confocal en un único punto cuántico, que muestra un cambio brusco en sus transiciones ópticas bajo excitación óptica selectiva. El análisis de la micro-PL y TRPL combinados en base a un modelo de ecuaciones de microestados, permite la estimación precisa del rango de tiempos implicados en los distintos procesos físicos.

Se pueden diseñar nuevos experimentos para medir directamente el tiempo que el electron extra permanece en el QD, después de la captura a través de la impureza.

Finalmente, se ha medido la dinámica de la ganancia en un amplificador óptico de semiconductor (SOA) basado en puntos quánticos tras amplificar trenes de pulsos cortos. El papel de la captura directa desde el reservorio 2D al estado fundamental del QD se clarifica cuando se trabaja en el régimen de saturación óptica. Un modelo de ecuaciones de balance nos permite describir el proceso de la recuperación de ganancia como un proceso de reequilibrio térmico. Esta descripción permite extraer los parametros que gobiernan la dinámica de amplificación, y usarlos para

el diseño o análisis del funcionamiento de láseres y amplificadores basados en puntos quánticos.

En la actualidad, el autor de esta tesis doctoral trabaja en la Universidad de Dortmund, donde se estan llevando a cabo nuevos experimentos en SOAs basados en puntos cuánticos para clarificar el papel del acoplo de la dinámica de la polarización y la población. Se busca una mejor compresión de la física de sistemas con la población invertida, mediante el uso de la técnica de mezcla de cuatro ondas y variaciones de los experimentos con trenes de pulsos cortos presentados aquí.

Bibliography

[1] J. Shah. *Ultrafast Spectroscopy of Semiconductors and Semiconductor Nanostructures.* Springer, 1996.

[2] P.Yu and M.Cardona. *Fundamental of semiconductors: physics and material properties.* Springer-Verlag, 1996.

[3] Ioffe Physico-Technical Institute. Electronic archive: New semiconductor materials. characteristics and properties. http://www.ioffe.ru/SVA/NSM//Semicond/GaAs/bandstr.html.

[4] D. Bimberg, M. Grundmann, and N. N. Ledentsov. *Quantum Dot Heterostructures.* Wiley, 1999.

[5] Y. Arakawa and H. Sakaki. *Appl. Phys. Lett.*, 40:939, 1982.

[6] D. Bimberg. *J. Phys.D.: Appl. Phys.*, 38:2055, 2005.

[7] D. J. Mowbray and M. S. Skolnick. *J. Phys. D: Appl, Phys.*, 38:2059, 2005.

[8] Y. Masumoto and T. Takagahara. *Semiconductor Quantum Dots.* Springer Verlag, 2002.

[9] D. Gammon, E.S. Snow, B.V. Shanabrook, D.S. Katzer, and D. Park. *Science*, 273:87, 1996.

[10] M. Grundmann, J. Christen, N.N. Ledentsov, J. Böhrer, D. Bimberg, S.S. Ruvimov, P. Werner, U. Richter, U. Gösele, J. Heydenreichand, V. M. Ustinov, A. Yu. Egorov, A. E. Zhukov, P. S. Kop'ev, and Zh. I. Alferov. *Phys.Rev.Lett*, 74:4043, 1995.

[11] B. Alén, F. Bickel, K. Karrai, R. Warbuton, and P. Petroff. *Appl.Phys.Lett*, 83:2235, 2003.

[12] M. Bayer and A. Forchel. *Phys.Rev.B*, 65:041308, 2002.

[13] M. Grundmann and D. Bimberg. *Phys. Rev. B*, 55:9740, 1997.

[14] M. Bayer. *Single Quantum Dots. Fundamentals, Applications and New Concepts*, volume 90 of *Topics in Advance Physics*. P. Michler, 2003. Exciton complexes in Self-Assembled In(Ga)As/GaAs Quantum Dots.

[15] J. Urayama, T. B. Norris, H. Jiang, J. Singh, and P. Bhattacharya. *Appl. Phys. Lett.*, 80:2162, 2002.

[16] A. Markus and A. Fiore. *Physica Status Solidi (a)*, 201:338, 2004.

[17] K. Karrai, R.J. Warburton, C. Schulhauser, A. Hogele, B. Urbaszek, E.J. McGhee, A.O. Govorov, J.M. García, B.D. Gerardot, and P.M. Petroff. *Nature*, 427:6970, 2004.

[18] K.P. O'Donnell and X. Chen. *Appl. Phys. Lett.*, 58:2924, 1990.

[19] G. Ortner, M. Schwab, M. Bayer, R. Pässler, S. Fafarda, Z. Wasilewski, P. Hawrylak, and A. Forchel. *Phys.Rev.B*, 72:085328, 2005.

[20] R. Heitz, M.Veit, N.N. Lendentsov, A. Hoffman, D. Bimberg, V.M. Ustinov, P.S.Kop'ev, and Zh. Alferov. *Phys. Rev. B*, 56:10435, 1997.

[21] U. Bockelmann and G. Bastard. *Phys. Rev. B*, 42:8947, 1990.

[22] H. Benisty, C. M. Sottomayor-Torres, and C. Weisbuch. *Phys. Rev. B*, 44:10945, 1991.

[23] T. Inoshita and H. Sakaki. *Phys. Rev. B*, 46:7260, 1992.

[24] O. Verzelen, R. Ferreira, and G. Bastard. *Phys. Rev. Lett.*, 88:146803, 2002.

[25] R. Ferreira and G. Bastard. *Appl.Phys.Lett*, 74:2818, 1999.

[26] E.W. Boggard, J.E.M. Haverkort, T. Mano, T. van Lippen, R. Nötzel, and J.H. Wolter". *Phys. Rev. B*, 72:195301, 2005.

[27] T.B. Norris, K. Kim, J. Urayama, Z.K. Wu, J. Singh, and P K Bhattacharya. *J. Phys D: Appl. Phys.*, 38:2077, 2005.

[28] J. Urayama, T. B. Norris, J. Singh, and P. Bhattacharya. *Phys. Rev. Lett.*, 86:4930, 2001.

[29] H.D.Summers D.R. Matthews and P.M.Smowton. *Appl.Phys.Lett.*, 81:4904, 2002.

[30] M.A. Lampert and P. Mark. *Current injection in Solids.* Academia Press, 1970.

[31] H. Jiang and J. Singh. *J. Appl. Phys.*, 85:7438, 1999.

[32] P. W. Fry, I. E. Itskevich, D. J. Mowbray, M. S. Skolnick, J. J. Finley, J. A. Barker, E. P. O'Reilly, L. R. Wilson, I. A. Larkin, P. A. Maksym, M. Hopkinson, M. Al-Khafaji, J. P. R. David, A. G. Cullis, G. Hill, and J. C. Clark. *Phys. Rev. Lett.*, 84:733, 2000.

[33] R.J. Warburton, C. Schulhauser, D. Haft, C. Schäflein, K. Karrai, J. M. Garcia, W. Schoenfeld, and P. M. Petroff. *Phys.Rev.B*, 65: 113303, 2002.

[34] B. Alén, J. Bosch, D. Granados, J. Martínez-Pastor, J.M. García, and L. González. *Phys.Rev. B*, 75:045319, 2007.

[35] W.Demtröder. *Laser Spectroscopy.* Springer Verlag, 1996.

[36] K. L. Hall, G. Lenz, E. P. Ippen, and G. Raybon. *Opt. Lett.*, 17:874, 1992.

[37] K. L. Hall, G. Lenz, A. M. Darwish, and E. P. Ippen. *Opt. Commun.*, 11:589, 1994.

[38] A. Mecozzi and J. Mørk. *J.Opt.Soc.Am.B*, 13:2437, 1996.

[39] K. Ouchi and T. Mishina. *J. Cryst. Growth*, 209:242, 2000.

[40] J. M. Ripalda, D. Granados, Y. González, A. M. Sánchez, S. I. Molina, and J. M. García. *Appl. Phys. Lett.*, 87:202108, 2005.

[41] J. M. García, G. Medeiros-Ribeiro, K. Schmidt, T. Ngo, and P. M. Petroff. *Appl. Phys. Lett.*, 71:2014, 1997.

[42] D. Granados and J. M. García. *Appl. Phys. Lett.*, 82:2401, 2003.

[43] R. Warburton, C. Schaflein, D. Haft, F. Bickel, A. Lorke, K. Karrai, J.M. García, W. Schoenfeld, and P.M. Petroff. *Nature*, 405:926, 2000.

[44] P. Offermans, P. M. Koenraad, J. H. Wolter, D. Granados, J. M. García, V. M. Fomin, V. N. Gladilin, and J. T. Devreese. *Appl. Phys. Lett.*, 87:131902, 2005.

[45] D. Granados, J. M. García, T. Ben, and S. I. Molina. *Appl. Phys. Lett.*, 86:071918, 2005.

[46] F. Guffarth, R. Heitz, A. Schliwa, K. Potschke, and D. Bimberg. *Physica E*, 21:326, 2004.

[47] H. Pettersson, R. Warburton, A. Lorke, K. Karrai, J.P. Kotthaus, J.M. García, and P.M. Petroff. *Physica E*, 6:510, 2000.

[48] A. Lorke, R. Luyken, A. Govorov, J.P. Kotthaus, J.M. García, and P.M. Petroff. *Phys. Rev. Lett.*, 84:2223, 2000.

[49] B. Alén, J. Martínez-Pastor, D. Granados, and J.M. García. *Phys. Rev. B*, 72:155331, 2005.

[50] D. Haft, C. Schulhauser, A. Govorov, R. Warburton, K. Karrai, J.M. García, W. Schoenfeld, and P.M. Petroff. *Physica E*, 13:165, 2002.

[51] R. Heitz, A. Kalburge, Q. Xie, M. Grundmann, P. Chen, A. Hoffmann, A. Madhukar, and D. Bimberg. *Phys. Rev. B*, 57:9050, 1998.

[52] C. Santori, G. Solomon, M. Pelton, and Y. Yamamoto. *Phys. Rev. B*, 65:073310, 2002.

[53] R. Heitz, H. Born, F. Guffarth, O. Stier, A. Schliwa, A. Hoffmann, and D. Bimberg. *Phys. Status Solidi (a)*, 190:499, 2002.

[54] J. Bellessa, V. Voliotis, R. Grousson, X.L. Wang, M. Ogura, and H. Matsuhata. *Phys. Rev. B*, 58:9933, 1998.

[55] H. Yu, S. Lycett, C. Roberts, and R. Murray. *Appl. Phys. Lett.*, 69: 4087, 1996.

[56] W. Yang, R.R. Lowe-Webb, H. Lee, and P.C. Sercel. *Phys. Rev. B*, 56:13314, 1997.

[57] A. Fiore, P. Borri, W. Langbein, J.M. Hvam, U. Oesterle, R. Houdré, R.P. Stanley, and M. Ilegems. *Appl. Phys. Lett.*, 76:3430, 2000.

[58] M. Gurioli, A. Vinattieri, M. Zamfirescu, M. Colocci, S. Sanguinetti, and R. Nötzel. *Phys. Rev. B*, 73:085302, 2006.

[59] G. Bacher, C. Hartmann, H. Schweizer, T. Held, G. Mahler, and H. Nickel. *Phys. Rev. B*, 47:9545, 1993.

[60] E.C. Le Ru, J. Fack, and R. Murray. *Phys. Rev. B*, 67:245318, 2003.

[61] S. Sanguinetti, M. Henini, M. Grassi Alessi, M. Capizzi, P. Frigeri, and S. Franchi. *Phys. Rev. B*, 60:8276, 1999.

[62] P. Dawson, O. Rubel, S.D. Baranovskii, K. Pierz, P. Thomas, and E. O. Göbel. *Phys. Rev. B*, 72:235301, 2005.

[63] S. Sanguinetti, D. Colombo, M. Guzzi, E. Grilli, M. Gurioli, L. Seravalli, P. Frigeri, and S. Franchi. *Phys. Rev. B*, 74:205302, 2006.

[64] F. Briones and A. Ruiz. *J. Cryst. Growth*, 111:194, 1991.

[65] G. Munoz-Matutano, B. Alén, J. Martínez-Pastor, L. Seravalli, P. Frigeri, and S. Franchi. *Superlattices and Microstuctures*, in press: doi:10.1016/j.spmi.2007.07.028, 2007.

[66] G.Munoz-Matutano. Espectroscopía excitónica y multiexcitónica de puntos cuánticos aislados de inas. Master's thesis, Universitat de València, 2007.

[67] G. Munoz-Matutano, J.Gomis, B. Alén, J. Martínez-Pastor, L. Seravalli, P. Frigeri, and S. Franchi. *Physica E*, in press: doi:10.1016/j.physe.2007.09.182, 2007.

[68] R. M. Thompson, R. M. Stevenson, A. J. Shields, I. Farrer, C. J. Lobo, D. A. Ritchie, M. L. Leadbeater, and M. Pepper. *Phys. Rev. B*, 64:201302, 2001.

[69] R. J. Warburton, B. T. Miller, C. S. Dürr, C. Bödefeld, K. Karrai, J. P. Kotthaus, G. Medeiros-Ribeiro, P. M. Petroff, and S. Huant. *Phys. Rev. B*, 58:16221, 1998.

[70] R. M. Stevenson, R. M. Thompson, A. J. Shields, I. Farrer, B. E. Kardynal, D. A. Ritchie, and M. Pepper. *Phys. Rev. B*, 66:081302, 2002.

[71] E. S. Moskalenko, K. F. Karlsson, P. O. Holtz, B. Monemar, W. V. Schoenfeld, J. M. García, and P. M. Petroff. *Phys. Rev. B*, 64:085302, 2001.

[72] J. Martínez-Pastor, A. Vinattieri, L. Carraresi, M. Colocci, Ph. Roussignol, and G. Weimann. *Phys.Rev. B*, 47:10456, 1993.

[73] M. Atatüre, J. Dreiser, A. Badolato, A. Högele, K. Karrai, and A. Imamoglu. *Science*, 312:551, 2006.

[74] A. Greilich, D. R. Yakovlev, A. Shabaev, Al. L. Efros, I. A. Yugova, R. Oulton, V. Stavarache, D. Reuter, A. Wieck, and M. Bayer. *Science*, 313:341, 2006.

[75] A. Greilich, A. Shabaev, D. R. Yakovlev, Al. L. Efros, I. A. Yugova, D. Reuter, A. Wieck, and M. Bayer. *Science*, 317:1896, 2007.

[76] A. Hartmann, Y. Ducommun, E. Kapon, U. Hohenester, and E. Molinari. *Phys. Rev. Lett.*, 84:5648–5651, 2000.

[77] E. S. Moskalenko, K. F. Karlsson, P. O. Holtz, B. Monemar, W. V. Schoenfeld, J. M. García, and P. M. Petroff. *Phys. Rev. B*, 66:195332, 2002.

[78] W.-H. Chang, H.-S. Chang, W.-Y. Chen, T. M. Hsu, T.-P. Hsieh, J.-I. Chyi, and N.-T. Yeh. *Phy. Rev. B*, 72:233302, 2005.

[79] E. S. Moskalenko, V.Donchev, K. F. Karlsson, P. O. Holtz, B. Monemar, W. V. Schoenfeld, J. M. García, and P. M. Petroff. *Phys. Rev. B*, 68:155317, 2003.

[80] G. Bacher, R. Weigand, J. Seufert, V. D. Kulakovskii, N. A. Gippius, A. Forchel, K. Leonardi, and D. Hommel. *Phys. Rev. Lett.*, 83:4417–4420, 1999.

[81] M. Sugawara, N. Hatori, M. Ishida, H. Ebe, Y. Arakawa, T. Akiyama, K. Otsubo, T. Yamamoto, and Y. Nakata. *J. Phys. D*, 38:2126, 2005.

[82] M. Ishida, N. Hatori, T. Akiyama, K. Otsubo, Y. Nakata, H. Ebe, M. Sugawara, and Y. Arakawa. *Appl. Phys. Lett.*, 85:4145, 2005.

[83] W. W. Chow and S. W. Koch. *IEEE J. Quant. El.*, 41:495, 2005.

[84] P. Bhattacharya, S. Ghosh, S. Pradhan, J. Singh, Z. W. Wu, J. Urayama, K. Kim, , and T. B. Norris. *IEEE J. Quant. El.*, 39: 952, 2003.

[85] Z. Mi, P. Bhattacharya, and S. Fathpour. *Appl. Phys. Lett.*, 86: 153109, 2005.

[86] K. Otsubo, N. Hatori, M. Ishida, S. Okumura, T. Akiyama, Y. Nakata, H. Ebe, M. Sugawara, and Y. Arakawa. *Jpn. J. Appl. Phys.*, 43:L1124, 2004.

[87] D.G. Deppe and H.Huang. *IEEE J. Quant. El.*, 42:324, 2006.

[88] K. Gündogdu, K. C. Hall, T. F. Boggess, D. G. Deppe, and O. B. Shchekin. *Appl. Phys. Lett.*, 84:2793, 2004.

[89] K. Gündogdu, K. C. Hall, T. F. Boggess, D. G. Deppe, and O. B. Shchekin. *Appl. Phys. Lett.*, 85:4570, 2004.

[90] K. W. Sun, A. Kechiantz, B. C. Lee, and C. P. Lee. *Appl. Phys. Lett.*, 88:163117, 2006.

[91] M. Lämmlin, G. Fiol, C. Meuer, M. Kuntz, F. Hopfer, A. R. Kovsh, N. N. Ledentsov, and D. Bimberg. *Electronics Lett.*, 42:697, 2006.

[92] D. Bimberg, M. Lämmlin, G. Fiol, C. Meuer, M. Kuntz, F. Hopfer, N. N. Ledentsov, and A. R. Kovsh. *ICTONmanuscript.*, 0:0, 2006.

[93] M. Kuntz, G. Fiol, M. Laemmlin, D. Bimberg, M. G. Thompson, K. T. Tan, C. Marinelli, R. V. Penty, I. H. White, V. M. Ustinov, A. E. Zhukov, Yu. M. Shernyakov, and A. R. Kovsh. *Appl. Phys. Lett.*, 85:843, 2004.

[94] S.Schneider. Carrier dynamics in electrically pumped semiconductor quantum dot amplifiers. Master's thesis, Universität Dortmund, 2004.

[95] S. Schneider, P. Borri, W. Langbein, U.Woggon, R. L. Sellin, D. Ouyang, and D. Bimberg. *IEEE Photon. Technol. Lett.*, 17:2014, 2005.

[96] T. W. Berg, S. Bischoff, I. Magnusdottir, and J. Mørk. *IEEE Phot. Techn. Lett.*, 13:541, 2001.

[97] K. Kim, J. Urayama, T. B. Norris, J. Singh, J. Phillips, and P. Bhattacharya. *Appl. Phys. Lett.*, 81:670, 2002.

[98] S. Dommers, V. V. Temnov, U. Woggon, J. Gomis, J. Martinez-Pastor, M. Laemmlin, and D. Bimberg. *Appl. Phys. Lett.*, 90:033508, 2007.

[99] A. Fiore and A. Markus. *IEEE J. Quant. El.*, 43:287, 2007.

[100] T. R. Nielsen, P. Gartner, and F. Jahnke. *Phys. Rev. B*, 69:235314, 2004.

[101] G. Rainò, G. Visimberga, A. Salhi, M. De Vittorio, A. Passaseo, R. Cingolani, and M. De Giorgi. *Appl. Phys. Lett.*, 90:111907, 2007.

[102] V. Cesari, W. Langbein, P. Borri, M. Rossetti, A.Fiore, S. Mikhrin I. Krestnikov, and A. Kovsh. *Appl. Phys. Lett.*, 90:201103, 2007.

[103] E. Malic, K. J. Ahn, M. J. P. Bormann, P. Hovel, E. Scholl, A. Knorr, M. Kuntz, and D. Bimberg. *Appl. Phys. Lett.*, 89:101107, 2006.

[104] E. Malic, M. J. P. Bormann, P. Hovel, M. Kuntz, D. Bimberg, A. Knorr, and E. Scholl. *IEEE Journal of Selected Topics in Quantum Electronics*, 13:1242, 2007.

[105] T. Piwonski, I. O'Driscoll, J. Houlihan, G. Huyet, R. J. Manning, and A. V. Uskov. *Appl. Phys. Lett.*, 90:122108, 2007.

Acknowledgements

First of all, I would like to thank my thesis directors, Juan Martínez-Pastor and Ulrike Woggon. They have been really supportive and patient in the long learning process that I complete finally with this text.

Science is the result of team-work. During these five years I have been really lucky to share laboratory and tasks with different colleagues. I extremely appreciate the time next to Walid Ouerghui, studying quantum ring multi-layer samples, Sabine Dommers and Vasily Temnov that shared with me the pump-probe heterodyne study of QD based SOAs and Guillermo Muñoz-Matutano, Benito Alén and Josep Canet-Ferrer drivers in our confocal trip.

I would love to thank also the actual and former members of the research groups that have taken me in, the *"Unidad de Materiales y Dispositivos Optoelectrónicos UMDO"* (David Fuster, José Bosch, José Luis Valdes, Laura Martin-Carron, José Marqués, Kamal Abderrafi, Raül García, Rafael Abargues, Esteban Pedrueza and Ernesto Jiménez) and the *EIIb* (Oliver Shöps, Björn Möller, Marco Allione, Yurij Fedutik and Vitali Anike-

yev and former group members Paola Borri, Stephan Schneider and Wolfgang Langbein), and the members of the institutions where I have worked, specially my officemates and friends, Abel Puche, Pablo Pardo and Jaume Vila and the research group members of the Group of Spectroscopy of Solids (GES) in Valencia and the EIIa group in Dortmund. It has been really nice to work at your side.

And special mention should be addressed to the growers of the samples studied: Daniel Granados and Jorge García, who provide their early grows of different shapes samples, Lucca Seravalli, Paola Frigeri and Secondo Franchi, the growers of the LGR sample studied in chapter 6 and Mathias Laemmlien and Dieter Bimberg, responsible of the QD based SOA device.

I have to acknowledge the support of the Spanish Ministry of Science through their program of research fellowships (FPI) and the European network SANDIE, who supported part of my stay in Dortmud and the last months in Valéncia.

Per últim l'agraïment més cabdal: Res d'això hauria estat possible sense la meva família, gràcies per l'esforç ... vosaltres heu fet el camí amb mi.